NTNU
Norwegian University of
Science and Technology

Numerical Simulation of Installation of XL Monopile for Offshore Wind Turbines

Fride Midtbø Birkeland

Marine Technology
Submission date: August 2016
Supervisor: Bernt Johan Leira, IMT
Co-supervisor: Zhen Gao, IMT

Norwegian University of Science and Technology
Department of Marine Technology

NTNU – Trondheim
Norwegian University of
Science and Technology

Numerical Simulation for Installation of XL Monopile for Offshore Wind Turbine

Fride Midtbø Birkeland

August 2016

MASTER THESIS
Department of Marine Technology
Norwegian University of Science and Technology

Supervisor 1: Professor Zhen Gao

Supervisor 2: Professor Bernt J. Leira

NTNU Trondheim
Norwegian University of Science and Technology
Department of Marine Technology – Group of Marine Structures

MSC THESIS IN MARINE TECHNOLOGY

SPRING 2016

FOR

STUD.TECHN. Fride Birkeland

Numerical Simulation of Installation of XL Monopile for Offshore Wind Turbines

Background:
Offshore wind industry is developing very fast. Transportation and installation are important aspects for reducing the life-cycle cost of offshore wind farms. Most of the offshore wind farms today are located in shallow waters (10-30 m of water depth), and monopile has been the dominate foundation with a more than 90% market share. A recent development on XL monopiles has shown a potential for water depth up to 40 m (http://www.esru.strath.ac.uk/EandE/Web_sites/14-15/XL_Monopiles/index.html).

An XL monopile may have a diameter of 7.5 m, a length of 60 m and a weight of around 900 ton. Installation of monopile foundations today are based on crane operations using jack-ups, followed by a hammering process. There is also a trend to use floating installation vessels which are less weather-sensitive during the positioning phase. However, it is challenging to install XL monopiles due to its large size and heavy weight. In particular, the floating installation vessel will move in waves and the resonant pendulum motion of the lifted foundation has been found critical for the safety assessment of such operation. Vessel motions introduce large forces in the gripper (which is rigidly connected to the vessel and functions as a guide for the monopile during the lowering and hammering processes) and in the lift wire.

A correct model of damping is important for resonant motion analysis. Since the monopile has a large diameter, both the diffraction and the radiation problems become important for short waves and moderate seas (which are typical wave conditions during installation). In particular, it was found that the wave radiation damping due to the motions of the monopile needs to be considered for lowering analysis, since the viscous damping on monopile for such wave conditions is small. On the other hand, during the lowering process, the submergence of the monopile and therefore the hydrodynamic properties change continuously. This requires a nonstationary load and response analysis, normally carried out in time domain. Such effect is captured by interpolating the excitation forces and the retardation functions with respect to the submergence, under the assumption that the lowering is a long process as compared to the typical periods of the monopile motions.

This thesis is a continuation of the project work of the student from last semester. The purpose of the thesis work is to develop a coupled numerical model of the monopile and the installation vessel in SIMO based on the hydrodynamic results obtained in the project work, and to study the dynamic responses of the monopile during the lowering process.

The student will be provided the design and the numerical model of the floating installation vessel in SIMO.

Assignment:
The following tasks should be addressed in the thesis work:

1. Literature review on hydrodynamic load analysis for the monopile lowering process, in particular with a focus on the nonlinear wave loads with a varying submergence of the monopile. Literature

review on coupled motion analysis of a multi-body system (a two-body (monopile and installation vessel) system in this case). Issues about the mechanical and hydrodynamic coupling between the two bodies should be studied. Aspects of time-variant system properties (such as the added mass and potential damping as a function of the submergence and the lift wire stiffness as a function of the wire length) should be looked at.

2. Based on the vessel model from Dr. Lin Li, develop the time-invariant coupled monopile and vessel model in SIMO with a proper mechanical coupling (lift wire). Perform an eigenvalue analysis to obtain the natural frequencies of different modes as a function of the submergence. Understand the possible governing motion modes and response parameters of such lowering operation.

3. Define a set of submergence of the monopile, perform regular wave analysis of the time-invariant model in the time-domain code SIMO for each submergence to obtain RAOs of typical response parameters (monopile motions, vessel motions and lift wire tension). Compare the RAOs of the same response parameters for different submergence. Discuss the feature of the obtained RAOs.

4. For selected irregular wave conditions, perform time-domain simulations and obtain the response spectra. Compare them with those obtained by a frequency-domain method using the obtained response RAOs and the input wave spectrum. Compare the response statistics (standard deviation and short-term extreme value).

5. Develop a time-variant numerical model based on the Morison's formula for monopile hydrodynamic loads. For the same irregular wave conditions considered in Task 4, perform time-domain simulations and compare the response statistics with those obtained by the time-invariant model.

6. Report and conclude on the investigation.

In the thesis the candidate shall present his/her personal contribution to the resolution of problem within the scope of the thesis work.

Theories and conclusions should be based on mathematical derivations and/or logic reasoning identifying the various steps in the deduction.

The candidate should utilize the existing possibilities for obtaining relevant literature.

The thesis should be organized in a rational manner to give a clear exposition of results, assessments, and conclusions. The text should be brief and to the point, with a clear language. Telegraphic language should be avoided.

The thesis shall contain the following elements: A text defining the scope, preface, list of contents, summary, main body of thesis, conclusions with recommendations for future work, list of symbols and acronyms, reference and (optional) appendices. All figures, tables and equations shall be numerated.

The supervisor may require that the candidate, in an early stage of the work, present a written plan for the completion of the work. The plan should include a budget for the use of computer and laboratory resources that will be charged to the department. Overruns shall be reported to the supervisor.

The original contribution of the candidate and material taken from other sources shall be clearly defined. Work from other sources shall be properly referenced using an acknowledged referencing system.

The thesis shall be submitted electronically in DAIM:

- Signed by the candidate
- The text defining the scope included
- Codes and/or drawings which cannot be inserted in the thesis file should be organized in a separate zip file.

Bernt J. Leira
Zhen Gao
Supervisors

Deadline: 12.8.2016

Preface

This master's thesis work has been carried out during the spring and summer of 2016, at the Norwegian University of Science and Technology in Trondheim. The thesis is submitted in support of a candidature for a Master's of Science Degree in Marine Technology. The topic of this thesis was proposed by the Offshore Wind Energy Group at the Department of Marine Technology and modified to concern XL monopiles in collaboration with AXTech AS in Molde.

Before starting this master's thesis work I had no experience with the MARINTEK software SIMO, mainly used to conduct the analyses in this report. Performing the analyses thus turned out more challenging than first expected, especially since a lot of the work has been carried out during the department's holiday period. Even if I have had a steep learning curve and it has been rewarding to familiarize with the software, the work is due to this not as comprehensive as first planned.

I would like to express my deepest gratitude to my supervisors at the Department of Marine Technology, Professor Zhen Gao and Professor Bernt Johan Leira, for their guidance and patience. My appreciation also goes to Dr. Lin Li that provided me with necessary input and guidance to conduct the first analyses and to the PhD candidate Yuna Zhao who spent some time this summer answering questions regarding my SIMO model.

I would also like to thank all the great employees at AXTech AS that I have had the pleasure to work with for the last four summers, for interesting discussions and for always being welcoming. My appreciation especially goes to Richard Myhre, Kjell Ødegård, Andreas Ludvigsen and Anne Mathilde Wicken for all their support, for letting me have all this valuable work experience and for letting me borrow office space to finish my thesis.

Finally, I want to thank my fellow students at office C1.076 for all the valuable discussions, the sharing of knowledge and the support during the work with this Master's thesis and for all the great moments over the last five years.

Trondheim, 12.08.16

Fride Midtbø Birkeland

Executive Summary

There has to be a significant increase in the share of power supplied by renewable energies to reduce global emission, simultaneously as the wealth is rising in the newly industrialized countries. Wind energy is one of the sustainable resources predicted to provide an increasing share of this power, due to the large extent of untapped resources offshore.

Kiełkiewicz et al. (2015) argue that, with regards to cost per megawatt of rated power, it is more favourable to use higher capacity wind turbines supported on larger piles than to use the turbines commonly used today. Even though the capital costs depend more on the number of structures than the size of the units (BVG Associates (2012)), larger components and a harsher environment do, however, bring more risky and expensive operations. Thus to make offshore wind profitable, at the same time as the structures move further offshore and to deeper waters, the installation procedures have to be optimized.

This thesis addresses numerical simulation of the installation of XL monopile substructures for offshore wind turbines. Even if monopiles are the most frequently used support structures, few numerical studies have been performed on installation of these. In this thesis, the behaviour of a coupled installation system composed of a heavy lifting vessel and an XL monopile is studied. To predict the responses of this system, a numerical model is established in SIMO and simulations of the lowering phase of the installation are conducted.

The hydrodynamic system properties, used in the dynamic analysis of the system, are obtained from a frequency-domain analysis in HydroD. As these properties are time varying and obtained during steady-state conditions, they cannot be implemented directly in a non-stationary situation. The common simplification of conducting steady-state simulations in the most onerous position is thus utilized to study the effect of radiation damping from the XL monopile.

The issue connected to the time varying hydrodynamic properties, which occurs when the entire lowering operation is to be simulated, can be solved if strip theory is applied and the potential damping is neglected. Since the radiation damping of the XL monopile might affect the system responses considerably for moderate seas, the significance of simulating the entire lowering operation rather than conducting stationary simulations at the most intolerable position is also investigated.

From the eigenvalue analysis of the time-invariant model it is found that the XL monopile has a strongly depth-dependent natural period in pitch, which varies in the range of approximately T = 3.25 s to T = 4.65 s as the monopile is lowered. The eigenfrequency of the vessel pitch motion is, on the other hand, not affected by the chancing monopile draft and stays steadily at T = 8.89 s.

Regarding the coupled rotational and translational oscillations, the pendulum motions, they have higher eigenperiods than the other rigid body modes. In most sea states, the wave power close to these natural periods is too low to excite the motion. Due to the significant depth-dependency of these natural periods it is, nonetheless, important to investigate these pendulum effects especially at small drafts and in severe sea states, as they might be critical for the operation.

When the difference in the response spectral density obtained by an irregular and a regular wave analysis is investigated, it is found that the response collected from the regular wave analysis either corresponds to or is larger than the irregular analysis response. If the irregular wave spectrum has a peak which coincides with a resonance frequency, an exception to this tendency is observed. For such cases, the frequency resolution in the regular wave analysis might not be sufficient to capture the peak.

When the spectral peak period corresponds to the eigenfrequency of the motion studied, higher short-term extreme responses and standard deviations are found for the irregular analysis, as expected. If not, the estimated extreme responses is lower for the irregular analysis. The extreme responses in surge are, however, found to be more critical in the irregular wave analysis than in the regular. This deviates from the expectations and implies that a further study of these responses should be conducted.

When the radiation damping effect of the monopile is investigated, a significant reduction in the rotational resonance motion is observed when the potential damping is included both in short and longer waves. In the $T_p = 8$ s case, there is a peak in the spectrum corresponding to the spectral peak period of the wave spectrum. For this peak, no reduction is observed. This is due to the fact that this monopile motion is induced through the crane, by the increasing vessel motion, and is not affected by the radiation and diffraction of the monopile.

In the final part the significance of performing complete non-stationary simulations of the operation is investigated. The short-term extreme response in the lift wire, obtained from steady-state simulations at the most onerous position, is compared to the extreme responses obtained from repeated deployments to examine the effect of conducting non-stationary analyses. A significantly higher short-term extreme wire tension is observed for the steady-state simulations. This indicates that the simplification of conducting stationary simulations overestimates the responses and consequently may reduce the allowable sea states established for the operation.

In this Master's thesis only a few critical factors for the operation are studied. To accurately model the lowering of an XL monopile and establish operational limits on the basis of the obtained system responses, further work is required. Based on the analyses conducted, additional studies should be performed to further verify the results. Before well-founded operational limits can be established, shielding effects, wave spreading and nonlinear loads should also be taken into account.

Sammendrag

En betydelig økning i andelen energi levert av fornybare energikilder må finne sted dersom globale utslipp skal reduseres parallelt med at velferden øker i de nyindustrialiserte landene. Vindkraft er en av de bærekraftige ressursene som er anslått å levere en økende andel av denne kraften, på grunn av omfanget av uutnyttede ressurser som finnes offshore.

Kiełkiewicz et al. (2015) hevder at, med tanke på kostnad per megawatt generert kraft, er det mer gunstig å bruke vindturbiner med høyere kapasitet støttet på større monopiler enn å bruke turbinene som normalt brukes i dag. Selv om kapitalkostnadene avhenger mer av antall strukturer enn størrelsen på enhetene (BVG Associates (2012)), fører større komponenter og et røffere miljø imidlertid med seg mer risikable og kostbare operasjoner. For å gjøre offshore vindkraft lønnsomt, samtidig som strukturene flyttes lengre til havs og på dypere vann, må installasjonsprosedyrene derfor optimaliseres.

Denne avhandlingen tar for seg numerisk simulering av installasjonen av XL monopile støtter for offshore vindturbiner. Selv om monopiler er de mest brukte støttestrukturene, finnes det få numeriske studier som omhandler installasjon av disse. I denne oppgaven studeres oppførselen til et koblet installasjonsarrangement bestående av et tungløftsfartøy og en XL monopile. For å estimere responsene i dette systemet etableres en numerisk modell i SIMO og simuleringer av nedsenkningsoperasjonen utføres.

De hydrodynamiske systemegenskapene, som brukes i den dynamiske analysen av systemet, innhentes fra en frekvens-domene analyse utført i HydroD. Ettersom disse egenskapene er tidsvarierende og innhentet under steady-state betingelser, kan de ikke implementeres direkte i en ikke-stasjonær situasjon. Den mye brukte forenklingen, som går ut på å utføre steady-state simuleringer i den mest utsatte posisjonen, er derfor utnyttet når effekten av hydrodynamisk demping fra XL monopilen skal studeres.

Problemet knyttet til de tidsvarierende hydrodynamiske egenskapene, som oppstår når hele nedsenkningen skal simuleres, kan løses hvis stripeteori anvendes og den potensielle dempingen neglisjeres. Siden den hydrodynamiske dempingen fra XL monopilen kan påvirke responsene i systemet betraktelig ved rolig sjø, undersøkes også betydningen av å simulere hele nedsenkningen i stedet for å utføre stasjonære simuleringer med monopilen i kritisk posisjon.

Egenverdianalysen av den tids-invariante modellen indikerer at egenperioden til XL monopilen i stamp er svært dybdeavhengig og varierer fra omkring T = 3.25 s til T = 4.65 s når monopilen senkes. Egenfrekvensen til fartøyet i stamp påvirkes imidlertid ikke av den varierende dypgangen til monopilen og holder seg på T = 8.89 s.

Når det gjelder de koblete rotasjonene og translasjonene, pendelbevegelsene, har de

høyere egenperioder enn de andre modene. I de fleste sjøtilstander, vil ikke bølgeenergien nær disse egenperiodene være høye nok til å eksitere bevegelsen. Det er likevel viktig å studere disse pendeleffektene, spesielt ved lave dypganger og tøffe sjøtilstander, da dybdeavhengigheten kan føre til at disse effektene blir kritiske for operasjonen.

Fra sammenligningen av responsspektraltettheten oppnådd ved en uregelmessig og en regelmessig bølgeanalyse blir det funnet at responsene fra den regelmessige analysen enten korresponderer med eller er større enn responsen fra den uregelmessige. Dersom det uregelmessige bølgespekteret har en topp som sammenfaller med resonansfrekvensen observeres imidlertid et unntak fra denne tendensen. I slike tilfeller er muligens frekvensoppløsningen i den regelmessige analysen utilstrekkelig til å fange opp toppen.

Når peak-perioden i bølgespekteret sammenfaller med egenfrekvensen til bevegelsen som undersøkes, observeres som forventet høyere korttids ekstremresponser og standardavvik for den uregelmessige analysen. Ekstremresponsene i jag viser seg imidlertid å være mer kritisk i den uregelmessige analysen enn i den regelmessige. Dette avviker fra forventningene og impliserer at en videre studie av disse responsene bør utføres.

En betydelig reduksjon i resonansbevegelsen observeres når effekten av den hydrodynamiske dempningen fra monopilen undersøkes, både for korte og lengre bølger. I $T_p = 8$ s tilfellet, er det en topp i spektrumet som korresponderer med peak-perioden til bølgespekteret. For denne toppen, observeres ingen reduksjon. Dette kommer av at bevegelsen til monopilen skapes av den økende fartøysbevegelsen, via krana, og dermed ikke påvirkes av den hydrodynamiske dempningen fra monopilen.

I den siste delen av rapporten undersøkes betydningen av å utføre ikke-stasjonære simuleringer av hele operasjonen som studeres. Korttidsresponsen i løftewiren, funnet fra steady-state simuleringer i den mest utsatte posisjonen, sammenlignes med ekstremresponsene funnet fra gjentakende simuleringer av nedsenkningsoperasjonen for å undersøke betydningen av å utføre ikke-stasjonære analyser. Disse resultatene hentyder at forenklingen med å utføre stasjonære simuleringer overestimerer responsene og følgelig fører til at tillatt sjøtilstand for operasjonen minker.

I denne masteroppgaven undersøkes bare noen få kritiske faktorer for operasjonen. For å korrekt modellere nedsenkningen av en XL monopile og etablere de operasjonelle grensene på basis av de estimerte responsene kreves en del videre arbeid. Basert på de utførte analysene burde videre studier gjennomføres for å verifisere resultatene. Før velbegrunnede grenser kan etableres, burde også skjermingseffekter, bølgespredning og ulineære-effekter tas i betraktning.

Contents

List of Tables

List of Figures

List of Abbreviations

BWEA	The British Wind Energy Association
EWEA	The European Wind Energy Association
GW	Gigawatt
HLV	Heavy lift vessel
IEA	The International Energy Agency
LCOE	Levelised Cost of Energy
MW	Megawatt
OWT	Offshore Wind Turbine

List of Symbols

H_s	Significant wave height [m]
T_p	Spectral peak period [s]
p	Pressure
S	Wave spectrum
S_{XX}	Response spectrum
β	Wave propagating direction
δ	Phase shift
ϵ	Phase angle
ζ	Surface elevation
ζ_0	Wave amplitude
η	Body motion
η_{0j}	Amplitude of oscillation in the j-th degree-of-freedom, j=1, 2..6
λ	Wave length
ϕ	Velocity potential
ω	Wave frequency
∇	Gradient

Chapter 1

Introduction

1.1 Background

With today's increasing energy demand and the current climate change challenge, the need to develop competitive ways to utilize clean energy sources is getting urgent. If the global emission reductions envisioned are to take place simultaneously as the prosperity is rising in the newly industrialized countries, there has to be an intensive growth in the share of power supplied by renewable energies.

The British Wind Energy Association (BWEA) states that, among the world's sustainable sources of energy, wind power holds one of the most favourable combinations of security of supply, risk and cost of electricity generation (BWEA (2004)). According to the International Energy Agency (IEA), wind energy can provide 15 % to 18 % of the global energy demand by 2050 (IEA (2012)). To reach this target, rapid scaling up of annual installed wind power capacity, from 45 gigawatts (GW) in 2012, is required (IEA (2013)).

Even if onshore wind turbines have been deployed for decades to reduce the reliance on fossil fuels, future growth is limited due to factors like visual impact, noise and transport constraints. It is claimed that these elements have restricted the land-based turbines to a maximum capacity of (3 to 4) megawatts (MW) (The Crown Estate (2012)). Offshore, however, these restrictions can be loosened.

IEA (2013) states that the higher wind speeds and the lower turbulence intensity offshore can result in up to 50 % higher energy production from these plants than the ones onshore. Even if the capital cost is more than twice the one for onshore projects (Moné et al. (2015)), IEA (2013) predicts that offshore wind will provide a growing share and reach one third of all generated wind energy by 2050.

According to Thomsen (2014) the industry prefers to work with 4 different types of bottom-fixed foundations; monopile, gravity-based, jacket and tripod. Figure 1.1 shows the distribution for Europe's offshore wind turbines (OWT) at the end of 2015. As one can see from the illustration, 80.1 % of the wind turbines were founded on monopiles. Although the consent 4 or 5 years ago was that this type of foundation was not cost-effective at larger depths than 25 m to 30 m, this projection was revised and efficient solutions for water depths up to 40 m to 50 m are being researched today. Studies performed by Kiełkiewicz et al. (2015) have shown that with regards to cost per MW of rated power, the most favourable is to use higher capacity wind turbines supported on XL monopiles, monopiles exceeding approximately 7 m in diameter.

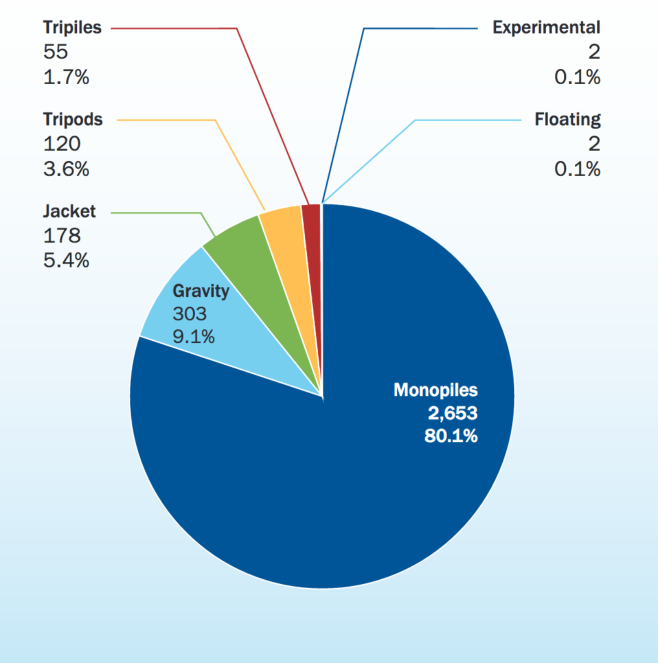

Figure 1.1: The distribution of offshore wind turbine foundations in Europe at the end of 2015 (EWEA (2015)).

To make offshore wind profitable and secure investors it is, however, critical that costs sink drastically. The Crown Estate (2012) found that the costs for projects at final investment decision in 2011 stabilised at a Levelised Cost of Energy[1] (LCOE) of about £140/MWh. To make offshore wind competitive with other low carbon power generation sources, The Crown Estate (2012) predicts that it has to reach a LCOE of £100/MWh by 2020.

As illustrated in Figure 1.2, the expenditure depend more on the number of turbines than the size of the unit. Higher rated power means fewer installation operations to achieve the same installed capacity. Since 18 % to 21 % of the capital costs come from the installation and assembly, compared to 6 % for land-based turbines (Moné et al. (2015)), an overall reduction in capital costs of approximately 4 % can be observed if the number of operations is cut in half (The Crown Estate (2012)).

---

[1] Lifetime cost of the project, per unit of energy generated (The Crown Estate (2012)).

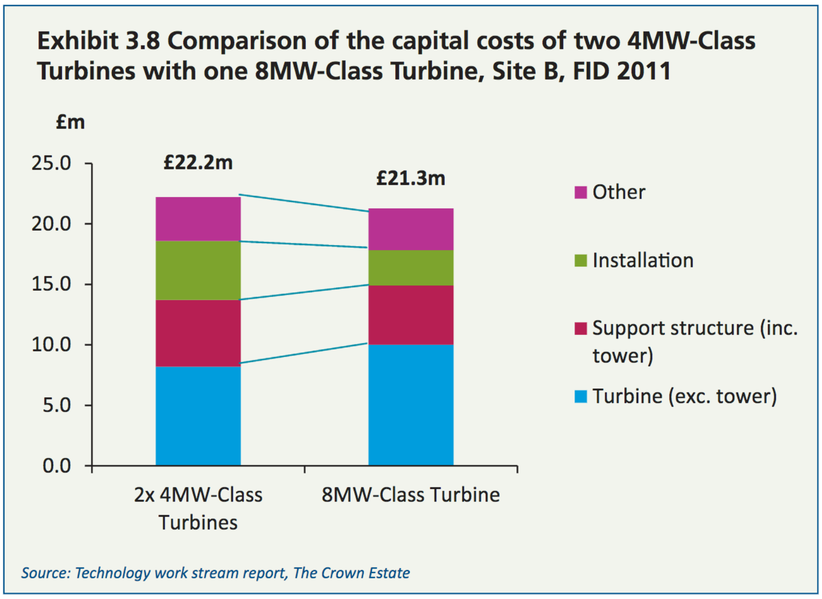

Figure 1.2: Capital costs of two 4 MW offshore turbines compared to one 8 MW turbine (BVG Associates (2012)).

The wind farms tend to move into deeper waters, as shown in Figure 1.3. This is a result of the search for greater environmental conditions for wind power generation and the lack of proper, available sites close to shore. Projects under construction, consented and planned confirm the same trend. According to the European Wind Energy Association (EWEA), the average depth and distance to shore at wind farms completed in Europe in 2015 were respectively 27.1 m and 43.3 km (EWEA (2015)).

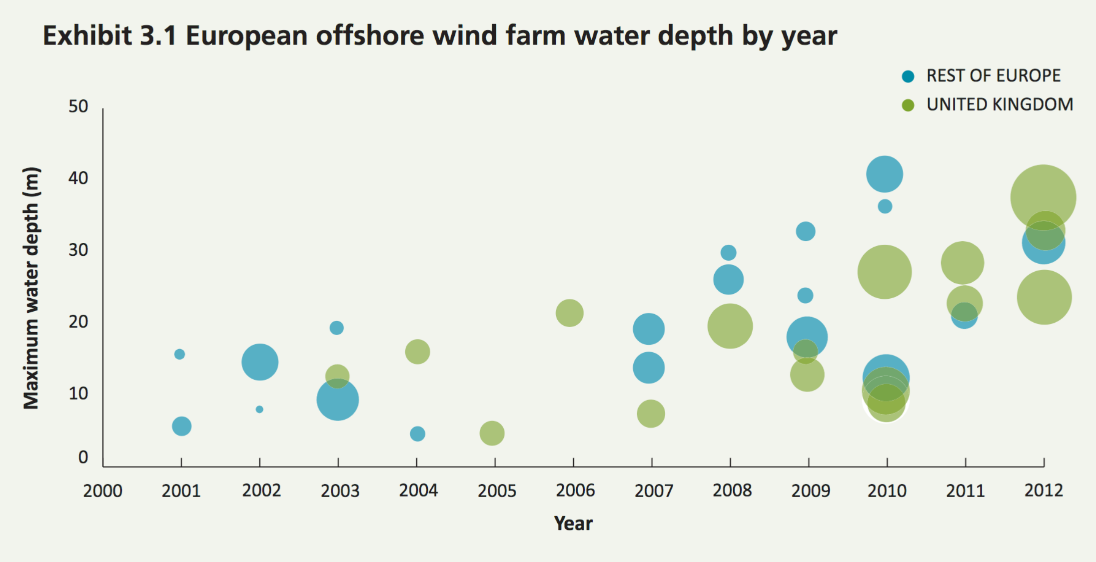

Figure 1.3: European offshore wind farm water depth by year (The Crown Estate (2012)).

To withstand greater loads, from a larger turbine and a harsher environment, bigger substructures are necessary. This brings new installation challenges. Since offshore operations already are risky and expensive, this will require even more robust installation methods. With costs of foundations, operations and electric infrastructure increasing with water depth and distance from shore, the cost reduction challenge is obviously huge, despite the higher level of generated energy at these sites. This is supported by Figure 1.4, which indicates how the capital costs of European offshore wind farms have increased in line with the trend to move further offshore and into deeper waters.

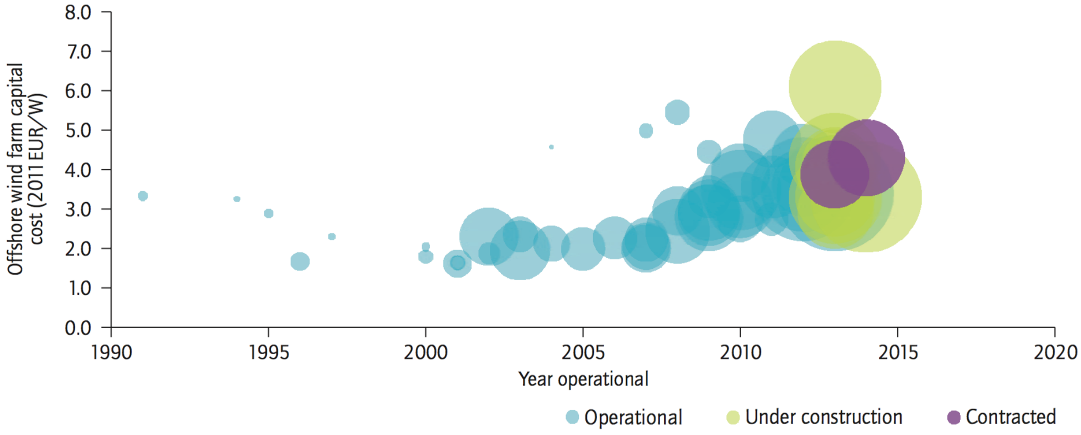

Note: the bubble diameter is proportionate to wind farm capacity; EUR/W = EUR per watt.

Figure 1.4: Capital costs of European offshore wind farms by year (IEA (2013)).

In the oil and gas industry, accurate numerical models have been made for years, by Mukerji et al. (1988) among others, to predict the interaction between a derrick vessel and the lifted object. Being able to estimate the design loads and the behaviour of the coupled system permits better planning of the operation, which can reduce the weather downtime. Reducing the downtime is a crucial factor in offshore wind industry, since the installation procedure is based on repetitive operations.

In a study performed by The Crown Estate it was found that, by increasing the average significant wave height working range from 1.4 m to 2.5 m, the weather downtime for an exemplified installation project could be reduced from around 33 % to 20 % (The Crown Estate (2012)). This shows the significance of being able to correctly estimate the system responses to reduce costs.

If the monopile has a large diameter, the wave-body interaction can cause significant radiation damping effects. Especially for short waves and moderate seas, which are typical wave conditions during installation, the potential damping may affect the responses on a monopile considered as a large-volume structure greatly. To obtain a correct damping model, it is thus important to investigate the effect of taking these hydrodynamic effects into account when the diameter of the monopile increases. If a precise model is established for the lowering operation and all damping contributions are taken into account, one can make sure that the responses are not overestimated.

1.2 State of the art OWT installation

The first offshore wind farms were small-scale projects, composed of few turbines installed in sheltered waters. At Middelgrunden wind farm outside Copenhagen, 20 turbines were installed in 2000, by the use of any makeshift equipment found available at short notice and low cost. Even though all the turbines were successfully installed at that site, the stakeholders realized that it would not be prudent to service exposed offshore sites in the same way as at this location. As a result, the industry started evolving. In view of this, Thomsen (2014) states that the Middelgrunden wind farm project marked the "entry into large-scale wind farm installation".

Today installation of turbines and bottom-fixed foundations largely rely on lifting operations, typically performed by a floating crane or a jack-up vessel that can provide a stable platform during lifting and mating. The jack-up principle may, however, cause a substantial downtime. Thus to reduce the duration of the positioning phase, more and more floating installation vessels are employed for foundation installation. These vessels are less weather sensitive during positioning, due to the fact that they lack an elevating system, which reduces the downtime in this phase notably.

Even if research on floating wind turbine concepts has intensified lately (Myhr et al. (2011), Muliawan et al. (2012), Karimirad and Moan (2011), Jonkman and Matha (2011), Gao et al. (2011)), Moan (2015) states that the development of floating support structures is still at an early stage. To date, only two full-scale floating OWTs are installed. So despite the fact that the floating OWTs, which have less water depth sensitive capital costs, have proven competitive at depths beyond 80 m, the monopiles will still play an important role in future developments.

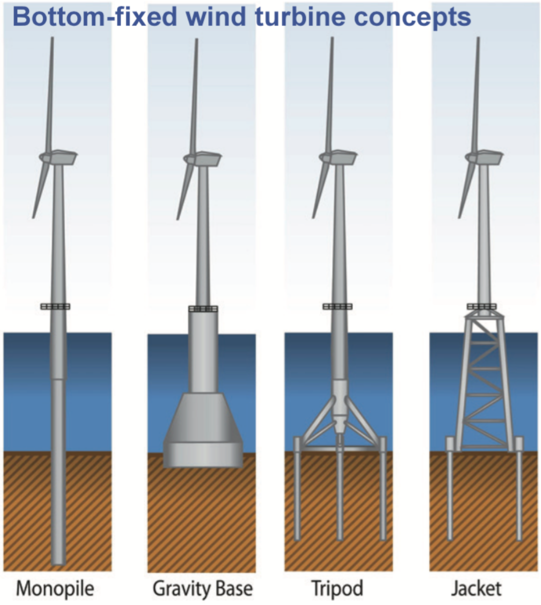

Figure 1.5: Various bottom-fixed foundations (Wiser (2011)).

In the subsequent sections current methods for installation of the bottom-fixed foundations illustrated in Figure 1.5 are presented and recently developed concepts for monopile installation are briefly discussed. As this thesis focuses on the installation of XL monopile substructures and different installation concepts are required for floating wind turbines, only installation of fixed foundations is presented in this section.

1.2.1 Monopile

A monopile foundation is basically a long steel or concrete tube, hammered or drilled into the seabed to a predetermined depth. The depth depends on the design load, soil conditions, water depth and environmental conditions, but typically 40 % to 50 % of the length is embedded into the bottom (Kaiser and Snyder (2010)). As previously mentioned the monopile is the most commonly used foundation type. This is due to structural simplicity and competitive costs of fabrication and installation (Thomsen (2014)).

Installation procedure for monopile foundation:

1. Transport to construction site: Monopiles may be transported to site by the installation vessel or a barge as in Figure 1.6, or they may be capped and wet towed (Herman (2002)). What way is preferred depends on numerous factors; the size of the monopile, the crane capacity, the distance to shore, environmental conditions and the transit speed.

Figure 1.6: Monopiles and transition pieces towed to site on a barge (ISKES (2016)).

2. Upending and lowering: After arrival at site the monopile has to be upended to a vertical position by the help of a crane. To wet tow and upend the monopile in water as shown in Figure 1.7 allows for the use of a smaller capacity crane, but at the expense of the operation's tolerance towards rougher weather conditions.

Figure 1.7: Wet tow, upending in water and positioning of monopile (Vellekoop (2015)).

As the crane used in this thesis work is not limiting for the operation, the XL monopile is assumed to be both transported and upended on board the installation vessel in this study. This procedure is illustrated in Figure 1.8 by the IHC IQIP 1400 t upending tool (IHC (2016)). How the numerical model is established for this case is further discussed in Chapter 4.

Figure 1.8: Upending on board the installation vessel by 1400 t upending tool (IHC (2016)).

New concepts are constantly being developed to reach maximum efficiency and cost effectiveness. Norwegian based NorWind proposed, in cooperation with Ulstein Group ASA, the new offshore wind foundation installation vessel in Figure 1.9 with a capacity to carry at least 24 piles. By the help of a Ulstein upending frame on starboard side, it is capable of safely upending the piles in wave conditions up to 2.5 m significant wave height (H_s) (OffshoreWind.biz (2011)). While for the Sheringham wind farm in UK, Knud E. Hansen A/S designed the upending trolley in Figure 1.9 which can upend monopiles delivered to a floating crane at site.

Figure 1.9: NorWind offshore wind foundation installation vessel and Knud E. Hansen upending trolley (OffshoreWind.biz (2011), K.E. Hansen A/S).

3. Driving/drilling operation: When the monopile is sitting vertically on the seabed, a hydraulic hammer is placed on top of it and it is driven into the seabed. To ensure an exact pile positioning a pile gripper is utilized. A rocky subsurface may prevent the driving operation. In that case, the monopile can e.g. be lifted into a pre-drilled hole like at the Bockstigen wind farm in Sweden and grouted into position by filling the gap between the structure and the rocky wall with concrete (4C Offshore Ltd (2016)).

   Sarkar and Gudmestad (2013), (2011), (2012) proposed a method to obtain a higher allowable sea state for performing the driving operation and increase the operability. They suggested using a pre-installed submerged support structure, to support the monopile in the initial phase of the driving operation. Their concept is to wet tow the monopile and at site remove the top end-cap, fill the monopile with ballast water to upend it and position it in the guide frame connected to the supporting structure.

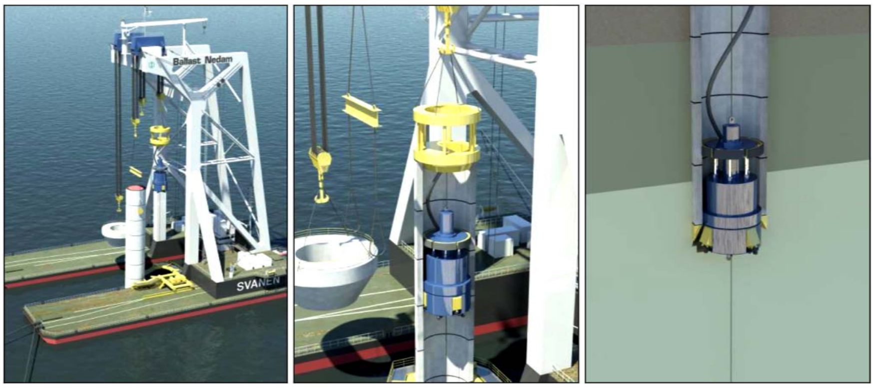

Figure 1.10: The monopile is upended before a drilling machine is installed in the pile and it is drilled to a predetermined depth (Vattenfall Wind Power AB (2009)).

   For a Vattenfall research project, Ballast Nedam and MT Piling developed a new concept consisting of prefabricated concrete monopiles installed by a vertical drilling method. The concrete concept is proposed to give lower material expenses, less vulnerability to market related price fluctuations and higher production capacity. In addition, this method will not require the use of both driving and drilling operations, not even at sites with likely occurrence of boulders (4C Offshore Ltd (2016)). As illustrated in Figure 1.10 the concrete pile is upended and positioned within a guiding frame, before the machine used for drilling is installed inside the monopile.

4. Installation of transition piece: The pile-driving operation may lead to the steel becoming brittle and ineligible for large load bearing. Typically this problem is solved by fitting a transition piece, a pile with a bigger diameter, on top of the monopile over a length of 6 m to 8 m (Thomsen (2014)). When it has been adjusted to true perpendicularity it is grouted onto the pile, and the wind turbine tower is installed on the transition piece.

1.2.2 Gravity-based

A gravity-based foundation is basically a huge concrete or steel structure that uses its weight to withstand the loads generated by the wind turbine and the offshore environment, i.e. it relies on its mass, including ballast, to secure the structure to the seabed.

This type of concept has been used successfully at sites like Middelgrunden in Denmark and Thornton Bank in Belgium. Common for the sites are the shallow water and the semi hard, uniform seabed conditions unsuited for pile driving. Concrete requires minimal maintenance and is a low-priced material, but the foundation's size, weight and need for subsurface preparation like dredging and backfilling makes this type of foundation very expensive and time consuming to install.

Installation procedure for gravity-based foundation:

1. Storage: A gravity-based foundation is typically cast in steel-reinforced concrete by the use of a prefabricated mold. This makes it difficult to manufacture a large number of foundations at the same time. To deal with this, the contractor typically sets up 6 to 8 molds and starts the manufacturing 9 to 12 months prior to the installation. As a result, a large number of foundations have to be handled and stored.
2. Transport to construction site: The foundations can be transported on an installation vessel or a barge or they can be wet towed to the installation site.
3. Lowering: If the foundations are dry-transported to the site, they will be lifted and lowered into place on the seabed by a high capacity crane, at arrival. Are they wet towed, on the other hand, the foundations are ballasted and sunk into the right positions at the seabed with the help of a lower-capacity lifting vessel.
4. Ballasting: When the foundation is installed successfully on the ocean floor, ballast, in the form of e.g. sand or water, is pumped into the structure and scour protection is provided.

1.2.3 Jacket and Tripod

A jacket foundation is a lattice structure. The idea of this type of support is to minimize the cross section of the structure in the splash zone, i.e. shrink the surface that passing waves can attack, to reduce the environmental loads on the foundation by the waves. As opposed to the other foundations mentioned, that have a large tube protruding out of the water, the jacket is constructed of small-diameter tubular members. This allows the structure to withstand large forces and be lightly built, but at the expense of manufacturing ease.

A tripod is a foundation composed of one large, central pole connected to three steel tubes. Above the surface it looks like a monopile with a relatively small cross section in the splash-zone. Due to its three cylindrical legs that provide a stable foundation it has proven useful at deeper sites and varying soil conditions. That the tripod is heavier and more expensive to manufacture and install than the monopile makes it less cost effective in shallow waters.

Installation procedure for jacket- and tripod foundation:

1. Storage: The jackets have to be manufactured early to avoid downtime during installation. 4 to 6 weeks fabrication time per jacket has to be planned for in terms of onshore storage space and time consume (Thomsen (2014)). Given that this type of foundation usually has a footprint of around 24 m x 24 m and a length of 50+ m, due to its cost effectiveness in deeper waters, storage will be a challenge for the jackets as the number of units increase and the projects move to deeper waters.
2. Transport to construction site: Both types of foundations are usually barged to the construction site and lifted into place by a heavy lifting vessel.
3. Post-/pre-piling: To secure the jacket foundation against lateral forces, anchor piles are either driven through the base of the foundation and into the seabed or the jacket is placed over pre-driven piles. To fit the jacket to the anchor piles, pile sleeves at each corner of the jacket are grouted to the pile or deformed to keep the pile in place. Similar to the jacket, the tripod is secured to the seabed by anchor piles.

Table 1.1 roughly summarizes the most common transportation- and installation procedures discussed above. As briefly mentioned in Sec. 1.2.1, the XL monopile further studied in this thesis is assumed to be dry-transported, upended on board and lowered towards the seabed by a high capacity crane.

Table 1.1: Transportation and installation methods for bottom-fixed foundations (Li (2016)).

Type of foundation	Transportation	Installation
Monopile	Dry-transported	Upended & lowered
	Wet-towed (end-caps)	Upended & lowered (smaller crane)
Gravity-based	Dry-transported	Lifted & lowered (large crane)
	Wet-towed (large foundation)	Ballasted & lowered (smaller crane)
Jacket/Tripod	Dry-transported (upright position)	Lifted & lowered; pre-or post-piling
	Dry-transported (horizontal position)	Upended and lowered; pre- or post-piling

1.3 Scope, objectives and limitations of the thesis

To reduce the LCOE for offshore wind farms, simultaneously with the tendency to install larger turbines further from shore, installation methods have to be optimized and the weather downtime minimized. This can be obtained by improving the operational procedures and the numerical methods used to simulate the responses in the system of interest. If an accurate numerical model of the installation operation can be developed, one can ensure that the predicted system responses are not exaggerated.

The main objective of this thesis is therefore to accurately numerically model the lowering operation for installation of an XL monopile, to estimate the responses in this coupled system. Based on the challenges identified in the previous sections and the literature review in Chapter. 2 the listed sub-objectives are thus established to achieve the main objective.

- Develop a time-invariant model of the vessel and the monopile and investigate the governing motion modes and natural frequencies of the coupled lifting system
- Compare the responses obtained from a regular wave analysis, with the responses obtained from an irregular wave analysis
- Investigate the effect of diffraction and radiation from the XL monopile at steady-state conditions
- Establish a time-variant model based on strip theory and study the difference between the responses obtained from steady-state simulations and the ones obtained from non-stationary simulations to examine the significance of simulating the entire lowering operation

Conventional lifting operations for installation of bottom-fixed wind turbines require moderate sea states, typically with a significant wave height (H_s) below 2.5 m (Li (2016)). To assume the response quantities to depend linearly on the wave process is often sufficient for such operations, even if this assumption might be questioned for rougher seas. This is supported by Haver (2016), whom states that for sea states where marine operations are likely to be performed, this assumption will most often be acceptable. In this thesis the response contributions from the non-linearity in waves is thus assumed to be negligible and only linear wave theory is applied to compute the wave forces.

To simplify the study, neither wind nor current forces are included in this thesis and only head sea is taken into account. The work is further limited to the modelling of undisturbed, long-crested waves. The effects of wave spreading and shielding from the vessel, on the system responses, are i.e. not considered. How these simplifications affect the results is further discussed in Chapter 7.2.

This thesis only focuses on the lowering of the XL monopile substructure. To obtain a solid basis for establishing operational limits for the complete installation process, the work has to be extended to consider the docking- and hammering phase of the operation.

In the lowering operation studied, the total mass, the damping and the stiffness varies as the monopile is lowered towards the seabed. If these system properties are obtained from a frequency-domain analysis, they will be expressed by the boundary conditions on the mean body wetted surface. This causes them to become non-applicable in a time-domain simulation of the lowering. To assess the issue of the time-varying system properties, the case is either simplified to steady-state simulations at a critical system configuration or to non-stationary simulations of a model based on strip theory.

1.4 Outline of the thesis

Chapter 2 gives a review of what knowledge is already out there. This chapter introduces relevant results found from numerical simulations of offshore lifting operations, with focus on issues like mechanical- and hydrodynamic couplings of the considered bodies. Aspects of time-variant system properties are also expanded upon.

Chapter 3 provides theoretical background information for the studies performed in the thesis.

Chapter 4 presents the lifting vessel and the XL monopile, in addition to the features of the numerical model of the coupled system. This chapter also describes the numerical methods utilized in the study. Additionally it briefly presents the numerical tools used to conduct the various types of analyses.

Chapter 5 addresses the dynamic analyses performed for regular and irregular wave realisations at steady-state conditions. The frequency-domain analysis performed in HydroD is described and the procedure to establish a time-invariant model is presented. Governing motion modes are established and the depth-dependency of their corresponding natural frequencies is discussed. This chapter covers all the results obtained to compare the responses obtained from a regular- and an irregular wave analysis.

Chapter 6 describes the approach used to create a time-variant model and to conduct a non-stationary load and response analysis. The effect of monopile radiation damping is studied by comparing the responses at steady-state conditions, with and without potential damping included. In this chapter the responses obtained from stationary analyses conducted with the monopile in the most onerous position is also compared to the responses found from a non-stationary analysis of the whole lowering process.

Chapter 7 states the conclusion of the thesis and gives recommendations for future work.

Chapter 2

Literature review

Nielsen (2007) states that marine operations are intermediate phases for a structure. In these phases, the conditions differ from the ones for the structure at a permanent state, which are normally considered during design. To ensure that the operations are conducted within recognised safety levels, more extensive studies are required as the complexity of the operations increases.

Nielsen (2007) argues that even if practical experience still plays an important role in the design of marine operations, an increasing need to determine the operational limits based on quantified responses will occur as new types of operations are to be executed. A few studies, expanded upon in Sec. 2.1, have been published regarding establishing operational limits.

Offshore lifting operations have been extensively investigated through numerical simulations and experiments over several years, due to their role in the oil and gas industry. There are numerous published studies, which have centred on the interactions between the responses of the derrick vessel and the hanging load, in addition to the hydrodynamic coupling of the vessel and a transport barge (Mukerji et al. (1988), van den Boom et al. (1988), Baar et al. (1992)). Some relevant results of these studies is further discussed in Sec. 2.3.

Unlike the installations in the oil and gas industry, which tend to be unique, repetitive operations are performed for the units in an offshore wind farm. Thus, in this industry the ability to build accurate numerical models to predict the system behaviour is even more crucial for efficient installation operations.

Nonetheless, few publications are found regarding the lowering operation of a monopile substructure for offshore wind turbines. There are no published studies, known to the author, which addresses the numerical simulation for installation of XL monopile substructures.

2.1 Operational limits

Clauss et al. (1990) investigated the limiting conditions of crane vessel operations by model tests and accompanying calculations. They selected the vertical load motion as limiting parameter and established the operational limits in terms of H_s for crane operations performed by a barge, a ship and a semisubmersible. Cozijn et al. (2008) established the operational limits for the installation of two top-side modules by a dynamic positioned vessel, from hydrodynamic scale model tests and computer simulations.

Matter et al. (2005) went a step further and developed a methodology connecting the results of a structural analysis of a deployment/retrieval operation for a jack-up to a hydrodynamic motion analysis, resulting in the operational limits in terms of H_s and T_p that would guarantee the structural integrity of the unit. While Ringsberg et al. (2015) studied how the operable weather window for such an unit could be increased by taking site-specific parameters as soil type and water depth into account and proposed a method to assess the weather window with these implemented.

Berg et al. (2015) studied how to date, the operational limits have been generally established based on previous experience with similar operations. They found that in few cases, the actual dynamics of the vessel for which the equipment are to be installed is considered and the suppliers usually end up with limits determined only by H_s. Berg et al. (2015) suggests that methods for specifying work task-specific limits should be developed. To get a weather window as wide as possible, the dynamics of the vessel, the environmental conditions and the type of equipment should be studied.

Li et al. (2016b) determined the allowable sea states for an installation operation for a bottom-fixed offshore wind turbine by different numerical approaches. They investigated which factors are crucial to include in the numerical modelling to achieve an accurate basis for establishing the operational limits. In Li et al. (2016a) they developed a methodology to establish the operational limits, based on the values obtained for the limiting parameters identified by the different numerical approaches.

2.2 Hydrodynamic load analysis for lowering process

During the lowering process, the varying submergence of the monopile makes the dynamic features of the system change continuously. It is critical for the quality of the simulation to select proper time-variant system properties, e.g. added mass, damping, wire stiffness etc., for the response analysis of the lifting system. Normally, computational fluid dynamics approaches or model tests are required to determine accurate hydrodynamic coefficients. To determine hydrodynamic mass and damping of a ventilated pile, Perry et al. (2005) e.g. utilized the oscillation decay model test.

An operation governed by transient or highly non-linear responses requires to be studied in a different manner than that of a stationary case. Sandvik (2012) studied two different approaches to simulate such a case. In the first approach stationary simulations are performed in irregular waves with the lowered object in the most intolerable position and in the second method repeated lowering runs are simulated with different irregular wave realizations. Sandvik (2012) found that the most precise estimates are found by analysing the entire lowering operation, because the unrealistic build-up of oscillations observed in the first approach is avoided.

Morison et al. (1950) developed a method to estimate the forces, exerted by surface waves, on a pile extending from the seabed and through the free surface. Low frequency waves cause low wave generating from the wave-body interaction and the incident waves on a small-volume structure will as a result not be considerably disturbed by the body. Due to the simple shape and small diameter of the monopile substructures, strip theory based on Morison's formula with varying draft has thus been utilized by Li et al. (2013), among others, to approximate the wave forces on a slender structure.

Li et al. (2015) examined the significance of taking into account potential damping during the lowering of a monopile substructure. They found that the conventional Morison's formula may overestimate the responses of the lifting system because the diffraction and radiation of the monopile is disregarded. Li et al. (2015) also developed a new approach to implement the radiation damping of the monopile in the time-domain numerical simulation.

2.3 Hydro-mechanical coupling

Baar et al. (1992) investigated the hydro-mechanical coupling effects arising during the lifting of a heavy load from a transport barge by means of a crane vessel. They found that, whilst the hydrodynamic coupling hardly affected the responses of the crane tip, the transport barge motions could be significantly altered due to the presence of the large crane vessel. This is supported by Li et al. (2014) whom performed numerical simulations of the entire lowering of a monopile substructure and observed that a reduction in the extreme responses of lifting operations can be achieved if the lifting is performed in the vicinity of a properly headed crane vessel.

Park et al. (2011) studied how crane boom elasticity affects the system responses during a lifting operation by conducting simulations with both an elastic boom and a rigid boom. The dynamic factor analysis showed a difference of only 1.0 % to 4.3 % between the two systems, depending on wave heading and cargo, when a mass of 30 % of the crane capacity is lifted.

Li et al. (2013) conducted numerical sensitivity analyses on the effects of gripper device- and landing device stiffness during the lowering of a monopile substructure. It was found that a suitable gripper device stiffness should be chosen, to restrain the relative motion of the monopile and the gripper, because a significant stiffness dependence is observed. They also found that the landing contact force in the landing phase grows considerably by applying a greater landing stiffness.

These findings later proved to be only essential in the coupled model for the hammering process. When Li et al. (2015) executed their analysis of the radiation damping effect during lowering, the gripper device was excluded from the numerical model. This was done because it was found that the hydraulic cylinders in the device in reality would be retracted and reveal a larger gap than what was modelled by Li et al. (2014). Since contact between the monopile and the gripper always should be avoided, do to the cylinders high stiffness, the relative motion of the monopile and the installation vessel was used as a limiting parameter and the gripper was excluded from the model.

Chapter 3

Linear wave induced motions and loads

The intention of this chapter is to provide the theoretical background on waves and wave induced motions, needed to evaluate the behaviour of the coupled installation system. Theory presented in this section is mainly obtained from Faltinsen (1993) or from the complementary material by Greco (2012), based on the book. The theory about response analysis is also collected from Haver (2016). Readers with a non-mathematical background should be able to understand this material, but it is assumed that the reader has a basic knowledge of fluid mechanics.

3.1 Potential theory

Potential theory is based on the assumption that the fluid motion is irrotational and the sea water incompressible and inviscid. Due to these assumptions the fluid velocity vector **V** can be described by the gradient of a scalar variable, ϕ (Faltinsen (1993)):

$$\mathbf{V} = \nabla\phi = \mathbf{i}\frac{\partial\phi}{\partial x} + \mathbf{j}\frac{\partial\phi}{\partial y} + \mathbf{k}\frac{\partial\phi}{\partial z} \tag{3.1}$$

The velocity potential, ϕ, has no physical meaning itself, but it is useful in the mathematical analysis of the fluid. To find this velocity potential, the Laplace equation, Eq. (3.2), with proper boundary conditions has to be solved. For more details on boundary conditions ref. (Faltinsen (1993)).

$$\nabla^2\phi = \frac{\partial^2\phi}{\partial x^2} + \frac{\partial^2\phi}{\partial y^2} + \frac{\partial^2\phi}{\partial z^2} = 0 \tag{3.2}$$

Faltinsen (1993) states that the finite water depth waves, described by the velocity potential in Eq. (3.3), have a corresponding wave profile, which can be described by Eq. (3.4).

$$\phi = \frac{g\zeta_0}{\omega}\frac{coshk(z+h)}{coshkh}cos(\omega t - kx) \tag{3.3}$$

$$\zeta = \zeta_0 sin(\omega t - kx) \tag{3.4}$$

where ω is the wave frequency, ζ_0 is the wave amplitude, k is the wave number and h is the average water depth.

In potential theory the linear loads are found by integrating the pressure described in Eq. (3.5), which follows from Bernoulli's equation, along the wetted body surface.

$$p = \underbrace{-\rho\frac{\partial\phi}{\partial t}}_{\text{dynamic}} \underbrace{-\rho g z}_{\text{hydrostatic}} \tag{3.5}$$

The dynamic pressure forces are found by integrating along the mean body wetted surface, while the hydrostatic forces are obtained by integrating on the instantaneous body surface (Greco (2012)). Based on this, the generalized hydrodynamic forces can be obtained by Eq. (3.6):

$$F_k(t) = -\rho\int_{S_{0B}}\frac{\partial\phi}{\partial t}n_k dS, k = 1, 2..6 \tag{3.6}$$

where n$_k$ is the generalized normal vector, S$_{0B}$ is the mean body wetted surface and ϕ is the wave velocity potential. The components for F$_k$ are forces for k = 1..3 and moments for k = 4..6.

The linearisation of the case permits decomposition of the velocity potential according to Eq. (3.7):

$$\phi = \phi_R + \phi_D \tag{3.7}$$

where ϕ_R is the radiation velocity potential and ϕ_D is the total diffraction velocity potential, which denotes the sum of the incident wave potential and the disturbance due to the presence of the body (Det Norske Veritas (2010b)). This is further discussed in Sec. 3.2.

3.2 Hydrodynamic Forces

Faltinsen (1993) states that if one assume linearity and steady state conditions, which implies that the response oscillates with the frequency of the disturbance, the hydrodynamic problem can be split into two sub-problems. The following sub-problems, A and B, can be solved separately and added, to give the total solution.

A: Radiation problem: The body is forced to oscillate in its 6 degrees-of-freedom with the wave excitation frequency. For this case there are no incident waves and the resulting hydrodynamic loads are *added mass*, *damping* and *restoring* terms.

B: Diffraction problem: It is assumed that the body is restrained from oscillating and is interacting with incident waves. The hydrodynamic loads for this case are called *wave excitation loads*. These loads are made up of Froude-Kriloff and diffraction forces and moments.

Induced loads and motions on marine structures from wave-body interaction, depend on the relative dimensions and flow effects involved. According to Faltinsen (1993), a simple figure like Figure 3.1 is useful to state the relative importance of viscous effects and potential flow effects for the hydrodynamic forces affecting the structure under consideration.

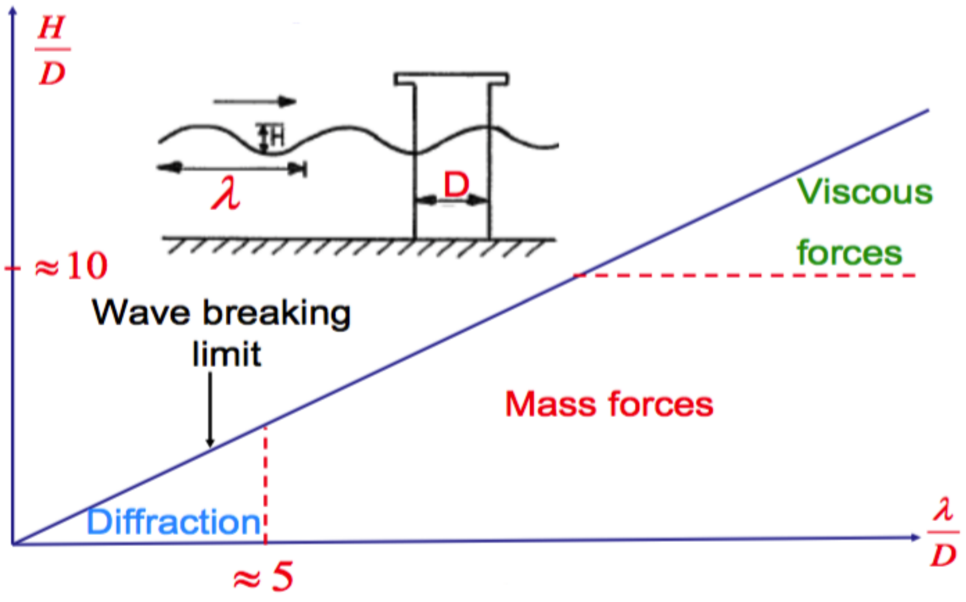

Figure 3.1: Relative importance of viscous effects and different types of potential flow effects like diffraction and radiation (Faltinsen (1993)).

Based on the results in the illustration one can state the following:

- For λ/D<5: loads induced by incident waves and their diffraction are important.
- For λ/D>$\approx$5: structure is so slender that incident waves tend to be unaffected.
- For H/D>$\approx$10 and λ/D$\gg$5: viscous loads become dominant.

This figure is determined by the use of a bottom-fixed, vertical cylinder penetrating the free surface. Morison's equation, further discussed in Sec. 3.4, with a mass- and drag coefficient of respectively 2 and 1, is utilized to find the horizontal wave forces the figure is based on. In addition, linear McCamy & Fuchs theory, described in Sec. 3.5, is used in the wave diffraction regime. D is the diameter of the pile, H represents the wave height of the regular, incident waves, while λ is the wave length.

When evaluating the responses in the coupled lifting system, induced by the waves, the notations in Figure 3.2 are utilized. Here η_1, η_2 and η_3 describe the translational motion, while η_4, η_5 and η_6 describe rotational motion.

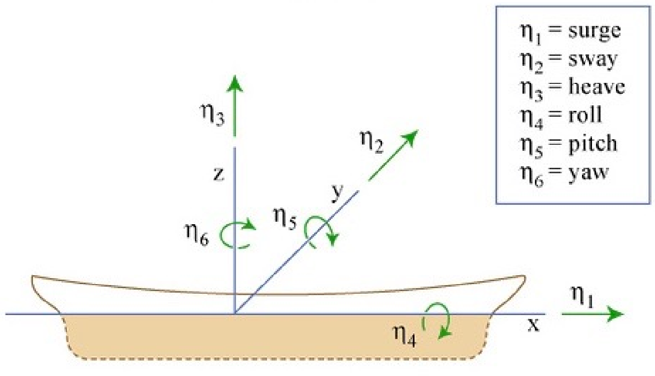

Figure 3.2: Sign convention for translatory and angular displacements (MIT OCW (2005)).

When the body is forced to oscillate in its 6 degrees-of-freedom (DOF) according to Eq. (3.8), as in case A, radiated waves are generated and the body is subjected to hydrodynamic loads identified as added mass, damping and restoring (Greco (2012)).

$$\eta_j(t) = \eta_{0j}\cos(\omega t), j = 1, 2..6 \tag{3.8}$$

Here j = 1, 2..6 represents surge, sway, heave, roll, pitch and yaw motion, respectively. η_{0j} is the amplitude of the oscillation in the j-th DOF. How the buoyancy varies when the body moves affects the restoring terms, which are connected to the hydrostatic pressure. These generalized restoring loads can be described by Eq. (3.9), where C_{kj} are the restoring coefficients.

$$F_{hydr,k}(t) = -\sum_{j=1}^{6} C_{kj}\eta_j, k = 1, 2..6 \tag{3.9}$$

The motions of the oscillating body determine the added mass and damping, as these loads are connected to the dynamic pressure induced by these motions. Thus the radiation forces can be described by Eq. (3.10):

$$F_{rad,k}(t) = -\int_{S_{0B}} \rho\frac{\partial\phi_R}{\partial t}n_k dS = \sum_{j=1}^{6}\{A_{kj}\ddot{\eta_j} - B_{kj}\dot{\eta_j}\}, k = 1, 2..6 \tag{3.10}$$

where S$_{0B}$ is the mean body wetted surface, ϕ_R is the radiation velocity potential, n$_k$ is the normal vector, $-A_{kj}\ddot{\eta_j}$ is the load proportional to the body acceleration and $-B_{kj}\dot{\eta_j}$ is the load proportional to the body velocity.

Wave excitation forces and moments are, as initially stated, the loads on a fixed body affected by incident waves. The Froude-Kriloff force, caused by the dynamic pressure induced by undisturbed incident waves, constitutes a part of the total excitation force and can be described by Eq. (3.11):

$$F_{FK,k}(t) = -\int_{S_{0B}} p_0 n_k dS = \int_{S_{0B}} \rho\frac{\partial\phi_0}{\partial t}n_k dS, k = 1, 2..6 \tag{3.11}$$

where S$_{0B}$ is the mean body wetted surface, ϕ_0 is the incident wave velocity potential and n$_k$ is the normal vector.

By itself, this undisturbed pressure force indicates an undisturbed velocity field. As this is unphysical with a body present, the total force must be comprised of an additional component. This part, given in Eq. (3.12), is a diffraction force, caused by the change in the undisturbed pressure field due to the presence of the body (Faltinsen (1993)).

$$F_{D,k}(t) = \sum_{j=1}^{6}(\bar{a}_{0j}A_{kj} + \bar{u}_{0j}B_{kj}), k = 1, 2..6 \tag{3.12}$$

Here $\bar{a}_{0j}$ and $\bar{u}_{0j}$ are to be evaluated at the geometrical mass centre of the body. A_{kj} and B_{kj} are the added mass- and the damping coefficients, respectively.

These loads appear as radiation loads, as they exist due to the forced flow in opposite direction of the incident waves, generated by the wave-body interaction to ensure body impermeability (Greco (2012)). It is, as stated in Eq. (3.13), the combination of the diffraction- and the incident wave dynamic pressure, that determine the excitation forces (Greco (2012)).

$$F_{exc,k}(t) = \underbrace{-\int_{S_{0B}} \rho \frac{\partial \phi_0}{\partial t} n_k dS}_{\text{Froude-Kriloff loads}} \underbrace{- \int_{S_{0B}} \rho \frac{\partial \phi_{Diff}}{\partial t} n_k dS}_{\text{Diffraction loads}}, k = 1, 2..6 \tag{3.13}$$

S_{0B} is the mean body wetted surface, ϕ_0 is the incident wave velocity potential, ϕ_{Diff} is the velocity potential which describes the disturbance due to the presence of the body and n_k is the normal vector.

3.3 Linear wave induced responses

3.3.1 Linear response system

A useful consequence of linear theory is that an irregular sea surface, closer to real ocean waves than harmonic waves (Eq. (3.4)), can be modelled by adding together several regular waves with varying amplitudes, wavelengths and propagation directions. If long-crested waves is assumed, the wave elevation of an irregular sea propagating along the positive x-axis can be written according to Eq. (3.14):

$$\zeta(x,t) = \sum_{n=1}^{N} \zeta_{0,n} sin(\omega_n t - k_n x + \epsilon_n) \tag{3.14}$$

where $\zeta_{0,n}$, ω_n, k_n and ϵ_n is the wave amplitude, the wave frequency, the wave number and a random phase angle of wave component n, respectively.

If a harmonic wave component at x = 0, described by Eq. (3.15), induces a motion in a linear response system, the steady state response will be a harmonic function of time too. The response will have an identical frequency, an amplitude that is a linearly scaling of the wave amplitude and a phase, δ, which indicates that the response is to some extent shifted in time compared to the wave process as shown in Eq. (3.16).

$$\zeta_n(t) = \zeta_{0,n} sin(\omega_n t + \epsilon_n) \tag{3.15}$$

$$x_n(t) = x_{0,n} sin(\omega_n t + \epsilon_n + \delta_n) = RAO(\omega_n)\zeta_{0,n} sin(\omega_n t + \epsilon_n + \delta(\omega_n)) \tag{3.16}$$

The response amplitude operator (RAO), is the ratio of response amplitude, $x_{0,n}$, to wave amplitude $\zeta_{0,n}$. Important to note is that the RAO only provides information about the amplitude scaling so if phase information is needed, the complex valued transfer function must be obtained (Haver (2016)).

From basic hydrodynamics it is found that the relation between the spectral density function for the wave process, $S(\omega_n)$, and the wave amplitude, $\zeta_{0,n}$ is given by Eq. (3.17) (Pettersen (2007)).

$$\frac{1}{2}\zeta_{0,n}^2 = S(\omega_n)\Delta\omega \tag{3.17}$$

Based on this, the response spectrum $S_{XX}(\omega_n)$ for the response process can be described by Eq. (3.18).

$$S_{XX}(\omega_n) = \frac{x_{0,n}^2}{2\Delta\omega} = \frac{[RAO(\omega_n)]^2\zeta_{0,n}^2}{2\Delta\omega} = [RAO(\omega_n)]^2 S(\omega_n) \tag{3.18}$$

Here the sea state is characterized by the wave spectrum, S(ω), and the response properties are specified by the absolute value of the transfer function, $RAO(\omega_n)$. When such an approach is utilized, the problem is solved in the frequency domain (Haver (2016)), which is the method used to solve the linear response problems in Chapter 5.

3.3.2 JONSWAP spectrum

The wave spectrum, S(ω) that characterizes the sea state in this thesis, is the 3-parameter JONSWAP spectrum. This spectrum is empirically determined from data collected at a shallow site in the North Sea, relatively close to shore, and is considered to be a reasonable model for wind sea in the range given in Eq. (3.19) (Pettersen (2007)).

$$3.6\sqrt{H_s} \leq T_p \leq 5\sqrt{H_s} \tag{3.19}$$

The JONSWAP spectrum has 5 parameters, but in this report the mean values, specified by Hasselmann et al. (1973) whom established the spectrum, are used for the spectral parameter, σ. Due to this, there is only a peak frequency, ω_p, a spectral parameter, α, and a peakedness parameter, γ, left that have to be assigned values.

The values used in the study is thus σ_a = 0.07, σ_b = 0.07 and γ = 3.3. α depends on γ, H$_s$ and T$_p$ and is therefore computed from Eq. (3.20).

$$\alpha = 5.061\frac{H_s^2}{T_p^4}(1 - 0.287 ln\gamma) \tag{3.20}$$

The spectrum is given by Eq. (3.21) (MARINTEK (2009)). This formula is utilized in all the analyses conducted in Chapter 5 and 6. Even if a sixth parameter, the form parameter, β, is defined in the formula given for the spectrum by (MARINTEK (2009)), this is just assigned the default value of 1.25.

$$S(\omega) = \frac{\alpha g^2}{\omega^5} exp\Big(- \beta \Big(\frac{\omega_p}{\omega}\Big)^4\Big) \gamma^{exp\Big(- \frac{(\omega/\omega_p - 1)^2}{2\sigma^2}\Big)} \tag{3.21}$$

3.3.3 Short term analysis of system response

The combination of H$_s$ and T$_p$ define the JONSWAP spectrum and thus characterizes a short term sea state. For a system where the response quantities are assumed to depend linearly on the wave process, the response spectrum is given by the absolute value of the transfer function, RAO, and the wave spectrum as presented in Eq. (3.18). From this spectrum, the spectral moments can be found by Eq. (3.22):

$$m_{X,N} = \int_0^\infty \omega^N S_{XX}(\omega) d\omega \tag{3.22}$$

where ω is the wave frequency and S$_{XX}(\omega)$ the response spectrum.

Based on these spectral moments, the variance, σ^2 and the zero-up-crossing period, t_{Xm02}, for the response process can be computed.

$$\sigma_X^2 = m_{X,0} \tag{3.23}$$

$$t_{Xm02} = 2\pi \sqrt{\frac{m_{X,0}}{m_{X,2}}} \tag{3.24}$$

According to Haver (2016), the response process for this linear quantity can be modelled as a Gaussian stochastic process. They state that a small deviation between the modelled process and the surface process usually gets filtered away by the load process. The global maxima for the response process are thus assumed to be distributed according to the Rayleigh distribution given in Eq. (3.25).

$$F_{X_G}(x) = 1 - exp\Big\{ - \frac{1}{2}\Big(\frac{x}{\sigma_X}\Big)^2\Big\} \tag{3.25}$$

To find the response value expected to be exceeded once for the response process modelled, the expression in Eq. (3.26) can be utilized. Here the probability of exceedence equals 1 over the number of zero-up-crossing response cycles occurring during the 1-hour sea state, n_{1h}, given in Eq. (3.27).

$$1 - F_{X_G}(\tilde{x}_{1h}) = exp\left\{ -\frac{1}{2}\left(\frac{x}{\sigma_X}\right)^2 \right\} = \frac{1}{n_{1h}} \Rightarrow \tilde{x}_{1h} = \sigma_X \sqrt{2ln(n_{1h})} \tag{3.26}$$

$$n_{1h} = \frac{1hour}{t_{Xm02}} = \frac{3600}{t_{Xm02}} \tag{3.27}$$

3.4 Morison's formula approximation

Morison et al. (1950) found that the force exerted by unbroken surface waves on a pile extending from the seabed and through the free surface is made up of a virtual mass force and a drag force. They established the following equation for computing the horizontal force, dF, exerted on a differential section, dz:

$$dF = \rho C_M \frac{\pi D^2}{4} dz a_1 + \frac{\rho}{2} C_D D dz |u| u \tag{3.28}$$

where D is the pile diameter, ρ the water mass density, C_M the coefficient of mass and C_D the coefficient of drag. These coefficients are empirically determined based on e.g. Reynolds number, Roughness number and Keulegan-Carpenter number. u and a_1 are the undisturbed fluid velocity and acceleration at the midpoint of the section, respectively.

As discussed in section 3.2, the incident waves on a small-volume structure will not be considerably disturbed by the presence of the body. If the wavelength is large compared to the characteristic length of the structure, the hydrodynamic forces will primarily be potential flow forces in phase with the unaffected local fluid acceleration (Faltinsen (1993)).

Long waves causes small frequencies and low wave generating from the wave-body interaction, which results in negligible radiation damping contributions. For such cases, strip theory, based on Morison's formula (Eq.(3.28)), have proven sufficient to approximate the excitation forces when only linear effects are considered (Li et al. (2013), Anam et al. (2004)).

This is further justified by comparing Eq. (3.29), where the excitation force is found from Morison's equation when viscous effects and potential damping are assumed negligible, with Eq. (3.28). As Eq. (3.29) coincides with Eq. (3.28) for $C_M = 2$, the approximation based on Morison's formula is applicable if the wavelength is large compared to the characteristic length of the body.

$$dF = \underbrace{dF_{Drag}}_{=0} + dF_{Mass} = \underbrace{\rho A a_1 dz}_{dF_{FK}} + \underbrace{A_{11} a_1 dz}_{dF_D} = \rho\frac{\pi D^2}{4} a_1 dz + \underbrace{\rho\frac{\pi D^2}{4}}_{A_{11}} a_1 dz \quad (3.29)$$

Thus Faltinsen (1993) states that the force on a small-volume structure can be written according to Eq. (3.30):

$$F_{exc,k}(t) \cong \int_S p_0 n_k ds + \sum_{j=1}^{3} \bar{a}_{0j} A_{kj}, k = 1, 2, 3 \quad (3.30)$$

where p$_0$ is the pressure in the undisturbed wave field, n$_k$ the normal vector pointing inside the body, $\bar{a}_{0j}$ the wave acceleration evaluated at the geometric center of the body and A_{kj} are the added mass coefficients. The first term in Eq. (3.30) is the Froude-Kriloff force, while the second term physically represent that there is a change in the undisturbed pressure field due to the body.

For large volume structures, however, the radiation damping effects may be crucial. In such cases, potential flow theory should be utilized to analyse the hydrodynamic loads on the structure according to Eq. (3.13).

3.5 Morison's formula with the MacCamy-Fuchs correction

Karimirad (2014) state that when the diffraction forces are important and the λ/D ratio is small, Morison's formula in its basic form is invalid and diffraction theory should be utilized to predict the inertia force. MacCamy and Fuchs (1954) presented a linear analytical solution for correction of the inertia term in Morion's formula, which is to be applied together with the drag term. They found that the maximum horizontal inertia force on a bottom-fixed vertical cylinder exposed to linear waves can be described by Eq. (3.31) when diffraction forces are accounted for:

$$F_{max,horizontal} = \frac{4\rho g}{k^2}\zeta_a \frac{\sinh[k(h + \zeta_a \sin\alpha)]}{\cosh kh}\xi \quad (3.31)$$

where k is the wave number, ζ_a the linear wave amplitude and α and ξ are functions of the wave number and the cylinder radius, respectively. This diffraction theory is valid for a circular pile that is extending from the sea floor and penetrates the free surface.

Chapter 4

Numerical modelling of operation

4.1 Description of the installation system

4.1.1 Installation vessel and monopile

As stated in Sec. 1.2 there is a trend to use floating installation vessels for installation of bottom-fixed foundations. This is because they are less weather sensitive in the positioning phase and can transit more efficiently from unit to unit than the jack-ups. Nonetheless, to employ floating vessels for installation of XL monopiles is challenging because of the foundations large size and heavy weight. An installation vessel moving in waves can induce pendulum motions in the XL monopile and large forces in the lift wire, which can be critical for the safety of such an operation.

Thus to simulate a lowering operation for an XL monopile, the coupled system composed of the crane vessel and the pile substructure has to be established. In this thesis a typical monohull heavy lift vessel (HLV) is used. The main parameters of the floating installation vessel is presented in Table 4.1.

Table 4.1: Principal dimensions and main particulars for floating HLV.

Length overall [m]	Breadth [m]	Operational draught [m]	Displacement [t]
183.0	47.0	10.2	5.12E4

The crane used in the numerical model is able to perform lifts of up to 5000 t at an outreach of 32 m, in fully revolving mode, and with a maximum clear height to the main deck of the vessel of 100 m. A combination of an 8-line mooring system and a dynamic positioning system, allows the vessel to perform heavy lifting operations in shallow water and near other structures.

The XL monopile used in the simulation is equivalent to a monopile intended to support a V164-8.0MW wind turbine proposed by Kiełkiewicz et al. (2015), based on research and literature. In their study they found that in terms of weight of the structure per MW of its rated power, it would be most favourable to use an 8 m diameter pile at 25 m water depth. Since at larger depths, a 9 m pile will be more advantageous, the pile used in the numerical model has a size suitable for a 25 m water depth and a 8 MW turbine. The main dimensions for the long and hollow cylinder are presented in Table 4.2.

Table 4.2: Main parameters of the XL monopile used in the numerical model, determined from research and literature by (Kiełkiewicz et al. (2015)).

Length of pile [m]	Weight of pile [t]	Outer diameter [m]	Thickness [m]
56.0	1114.1	8.0	0.10

4.1.2 Setup for monopile lowering operation

When a HLV moves in waves, its motions will influence the responses of the monopile during lowering and the coupling effects have to be taken into account. A lift wire extends from the monopile through a guide point, defined as the crane tip, to a winch on the vessel deck.

The lift wire is assumed to be really stiff in the simulation of this operation and the wire is therefore considered to be rigidly connected to the monopile. In the numerical model the crane is also modelled as rigidly connected to the deck of the vessel. For simplicity, the lowering system is i.e. regarded as a multi-body system composed of two coupled, rigid bodies; the monopile and the vessel. The system, coupled through the lift wire, will as a result have 12 DOF when a floating installation vessel is considered.

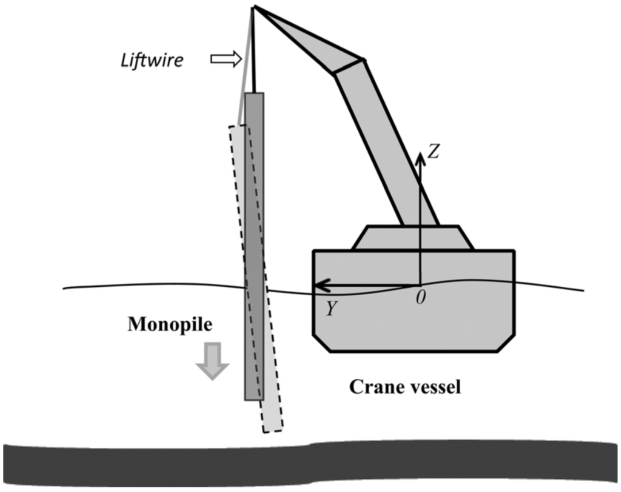

Figure 4.1: Schematic illustration of the monopile lowering system (Li et al. (2015)).

In Figure 4.1 a schematic illustration of the monopile lowering system is presented. As portrayed, the global coordinate system is a right-handed system, where the y-axis points towards the port side, the x-axis towards the bow and the z-axis upwards. The location of the origin is on the centerline and the still-water line, at the midship section, when the HLV is at rest.

With regards to the load-radius chart for the main crane in Appendix A and the design of the vessel, the position of the crane is specified in the model such that enough clearance is provided to upend and lower the monopile, while the safe working load (SWL) parameter is kept high. The crane tip and the winch is positioned at (-20 m, 30 m, 80 m) and (-74.2 m, 0 m, 10 m), respectively, with regards to the global coordinate system. In all the analyses conducted, the water depth for the installation is defined as 25 m.

4.1.3 Modelling of the couplings

When one is to perform a time-domain simulation of the lowering operation, the hydro-mechanical coupling effects arising either from hydrodynamic interaction between the two bodies or from mechanical coupling via the crane, have to be carefully examined. The mechanical coupling effects depend on the relative motions between the monopile substructure and the vessel, while the hydrodynamic couplings rely on how the presence of each body influence the hydrodynamic forces affecting the other.

Li et al. (2014) studied the hydrodynamic interaction during the lowering of a monopile substructure in detail with special focus on the shielding effects from the HLV. As shielding effects are outside of the scope of this master thesis work, only the modelling of the mechanical couplings are presented in this section.

In the numerical model the mechanical coupling via the crane, a simple wire coupling, is modelled as a linear spring according to Eq. (4.1) (MARINTEK (2009)):

$$T = k \times \Delta l \tag{4.1}$$

where T is the wire tension, k is the effective axial stiffness and Δl is the elongation. The effective axial stiffness in Eq. (4.1) is given by Eq. (4.2):

$$\frac{1}{k} = \frac{l}{EA} + \frac{1}{k_0} \tag{4.2}$$

where E, A and l is the modulus of elasticity, the cross-section area and the unstretched wire length, respectively. During the simulation the winch runs and the wire length varies. 1/k_0 is the crane flexibility, that based on Park et al. (2011) findings presented in Sec. 2.3 is given a low, constant value. According to their studies, a lifted object of the size of the monopile is too light for the crane boom elasticity to have crucial effect on the system responses. The lift wire stiffness will, on the other hand, affect the system's eigenperiods. As these have an significant effect on the system responses, the wire elasticity has to be chosen with care. With respect to the maximum capacity of the HLV, this lift can be regarded as one in the lighter range, togheter with the lift studied by Li et al. (2014), and the same lift wire properties as utilized in that case is thus used in this study. According to MARINTEK (2009), the material damping in the lift wire can be simplified as 1 % to 2 % of EA. Based on this, the damping is set to 2 % in this thesis work. The main parameters for the simple wire coupling is collected in Table 4.3.

Table 4.3: Main parameters for the simple wire coupling in the numerical model.

Lift wire		
EA/l_0 [kN/m]	k_0 [kN/m]	Damping [kNs/m]
7.0E+04	5.00E+05	1.4E+03

When a monopile substructure is installed a gripper device is usually used to constrain the motions of the pile. This device is normally made up of a circular frame surrounding the monopile and several hydraulic cylinders. During the lowering phase, the hydraulic cylinders are retracted so that a gap between the cylinders and the wall of the monopile appears. This gap is necessary to avoid critical contact forces between the stiff cylinders and the monopile surface.

Based on the fact that the gap in practise would be large enough to avoid impact during safe lowering, Li (2016) found that it would be most favourable to exclude the gripper device from the numerical model when simulating the lowering operation. Instead they suggested to use the relative motion between the two bodies as the operational criteria, since an impact always should be avoided, and judge if an impact would occur based on this motion. Thus in this thesis only the mechanical coupling of the lift wire is considered.

4.2 Numerical methods

In this Master's thesis the numerical models are established by the use of the DNV GL softwares Sesam HydroD and Sesam GeniE, in addition to the MARINTEK software SIMO.

Sesam GeniE is utilized to create a panel model of the bottomless monopile, proper for analyses conducted by Sesam HydroD. By executing the Wadam solver from Sesam HydroD, a frequency-domain hydrodynamic analysis of this structure can easily be performed. Wadam computes the wave induced forces on the panel model, with potential theory (ref. Sec. 3.1), for the specified set of wave frequencies and heading angles

(Det Norske Veritas (2010b)). For more details on the procedure ref. Sec. 5.1.

To carry out time-domain simulations for the marine operation the MARINTEK software SIMO has to be applied. This is a simulation and analysis tool used to study wave induced responses and station keeping of multibody systems.

4.2.1 Equations of motion

In Wadam, the equations of motion for a set of wave frequencies and heading angles can be solved to obtain the motion responses for the modelled monopile. The equation of motion is established for harmonic motion of rigid body systems, according to Eq. (4.3) (Det Norske Veritas (2010b)):

$$[-\omega^2(\mathbf{M}+\mathbf{A}(\omega))+i\omega(\mathbf{B}(\omega)_p+\mathbf{B}_\nu)+\mathbf{C}+\mathbf{C}_e]\mathbf{X}(\omega,\beta)=F(\omega,\beta) \tag{4.3}$$

where $\mathbf{M}$ is the inertia matrix, $\mathbf{A}(\omega)$ is the frequency dependent added mass matrix, $\mathbf{B}(\omega)_p$ is the frequency dependent potential damping matrix and $\mathbf{B}_\nu$ is the linearised viscous damping matrix. $\mathbf{C}$ and $\mathbf{C}_e$ are the hydrostatic restoring matrix and the external restoring matrix, respectively, while $\mathbf{F}(\omega,\beta)$ is the complex exciting force vector for frequency, ω, and incident wave heading angle, β.

When the added mass, damping and exciting force acting on the panel are found from Wadam, the motion vector $\mathbf{X}(\omega,\beta)$ can in theory easily be obtained by applying Newtons law as in Eq. (4.3). However, as the monopile is to be included in a coupled model where it is to be lowered towards the seabed with a lifting wire, the hydrostatic- and external restoring will have to be specified during the SIMO analyses instead. Only the hydrodynamic forces, that are later exported to SIMO, are therefore collected from Wadam.

In its calculations, Wadam assumes the flow to be ideal and time-harmonic, and for the first order potential theory the free surface condition is linearised. The exciting force transfer functions due to incident waves, are calculated by integration over all panels of the pressure resulting from the diffraction problem. Wadam determine both the radiation and diffraction potentials on the wetted body surface from the solution of an integral equation obtained by using Green's theorem (Det Norske Veritas (2010b)). Both the frequency dependent added mass and the frequency dependent damping are computed from potential theory (ref. Sec. 3.1).

In the MARINTEK software SIMO, the following equations of motion have to be solved in time-domain for the systems 12 DOF (MARINTEK (2009)):

$$\mathbf{M}\ddot{\mathbf{x}}+\mathbf{C}\dot{\mathbf{x}}+\mathbf{D_1}\dot{\mathbf{x}}+\mathbf{D_2}\mathbf{f}(\dot{\mathbf{x}})+\mathbf{K}(\mathbf{x})\mathbf{x}=\mathbf{q}(\mathbf{t},\mathbf{x},\dot{\mathbf{x}}) \tag{4.4}$$

where **x** is the position vector of the system, **M** is the frequency-dependent mass matrix, **C** is the frequency-dependent potential damping matrix, $\boldsymbol{D_1}$ is the linear damping matrix, $\boldsymbol{D_2}$ is the quadratic damping matrix, **f** is the vector function $f_i = \dot{x}_i|\dot{x}_i|$, **K** is the hydrostatic stiffness matrix and **q** is the exciting force vector given by Eq. (4.5):

$$\mathbf{q(t, x, \dot{x}) = q_{W1} + q_{WA}^{(1)} + q_{WA}^{(2)} + q_{CU} + q_{cpl}} \tag{4.5}$$

where $\boldsymbol{q_{W1}}$ is the wind drag force, $\boldsymbol{q_{WA}^{(1)}}$ is the 1. order wave excitation force, $\boldsymbol{q_{WA}^{(2)}}$ is the 2. order wave excitation force, $\boldsymbol{q_{CU}}$ is the current drag force and $\boldsymbol{q_{cpl}}$ are the coupling forces.

One of the available solution methods in SIMO is based on the retardation function, $\boldsymbol{h}$, which requires the values for the frequency-dependent potential damping and one value for the frequency-dependent added mass (MARINTEK (2009)). In this method it is assumed that Eq. (4.4) can be written as:

$$\mathbf{[m + A(\omega)]\ddot{x} + C(\omega)\dot{x} + Kx = f'(t) = q - D_2f(\dot{x}) - D_1\dot{x}} \tag{4.6}$$

By substituting $\boldsymbol{f}$(t) from Eq. (4.4) and $\boldsymbol{f}$'(t) from Eq. (4.6) the following equation, needed to be solved for the vessel's 6 DOF, is obtained:

$$\mathbf{(m + A_\infty)\ddot{x} + D_1\dot{x} + D_2f(\dot{x}) + Kx} + \int_0^t \mathbf{h(t-\tau)\dot{x}(\tau)d\tau = q(t, x, \dot{x})} \tag{4.7}$$

Here $\boldsymbol{m}$ is the body mass matrix of the vessel and $\boldsymbol{A_\infty}$ is the frequency-dependent added mass matrix at $\omega = \infty$. The hydrostatic stiffness matrix $\boldsymbol{K}$ contains the hydrostatic stiffness of the installation vessel and the restoring from the mooring lines. Li et al. (2013) simplified the mooring system for the vessel, utilized in the numerical model, as linear stiffness terms in surge, sway and yaw according to Eq. (4.8) based on the assumption that the natural periods in these DOF are equal to 90 s.

$$K_{ii} = \left(\frac{2\pi}{T_{i0}}\right)^2 \times (m_{ii} + A_{ii}), i = 1, 2, 6 \tag{4.8}$$

where T_{i0} is the natural period for the DOF, m_{ii} is the mass and A_{ii} is the potential added mass. D_1 and D_2 is the linear- and quadratic damping matrices, respectively, but for this case Li et al. (2013) found that the damping from the mooring and the viscous effects of the vessel hull can be simplified to linear damping terms. The damping terms in this numerical model are therefore determined according to DNV-OS-E310 (Det Norske Veritas (2010a)) as 10 %, 20 % and 15 % of the critical damping described in Eq. (4.9) for surge, sway and yaw respectively.

$$B_{ii} = 2\sqrt{K_{ii} \times (m_{ii} + A_{ii})}, i = 1, 2, 6 \tag{4.9}$$

where K_{ii} is the stiffness, m_{ii} the mass and A_{ii} the potential added mass.

To further simplify the study, the wind drag forces, $\boldsymbol{q_{W1}}$, the current drag forces, $\boldsymbol{q_{CU}}$ and the 2. order wave excitation forces, $\boldsymbol{q_{WA}^{(2)}}$, are excluded from the equations of motion for the vessel. These simplifications are justified based on the assumptions that the vessel responses are mainly induced by waves, not current and wind, and that the dynamic positioning system is able to control the slow-drift motions such that the second-order wave forces can be neglected from the study.

As stated above, the retardation function is calculated from the frequency-dependent added mass and damping and can therefore be expressed by Eq. (4.10):

$$\mathbf{h}(\tau) = \frac{2}{\pi}\int_0^\infty \mathbf{c}(\omega) cos\omega\tau d\omega = -\frac{2}{\pi}\int_0^\infty \omega a(\omega) sin\omega\tau d\omega \tag{4.10}$$

As the XL monopile is considered a large-volume structure, the equations of motion for its 6 DOF can be formulated as follows:

$$\mathbf{M} \cdot \ddot{\mathbf{x}} + \mathbf{Kx} + \int_0^t \mathbf{h(t-\tau)\dot{x}(\tau)d\tau} = \mathbf{F_{ext}}(t) = \mathbf{F_B} + \mathbf{F_G} + \mathbf{F_W} + \mathbf{F_{cpl}} \tag{4.11}$$

where $\boldsymbol{F_{ext}}$ are made up of the buoyancy forces, $\boldsymbol{F_B}$, the gravity forces, $\boldsymbol{F_G}$, the hydrodynamic wave forces, $\boldsymbol{F_W}$, and the coupling forces between the monopile and the floating installation vessel, $\boldsymbol{F_{cpl}}$. $\mathbf{M}$ is the mass matrix that contains the body mass matrix and the frequency-dependent added-mass matrix at infinite frequency, $\boldsymbol{A_\infty}$. $\mathbf{K}$ represents the stiffness matrix due to the restoring from the arrangement of the coupled system and the hydrostatic restoring. The retardation function, $\boldsymbol{h}$, is computed from the frequency-dependent added mass and damping of the monopile.

4.2.2 Time-domain simulations in SIMO

To find the dynamic response, time-domain simulations are performed in SIMO. The response is obtained by solving the equations of motion with Runge-Kutta numerical integration. Wave responses are included in the simulation through time series of wave responses, superpositioned harmonic components with uniformly distributed phases, pre-generated by Fast Fourier transform (FFT).

To make sure that all the resonance frequencies for the system are captured, the length of each time step has to be carefully determined. Newland (2012) states that to recognize a harmonic component with a certain frequency, at least 3 sampled values within its wave period are needed. For a time step, Δt, the shortest period that can be identified is thus 2Δt. In addition they also suggests that in order for the frequency of interest to be recognized, the Nyquist frequency should be at least twice this frequency. Based on this, the necessary time step is given by Eq. (4.12). As the target resonance frequencies, according to Table 5.8, are in the range of 0.2 rad/s to 6.2 rad/s the equations of motion are solved with a time step of 0.08 s.

$$\omega_N = \frac{2\pi}{2\Delta t} \geq 2\omega_0 \Leftrightarrow \Delta t \leq \frac{1}{2\omega_0} \tag{4.12}$$

The length of the dynamic simulation is set to 700 s for each case, except for when the RAOs are established from the harmonic waves in the regular wave analysis in Sec. 5.2.3. This ensures enough time to eliminate initial transient effects and to perform the lowering operation. During the simulation of the installation operation, further described in Chapter 6, the winch starts to run after 300 s. With a launching speed of 0.05 m/s, it uses 400 s to lower the monopile 20 m.

To avoid that the time series of wave responses, generated by FFT, repeats themselves within the 700 s time history simulated, the frequency resolution has to be less than 1/700 s. This is obtained by requesting a time series length larger than the simulation length.

The number of simulations performed for each environmental condition is chosen based on a convergence study. To account for the variability of stochastic waves and obtain an accurate basis for comparison, a sufficient number of realisations of irregular waves are needed for each condition. In order to decide on a a proper number, Simo is run for 30 different seeds and the maximum responses at steady-state are plotted against the mean value of all the 30 samples. The study is performed for the maximum liftwire tension and the maximum surge motion of the monopile, as the accuracy of these extreme responses are important if the study shall be used to establish operational limits for the installation.

A JONSWAP spectrum with a spectral peak period of T_p = 6 s and a significant wave height of H_s = 2 m is used in the study, since this sea state is frequently occurring at a typical site. The results are obtained from simulations in irregular waves, when the monopile is 20 m submerged. As illustrated in Figure 4.2 this gives an indication of how many seeds are needed to obtain convergence in the results. Based on these observations, 15 seeds are used for each of the sea states.

As discussed in Sec. 2.2, Sandvik (2012) found that the most accurate approach for estimating the dynamic responses occurring during the lowering is to repeatedly simulate the whole process for various irregular wave realisations. This method is manageable in SIMO for a monopile fulfilling the criteria of the slender body approximation, since strip theory based on Morison's formula can be utilized. As later described in Sec. 6.1, the time-variant coupled model can easily be established by specifying constant added mass- and drag coefficients for the number of strips that the monopile consists of.

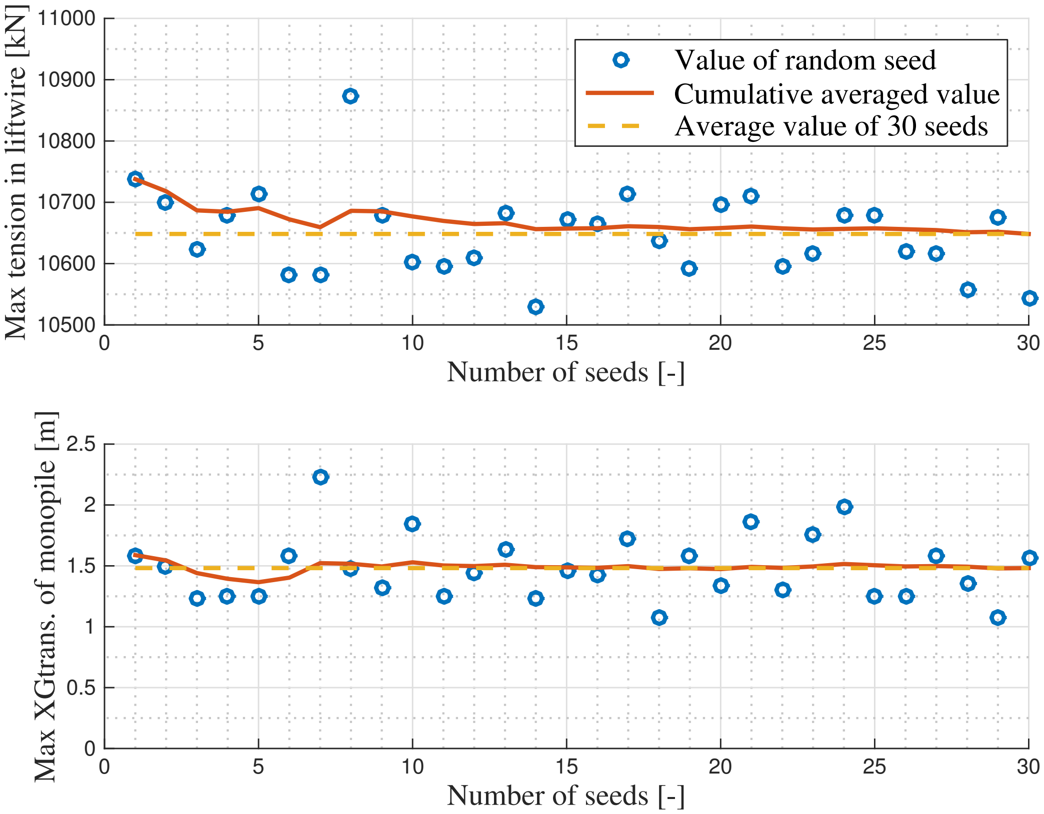

Figure 4.2: Stationary simulations are conducted in irregular waves for 30 different seeds to get an indication of how many realisations of irregular waves are needed to obtain convergence in the results (Li et al. (2013)).

However, an estimation of the hydrodynamic forces based on Morison's equation is not sufficient when diffraction and radiation effects matter. In such cases potential damping and frequency dependent added mass have to be included. As these hydrodynamic properties are obtained by solving the hydrodynamic interaction problem in the frequency-domain, using the panel method program Wadam, they are expressed by the boundary condition given on the mean body wetted surface. This makes them not applicable directly in a non-stationary process where the position of the monopile changes greatly as it is lowered towards the seabed.

A frequently used simplification for estimating the dynamic responses is such a case is thus to conduct stationary simulations for a set of irregular wave realisations with the monopile in the most onerous position and predict the extreme value based on these results instead, as described in Chapter 6.

Nonetheless, if stationary simulations are performed as here, there will be an unrealistic build-up of oscillations, according to Sandvik (2012), which will overestimate the response. This is a weakness of the utilized approach and it is thus expected that the radiation and diffraction of the monopile in reality help reduce the dynamic responses even more than what is presented in this thesis.

In this thesis the difference between the responses obtained from a regular wave analysis and an irregular wave analysis is thus investigated at steady-state conditions for a system where the monopile radiation damping effect is included (method PT). How the results differ in a steady-state and a non-stationary analysis is, on the other hand, studied by strip theory with the potential damping excluded (method ME). To study the effect of radiation damping from the monopile, both approaches for modelling is utilized and simulations are run at steady-state conditions. Table 4.4 summarizes these methods.

Table 4.4: Methods to estimate the hydrodynamic forces on the monopile (Li et al. (2015)).

Method	Morison's equation approach (ME)	Potential theory approach (PT)
Added mass	2D C_A coeff.	Potential theory A(ω)
Potential damping	0	Potential theory B(ω)
Excitation force	C_M coeff.	Potential theory F(ω)
Viscous damping	C_q coeff.	C_q coeff.

Chapter 5

Dynamic analysis at steady-state conditions

In this chapter, the extreme response for a set of monopile submergences is found by two different approaches and compared. The first predicts the responses from the system RAOs and the wave spectrum, while the other estimates them directly from time-domain simulations with various irregular wave realisations. In order to estimate the system responses from stationary analyses, the time-variant system properties first have to be established from a frequency-domain analysis in HydroD.

5.1 Frequency-domain analysis in HydroD

The frequency-domain hydrodynamic analysis based on potential theory is performed in the Sesam software HydroD. Before any runs can be commenced, however, the Wadam solver needs a panel model of the monopile as input (Det Norske Veritas (2010b)). This model is created in the Sesam software GeniE, from an input-file developed by Dr. Lin Li (ref. Li (2016)).

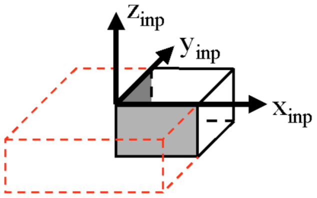

Figure 5.1: x-z and y-z plane of symmetry (Det Norske Veritas (2010b)).

When the text-file, with the modified dimensional parameters, is run in GeniE a proper panel model of a bottomless XL monopile is constructed. As the monopile is symmetric about both the x-z- and the y-z-plane, only a quarter of the pile is modelled

(Figure 5.1). After the model is built and meshed in GeniE, it is exported to HydroD. Here stationary analyses are conducted for different submergences, to obtain frequency dependent hydrodynamic properties for each draft.

To perform these analyses, a Wadamwizard is utilized to set up the proper input. As first order potential theory is applied, the models in Wadam are exposed to planar and linear harmonic incident waves described by Eq. (5.1):

$$\eta = Acos(\omega t - k(xcos\beta + ysin\beta)) \tag{5.1}$$

Since the Wadam solver in HydroD calculates the wave induced forces for a specific set of wave frequencies and heading angles, by potential theory (ref. Sec. 3.1), these have to be specified. Thus in the Wizard, a direction set of wave propagating directions, β, and a frequency set of wave periods are defined according to Table 5.1. The environmental conditions for the location are further specified through the parameters shown in Table 5.2.

Table 5.1: Direction set and frequency set for Condition1 specified in Wadam.

Direction, β [deg]	Wave period, T [s]
0, 15, 30 .. 360	3, 4, .. 40

Table 5.2: Conditions specified for location in Wadam.

Gravity [m/s^2]	Water density [kg/m^3]	Water kinematic viscosity [m^2/s]	Water depth [m]
9.81	1025.00	1.19E-06	25.00

The global response analysis is conducted for a setup composed of a hydro model and a mass model. Thus when the environmental conditions are specified, the next step is to define the hydro model, which for this case consists of a panel model that is to be imported in the next step. The characteristics that are specified for the floating hydro model is presented in Table 5.3.

Table 5.3: Characteristics defined for Hydromodel1 in Wadam.

Baseline z-position [m]	AP x-position [m]	FP x-position [m]
0	-4	4

When the proper features are assigned for the hydro model, the panel model is generated from the FEM-file exported from GeniE. Since the objective of the frequency-domain analysis is to obtain hydrodynamic properties that are later to be used to tune the coefficients for a time-variant model or for stationary analyses in SIMO, several loading conditions are defined to represent the various levels of monopile submergence. The z-position of the waterline is defined for each loading condition and a corresponding mass model is computed.

Based on the fact that only the added mass, the potential damping and the excitation forces are to be obtained from this analysis, the mass model is found by balancing with buoyancy. This basically means that HydroD sets the gravity equal to the buoyancy. Important to note is that an approach like this gives an incorrect dry mass and consequently generates useless RAOs.

Table 5.4: Overview of the input to the various analyses conducted in Wadam.

Wadamrun5	Wadamrun10	Wadamrun15	Wadamrun20
Hydromodel1 Loading5 Condition1	Hydromodel1 Loading10 Condition1	Hydromodel1 Loading15 Condition1	Hydromodel1 Loading20 Condition1

In the final step of the Wadamwizard the characteristic length is specified to be 8 m and a Wadamrun for each load case is defined according to Table 5.4. Where the same hydromodel and environmental condition are used for all the drafts, Hydromodel1 and Condition 1, respectively, but the loading condition changes.

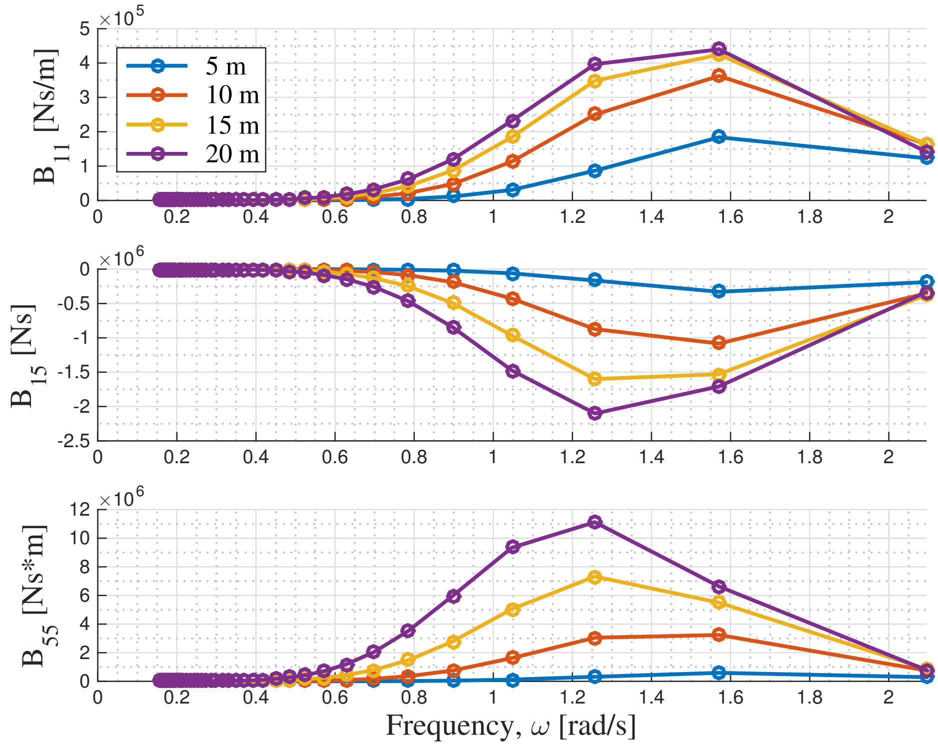

Figure 5.2: Potential damping in surge and pitch collected from stationary analyses conducted in HydroD for varying monopile submergences.

Collected from the stationary analyses conducted in HydroD, for varying drafts, is the potential damping. As initially mentioned, this hydrodynamic property is to be accounted for through the retardation function in the time-domain analysis. Due to the fact that the monopile is symmetric and that only undisturbed, head sea is considered in this study, the frequency dependent potential damping in surge and pitch is presented in Figure 5.2. In addition, the 3D added mass coefficients and the excitation force transfer functions are obtained from the frequency-domain analysis.

5.2 Steady-state analysis in SIMO

5.2.1 Time-invariant model

To obtain RAOs of typical response parameters, regular wave analyses are performed for the set of monopile submergences. The dynamic responses in the coupled system are obtained by solving the equations of motion in time-domain for the systems 12 DOF. Before the analyses are conducted, however, the installation system is modelled. Based on the system details established in Sec. 4.1 and the hydrodynamic properties obtained from Wadam, a time-invariant coupled SIMO model is developed according to the PT approach in Table 4.4.

Modelling of the installation vessel is not the scope of this Master's thesis. The model of the installation vessel and the mooring system, described in Sec. 4.1.1 and used in the simulation, are therefore provided by Dr. Lin Li. For the installation vessel, the added mass coefficients, the potential damping coefficients, the hydrostatic stiffness and the first order wave excitation force transfer functions were all computed in Wadam and provided with the model.

When a task containing this vessel is established, the XL monopile is modelled by a slender element feature in SIMO and coupled with the vessel through a lift wire as explained in Sec. 4.1.3. The monopile body is defined as a large volume structure and is assigned the mass properties shown in Table 5.5. Besides a large linear damping coefficient in yaw, to damp the irrelevant yaw-motion of the monopile, no linear or quadratic damping coefficients are specified for this body.

As stated in Sec. 4.2.2 a constant transverse quadratic drag coefficient is, however, specified for the submerged part of the monopile body in the numerical model according to Eq. (5.2) obtained from the drag-term of Morison's equation (ref. Eq. (3.28)).

$$\frac{\rho}{2} C_D D [Ns^2/m^3] \tag{5.2}$$

This coefficient is specified based on the assumption that inertia forces dominates the drag forces and a varying C_D, as a result, only has a limited effect on the result except

Table 5.5: Monopile mass matrix established in SIMO, as part of the system description file, based on input data manually specified by the author.

Mass matrix (body fixed origin)						
	(tonne)	(tonne)	(tonne)	(tonne m)	(tonne m)	(tonne m)
( )	1114	0.000	0.000	0.000	0.000	0.000
( )	0.000	1114	0.000	0.000	0.000	0.000
( )	0.000	0.000	1114	0.000	0.000	0.000
(m)	0.000	0.000	0.000	0.2998E+06	0.000	0.000
(m)	0.000	0.000	0.000	0.000	0.2998E+06	0.000
(m)	0.000	0.000	0.000	0.000	0.000	17380

for close to the eigenperiod (Li et al. (2015)). The coefficient depends on the Keulegan-Carpenter (KC) number and the Reynolds number (Rn) and is therefore assumed to be equal to 0.7, which according to Faltinsen (1993) is a reasonable coefficient for the current range. As a result the hydrodynamic data in Table 5.6 are specified for the slender body in the system description file.

Table 5.6: Part of the system description file in SIMO, concerning hydrodynamic data, established based on input data manually defined.

Hydrodynamic data		
Quadratic longitudinal drag (X-dir) - C2X	0.000	[KNs^2/m^3]
Quadratic transverse drag (Y-dir) - C2Y	2.870	[KNs^2/m^3]
Quadratic transverse drag (Z-dir) - C2Z	2.870	[KNs^2/m^3]
Linear longitudinal drag (X-dir) - C1X	0.000	[KNs/m^2]
Linear transverse drag (Y-dir) - C1Y	0.000	[KNs/m^2]
Linear transverse drag (Z-dir) - C1Z	0.000	[KNs/m^2]
Longitudinal added mass (X-dir) - AMX	0.000	[tonne/m]
Transverse added mass (Y-dir) - AMY	0.000	[tonne/m]
Transverse added mass (Z-dir) - AMZ	0.000	[tonne/m]

The additional hydrodynamic data is found in HydroD, as discussed in Sec. 5.1, and imported. As these hydrodynamic properties are obtained from a frequency-domain analysis for a given set of monopile submergences, the various properties are added to the model when it is set up with a proper configuration for that case. In other words, several time-invariant models have to be established, one for each relevant configuration with appropriate coefficients imported. The time-invariant model is therefore only utilized to perform the eigenvalue analysis of the coupled system (Sec. 5.2.2) and to conduct stationary simulations in regular and irregular waves for a given set of monopile submergences.

Table 5.7 illustrates the added mass matrix at infinite frequency utilized to solve the equations of motion, defined in the system description file for the case where the monopile is 20 m submerged, based on the imported data.

Table 5.7: Added mass matrix at infinite frequency established in SIMO, as part of the system description file, based on input data imported from Wadam for a monopile 20 m submerged.

	Added mass infinite (Made symmetric)					
	(tonne)	(tonne)	(tonne)	(tonne m)	(tonne m)	(tonne m)
(m)	1666	0.000	0.000	0.000	-1.59E+04	0.000
(m)	0.000	1666	0.000	1.59E+04	0.000	0.000
(m)	0.000	0.000	0.4702	0.000	0.000	0.000
(m)	0.000	1.59E+04	0.000	1.945E+05	0.000	0.000
(m)	-1.59E+04	0.000	0.000	0.000	1.945E+05	0.000
(m)	0.000	0.000	0.000	0.000	0.000	0.000

Now that both the mass matrix, $\boldsymbol{M}$, and the stiffness matrix, $\boldsymbol{K}$, are established for the monopile's equations of motion, only the retardation function, $\boldsymbol{h}$, and the 1. order excitation force, $\boldsymbol{F_{ext}}$ remains. From the imported frequency dependent added mass and potential damping, the retardation function discussed in Sec. 4.2.1 and defined in Eq. (4.10) can be generated in SIMO and utilized in the solution process. These retardation functions are illustrated in Figure 5.3.

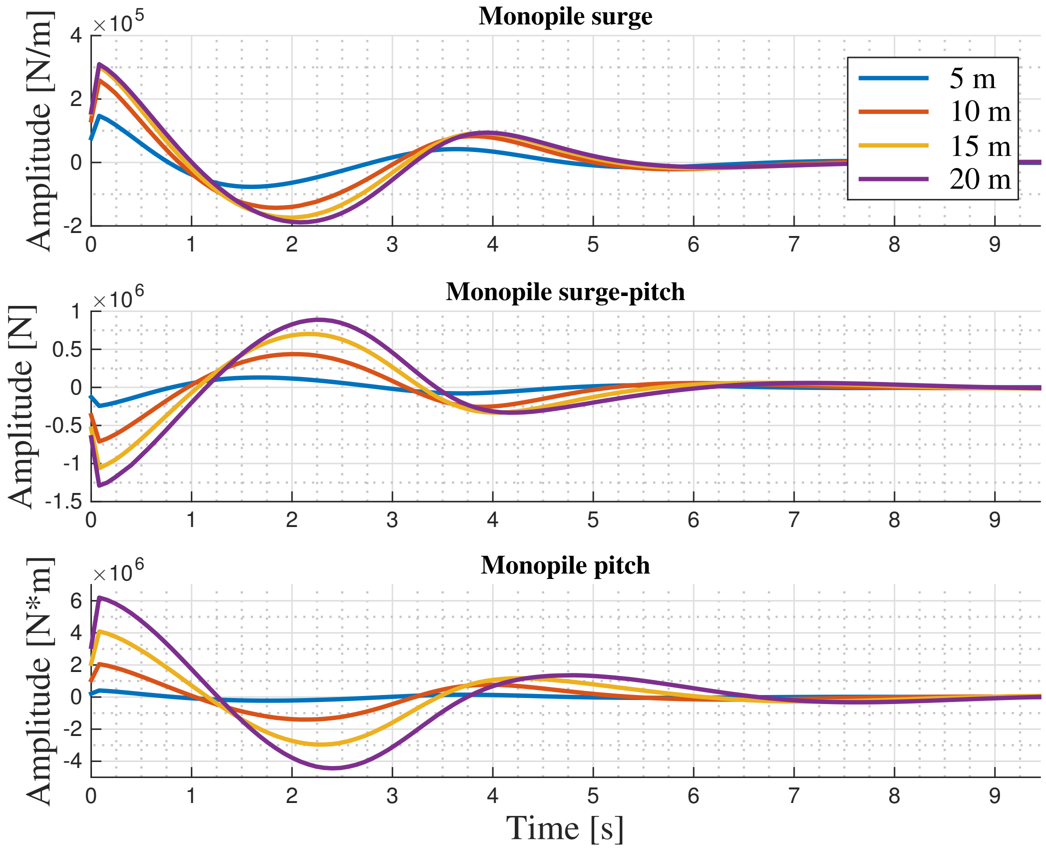

Figure 5.3: Retardation functions generated in SIMO from the frequency dependent added mass and potential damping imported from Wadam.

The 1. order wave excitation forces, found from potential theory in Wadam, is included in the numerical model in SIMO by importing the force transfer functions obtained. These transfer functions are illustrated in Figure 5.4 by the transfer functions in surge and pitch, respectively.

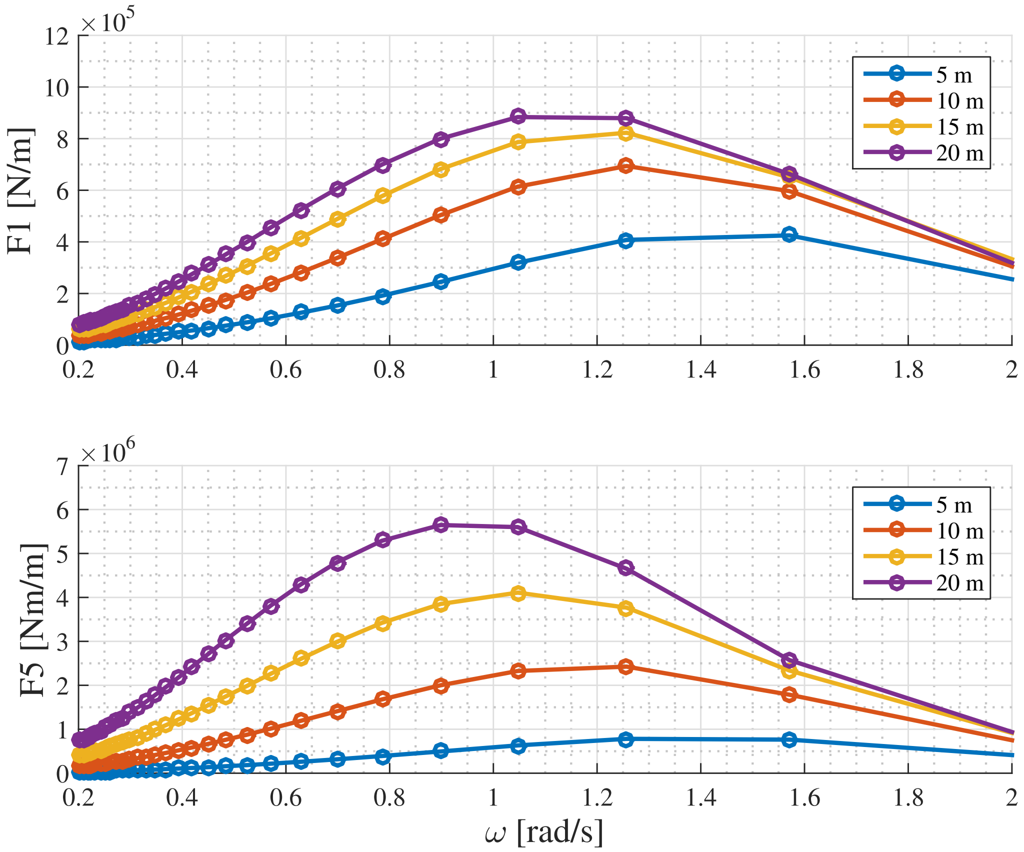

Figure 5.4: Force transfer functions obtained from potential theory in Wadam and exported to SIMO. These transfer functions give the 1. order wave excitation force effect on the monopile.

5.2.2 Eigenmodes of lifting system

The numerical model is, as stated in Sec. 4.1.2, composed of two 6 DOF rigid bodies. This means that the system will experience rigid body motion, or in other words, that the coupled motion in an arbitrary point on the body can be described by Eq. (5.3).

$$\mathbf{s} = (\eta_1 + z\eta_5 - y\eta_6)\hat{\mathbf{i}} + (\eta_2 + x\eta_6 - z\eta_4)\hat{\mathbf{j}} + (\eta_3 + y\eta_4 - x\eta_5)\hat{\mathbf{k}} \tag{5.3}$$

Before any hydrodynamic analyses are conducted in SIMO, it is thus important to assess the eigenperiods of the rigid body motions of the lifting system and understand what motion modes are governing for the lowering operation. The natural frequencies of different modes, as a function of the submergence, are obtained from Eq. (5.4) by assuming zero hydrodynamic forces on the system.

$$\big[-\omega^2(\mathbf{M}+\mathbf{A})+\mathbf{K}\big]\times\mathbf{x}=0 \tag{5.4}$$

$\mathbf{x}$ is an eigenvector that contains the 12 DOF of the coupled lifting system for the different rigid body motions. $\mathbf{M}$ is the structural mass matrix of the vessel and the monopile, $\mathbf{K}$ is the total restoring stiffness matrix and $\mathbf{A}$ is the added mass matrix. The stiffness matrix gets contributions from hydrostatic restoring, mechanical restoring and mooring restoring.

Since the frequency dependency of the hydrodynamic mass is not accounted for in the eigenvalue analysis, added mass with infinite frequency is used for both the vessel and the monopile (MARINTEK (2007)). Regarding the monopile, however, the depth dependent added mass matrices at infinite frequency have to be obtained from Wadam and imported, as discussed in Sec. 5.1.

Table 5.8: Eigenperiods and eigenvectors of coupled lifting system at 20 m monopile draft.

Body	Mode	1	2	3	4	5	6	7	8
Vessel	Heave [m]	-0.01	0.00	0.00	-0.05	**1.00**	0.00	0.00	0.00
Vessel	Roll [deg]	-0.16	-0.05	0.00	-0.05	-0.11	**-0.44**	0.14	0.00
Vessel	Pitch [deg]	-0.01	0.00	0.00	**0.33**	0.14	0.00	0.00	0.01
MP	Surge [m]	-0.01	0.00	0.14	0.06	0.01	0.01	0.06	**1.00**
MP	Sway [m]	0.00	-0.14	0.00	0.00	0.02	0.40	**0.56**	-0.08
MP	Heave [m]	**1.00**	-0.04	0.00	0.06	**0.97**	-0.39	0.13	0.00
MP	Roll [deg]	-0.03	**1.00**	-0.03	-0.19	-0.67	**-1.00**	**1.00**	-0.09
MP	Pitch [deg]	-0.06	0.03	**1.00**	**1.00**	0.39	-0.09	-0.01	**-0.89**
Natural period [s]		1.02	4.34	4.65	8.89	10.03	14.01	24.12	31.72

In Table 5.8 the governing motion modes and the corresponding natural periods for the system at a monopile draft of 20 m are presented. The eigenvectors presents the relative contribution of each mode to the natural period and can therefore be utilized to determine the natural periods of the dominating modes (MARINTEK (2007)). In this presentation the yaw-motion of the load is disregarded, as this rotation can not be controlled by the hoisting wire. Surge, sway and yaw of the installation vessel are controlled by the mooring. Based on this, these are not included in the table either, as they are viewed as secondary for this study.

Mode 1, 2 and 3 are dominated by monopile heave-, roll- and pitch motion, respectively, while the vessel is virtually not moving. The vessel is also nearly still for Mode 7 and 8, but for these modes the rotational motions are coupled with translational motions, resulting in pendulum motions with long corresponding natural periods. As illustrated in Table 5.8, Mode 7 is dominated by sway-roll motion, while Mode 8 represents the coupled surge-pitch motion.

As previously discussed, coupling effects between the floating installation vessel and the monopile arise during a lifting operation. The vessel motions affect the motions of the monopile through the lift wire, according to Eq. (5.3). In this case, (x,y,z) are the coordinates for the crane tip relative to the fixed coordinates of the vessel. These mechanical coupling effects is visible in Mode 4 to 6. In respective order, these modes are dominated by vessel pitch, heave and roll motion. Based on Table 5.8 it is therefore expected that the vessel motion will have a significant effect on the response of the monopile for wave periods close to T_P = 9 s to 14 s.

During the lowering operation, the winch runs and the wire length increases which affects the wire stiffness and consequently the mechanical restoring in the coupled system. Additionally the added mass increases due to the increasing submergence, which alters the added mass matrix. As a result, the natural periods of the rigid body modes changes with the submergence of the monopile as illustrated in Figure 5.5.

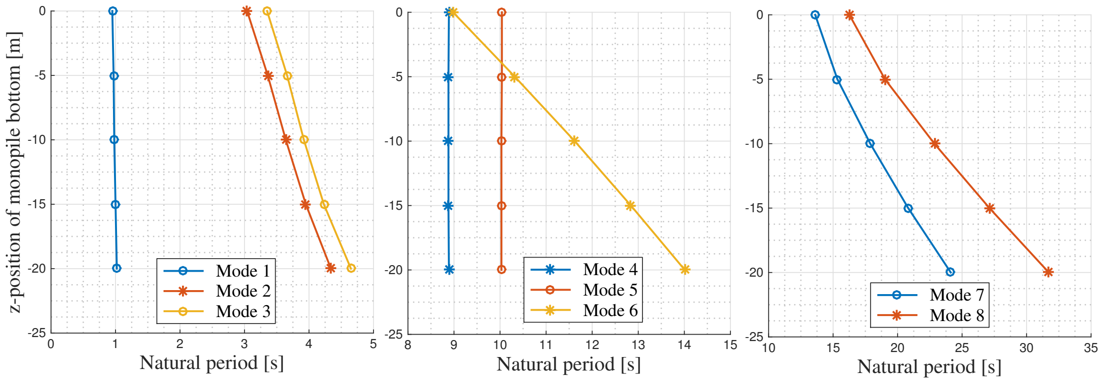

Figure 5.5: The natural periods of the rigid body modes changes with the submergence of the monopile, due to changing wire stiffness and added mass effects. Mode 1 (monopile heave) is barely affected, while Mode 2 and 3 (monopile roll and pitch) and Mode 7 and 8 (monopile pendulum motions) strongly depend on the submergence.

From Figure 5.5 it is observed that the monopile heave motion, represented by Mode 1, is barely affected by the increasing submergence. Mode 2 and 3, monopile roll and pitch respectively, are on the other hand clearly influenced by the changing monopile draft. Since a wave spectra with a spectral peak period of T_p = 4 s or T_p = 5 s will have a lot of wave power near the natural frequency in pitch for the monopile when it is 15 m to 20 m submerged, it is important to note that resonance motions might be induced by these sea states. As for the behaviour of the vessel, only the mode representing roll motion seems to be affected.

When it comes to the pendulum motions, they are strongly dependent on the submergence. They have, as illustrated, higher natural periods than the other modes. Most sea states occurring at a typical site will not have a lot of wave energy at wave periods corresponding to these frequencies and it is therefore expected that for most sea states these resonance motions will not be excited.

5.2.3 Regular wave analysis of time-invariant model

A regular wave analysis is performed in the program SIMO (MARINTEK (2007)) for each of the monopile submergences discussed so far in Chapter 5. To simplify the study, only linear wave forces and linear wave theory are considered. For each configuration, a separate SIMO task is defined and a time-invariant model is established according to the description in Sec. 5.2.1.

To investigate the response in the system to various environmental conditions, the conditions of interest have to be defined for each case. For this study, the responses induced by regular waves with a constant wave amplitude of 2 m is utilized to define the RAOs of typical response parameters. A range of different wave periods is defined for the harmonic waves by establishing a condition set. The range of wave periods included in the analysis for each task, with a somewhat higher density of wave periods around the natural periods, is illustrated in Table 5.9.

Table 5.9: Wave periods defined in a condition set for the regular wave analysis in SIMO.

Direction, β [deg]	Wave period, T [s]
0	3, 3.125, 3.25, .. 6, 6.25, 6.5, 6.75, 7, .. , 10, 11, .. 20

For each regular wave realisation a stationary simulation of 1200 s is performed. This results in time series representing the wave induced responses in the system. To avoid all transient effects, only the time series range from 800 s to 1200 s, where strict harmonic response is observed, is used to establish the RAOs. On this part of the time series, the post processor in SIMO is utilized to find the local maxima peaks and the local minima peaks, as exemplified by a wave with period T = 7 s in Figure 5.6.

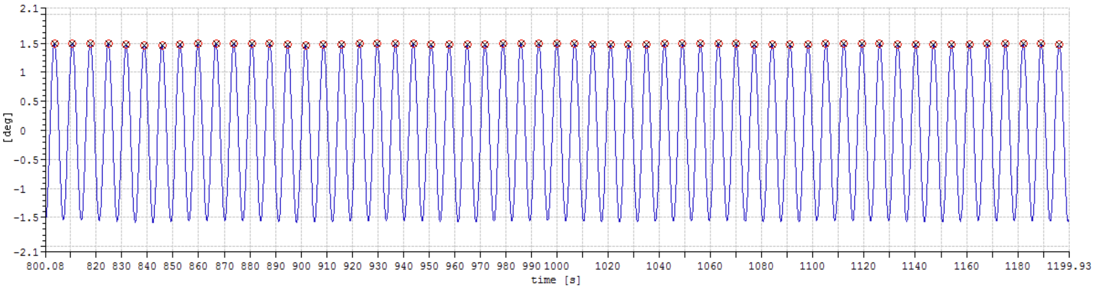

Figure 5.6: Local maxima peaks for the harmonic response of a T = 7 s and ζ_0 = 2 m wave.

From these values, the mean maxima and the mean minima is established for each of the harmonic time series. Half of the obtained response range, now defines the response amplitude, η_{j0} for the response parameter investigated. From Eq. 5.5, the RAO is established for each parameter, at each draft and for every wave period.

$$RAO(\omega) = \frac{\eta_{j0}}{\zeta_0}, j = 1, 2..6 \tag{5.5}$$

Figure 5.7 illustrates the post processor setup used to perform this regular wave analysis and obtain the RAOs. The first part portrays the different conditions containing the results from the stationary analysis conducted for each submergence. These are connected to plot-, window, peaks- and statistics functions to allow the wanted flow of data. The window-function takes care of limiting the range of the time series, the peaks-function finds the local maxima and minima, while the statistics-function computes the mean maxima and mean minima to obtain the range of the harmonic response.

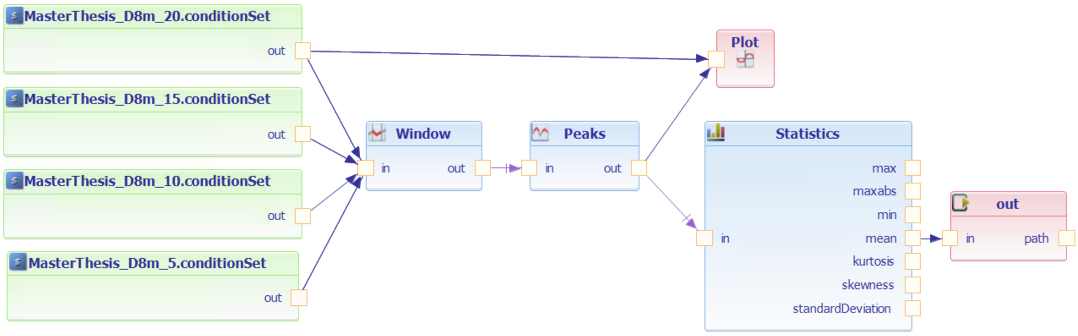

Figure 5.7: Post processor setup in SIMO for regular wave analysis.

The RAOs established from the stationary regular wave analysis are presented in Sec. 5.3.1. Based on these RAOs, the response spectra for the system motions are found for different irregular wave conditions according to Eq. (3.18). The short term wave condition is modelled by a 3-parameter JONSWAP spectrum (MARINTEK (2009)) as described in Sec. 3.1. These results are to be found in Sec. 5.3.2.

To construct the response spectra for the linear response processes, for various short term sea states, a MATLAB-script, main_response_spectrum.m, written by the author and presented in Appendix B is utilized. The script contains a function for collecting the data about the RAOs obtained from SIMO, a function which creates the wave spectrum and a function that constructs the response spectrum. To make the generating of spectra for numerous different irregular wave conditions a simple task, the script loops through a predefined set of H_s and T_p.

To estimate the short term extreme response and the standard deviation of the response process a MATLAB-script is developed. This is composed of a function that computes the variance based on the zero spectral moment and based on this value, finds the characteristic largest response value when the response process is modelled as a Gaussian process. The results of this analysis are presented in Sec. 5.3.3.

5.2.4 Irregular wave analysis of time-invariant model

To estimate the extreme responses, a second method can be utilized. This approach also obtains the responses from the time-invariant model described in Sec. 5.2.3, but in this case the responses are found directly from SIMO time-domain simulations in irregular wave conditions.

As for the regular wave analysis in Sec. 5.2.3, separate SIMO tasks are established to cover the various stationary cases investigated. For each case, linear wave theory is assumed for simplicity and steady-state coefficients corresponding to the configuration is applied by the same approach as previously discussed in Chapter 5.

The simulations for each sea state are run for 700 s, as stated in Sec. 4.2.2. This corresponds to an operation of approximately 1.5 hours, since 15 seeds are run and only the range for which the winch in theory is running is used, from 300 s to 700 s.

The irregular waves are modelled by a 3-parameter JONSWAP spectrum as discussed in Sec. 3.3.2. Time-domain simulations are performed for selected wave conditions and time series of responses are obtained. To account for the stochastic variability, the average out of the 15 time series are used to determine the response.

From these time series, the response spectra are obtained directly by using the auto spectrum-function in the SIMO post processor as illustrated in Figure 5.8. Based on conversations with Professor Zhen Gao, the default value of 3 is used for the smoothness parameter in the function since the resonant responses typically are quite narrow in the response spectra.

The results of the analysis are presented in Sec. 5.3.2. These results are also compared to the responses estimated based on the regular wave analysis.

From the response series, the standard deviation and the extreme response are also obtained. These values are found directly from SIMO, by the use of the statistics-function and the amplitude-function, and can be found in Sec. 5.3.3 where they are compared to the estimates obtained from the regular wave analysis.

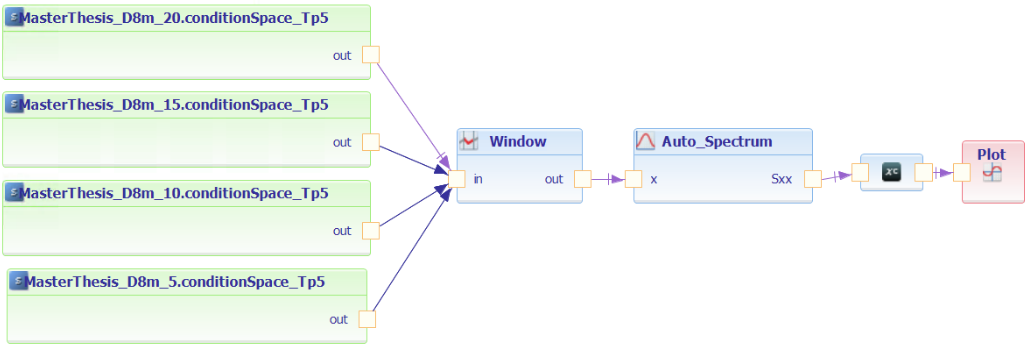

Figure 5.8: Post processor setup in SIMO for irregular wave analysis with T$_p = 5s$

5.3 Results and discussion

This section covers all the results obtained from the regular and irregular analysis of the time-invariant model. First the RAOs obtained from the regular wave analysis is presented in Sec. 5.3.1. and commented upon with regards to the eigenmodes of the coupled system. Sec. 5.3.2 provides the response spectra found from both the regular wave analysis and the irregular wave analysis and a discussion on the difference between the results obtained from the two.

In Sec. 5.3.3 the standard deviation and the extreme responses found from each analysis are presented.

5.3.1 RAOs obtained from regular wave analysis

In Figure 5.9 the resulting vessel RAOs are compared to the first order motion transfer functions, provided with the vessel model, to validate the approach utilized to obtain the RAOs. These transfer functions are part of the vessel kinetics in SIMO and decide how the vessel model is to behave in the numerical simulation. That the results from the regular wave analysis corresponds to the imported characteristics, suggest that the approach for determining the RAOs is valid.

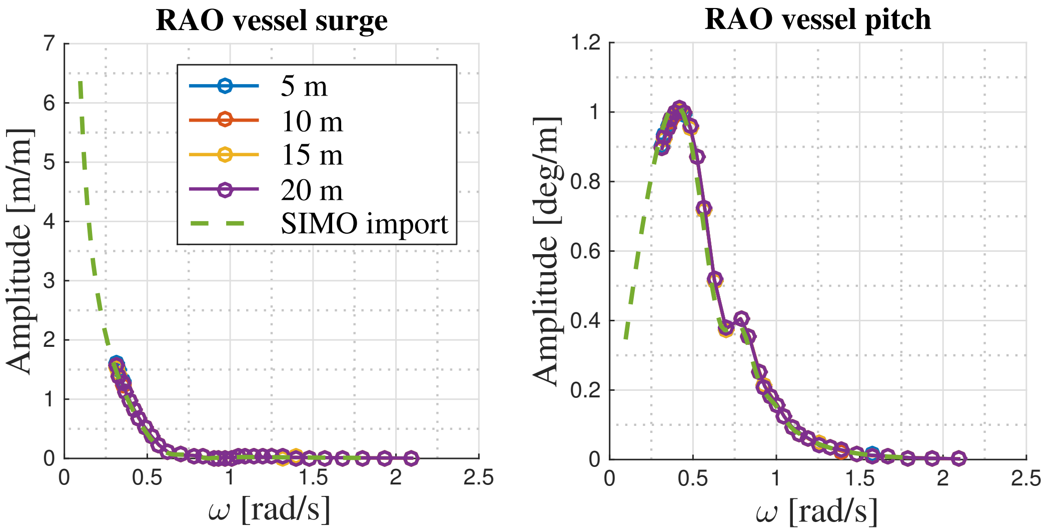

Figure 5.9: Comparison of the vessel RAOs obtained from regular wave analysis and the RAOs imported into SIMO as properties of the vessel model at head sea.

Figure 5.10 presents the vessel RAOs at head sea for surge and pitch motion obtained from the regular wave analysis conducted in Sec. 5.2.3. This figure illustrates how the RAOs for the vessel are unaffected by the lifting system configuration. The figure indicates that, whether the monopile is 5 m or 20 m submerged does not have an effect on these first order motion transfer functions.

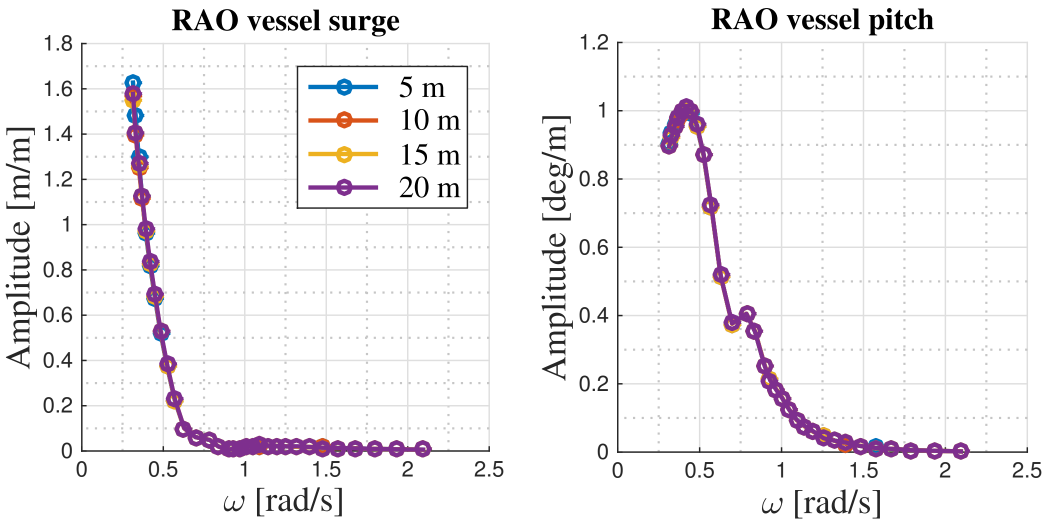

Figure 5.10: Comparison of vessel RAOs with monopile submerged to various levels.

It is observed that for T < 8 s the amplitude of the surge motion is never larger than a 10th of the wave amplitude. Waves this short do, in other words, not induce a large vessel response and the vessel is virtually not moving in surge. The same tendencies are found for the vessel pitch motion.

While for longer waves, the response in surge is steadily rising due to the long natural period in surge determined by the stiffness of the mooring. In the plot showing the pitch response, it is found that the amplitude increases at the eigenfrequency of the vessel pitch motion. For ω in the range of 0.45 rad/s to 0.7 rad/s a large induced vessel response is observed, as expected from the eigenvalue analysis performed in Sec. 5.2.2.

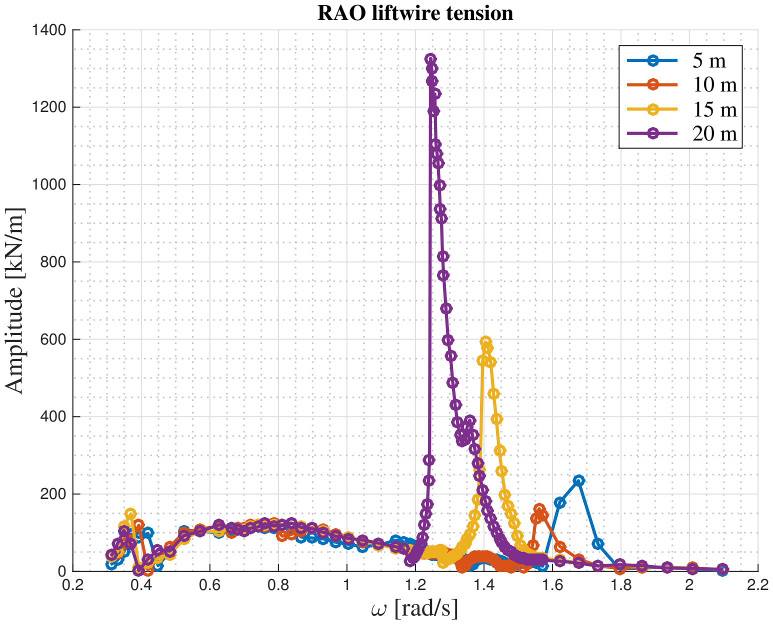

Figure 5.11: Comparison of RAOs, at different drafts, for lift wire tension at head sea.

Figure 5.11 presents the RAOs established for the tension in the lift wire. It is observed that the lift wire tension is governed by the rotational resonance motions of the monopile when the coupled system is exposed to head sea. The natural frequency of the monopile pitch motion is, as found in Sec. 5.2.2, strongly depth-dependent. It is this effect that is indicated in the figure by the draft-dependent peaks.

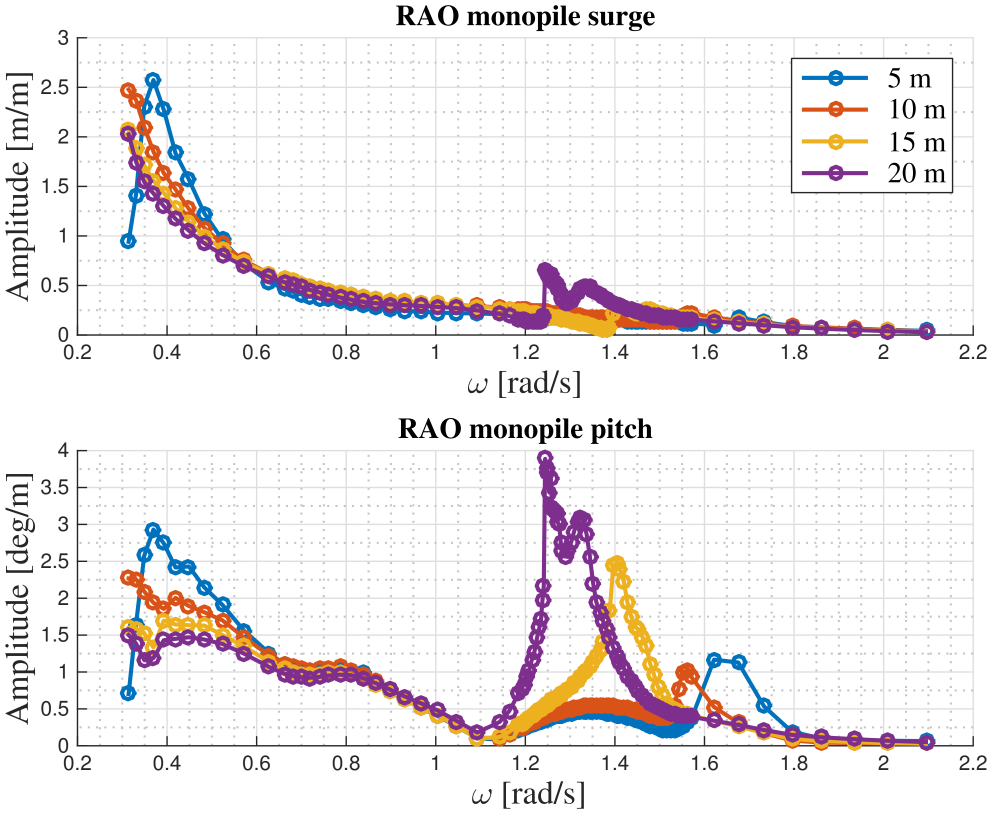

Figure 5.12: Comparison of monopile RAOs when it is submerged to various levels.

Figure 5.12 shows the RAOs of the monopile, at head sea, for surge and pitch motion. In the first sub plot, presenting the monopile surge motion, it is observed that there is virtually no response for the high wave frequencies. This is connected to the fact that the vessel is nearly still. The only exception is close to the monopile pitch natural frequency where the small contribution to the frequency from the monopile surge mode, illustrated in Table 5.8, is observed.

With regards to the lower frequencies, the affect of the pendulum motion described as Mode 8 in Sec. 5.2.2 is interesting to study. As found in that section, the submergence of the monopile has an affect on the natural frequency of the coupled surge-pitch motion. Thus it can be observed that the monopile response ratio for low frequency waves differ with only 0.5 for the various monopile drafts, up to the point where the wave frequency is in the proximity of the natural frequency. Close to this frequency, 0.35 rad/s and 0.28 rad/s for a 5 m and 10 m submerged monopile, respectively, a significantly larger difference in the response is observed.

Similar to the surge motion, the pitch response illustrated in the lower plot experiences the same coupled pendulum effects at the lowest frequencies. In this case, however, it is clear that the pitch motion of the monopile is excited for wave periods close to the natural period, as the rotational resonance motions are prominent between 1.25 rad/s and 1.68 rad/s.

5.3.2 Response spectra for monopile

The response spectra of the monopile, constructed from the RAOs obtained from the regular wave analysis and the wave spectrum, are presented in the first three figures. Regarding the spectra for the lift wire tension, the results deviates from what was expected. When the results from the two approaches are compared, this is thus further discussed.

Figure 5.14 shows the response spectrum for the monopile in irregular waves with H$_s$ = 2 m and T$_p$ = 5 s. The JONSWAP spectrum used is illustrated in Figure 5.13I. n short waves the resonant rotational motion of the monopile is excited when the frequency of the incident waves are close to the peak frequency of the wave spectrum, ω_p = 1.26 rad/s. Due to the depth-dependency of the monopile's natural frequencies, only the resonant motion of the 20 m submerged monopile is excited.

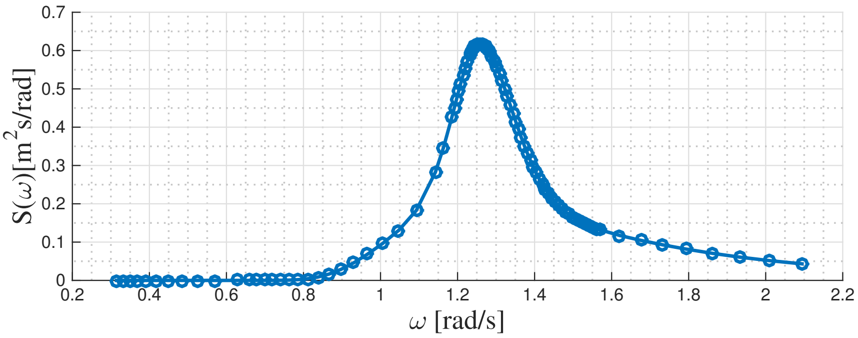

Figure 5.13: JONSWAP spectrum for H$_s$= 2 m and T$_p$ = 5 s used in regular wave analysis.

In Figure 5.16 the response spectrum for the monopile, when H$_s$ = 2 m and T$_p$ = 8 s, is given. For this sea state the resonant motion of the vessel is excited for wave frequencies near the spectral peak frequency, which induces responses in the monopile when the vessel response increases. This effect occurs as an additional peak in the response spectrum for the monopile.

The response spectrum for the monopile in irregular waves with H$_s$ = 2 m and T$_p$ = 12 s is illustrated in Figure 5.18. In long waves the system responses are dominated by the vessel motion. The only peaks found in the spectrum are thus for the wave frequencies corresponding to the energy-rich waves in the spectrum, that induces large vessel responses which consequently causes monopile motion.

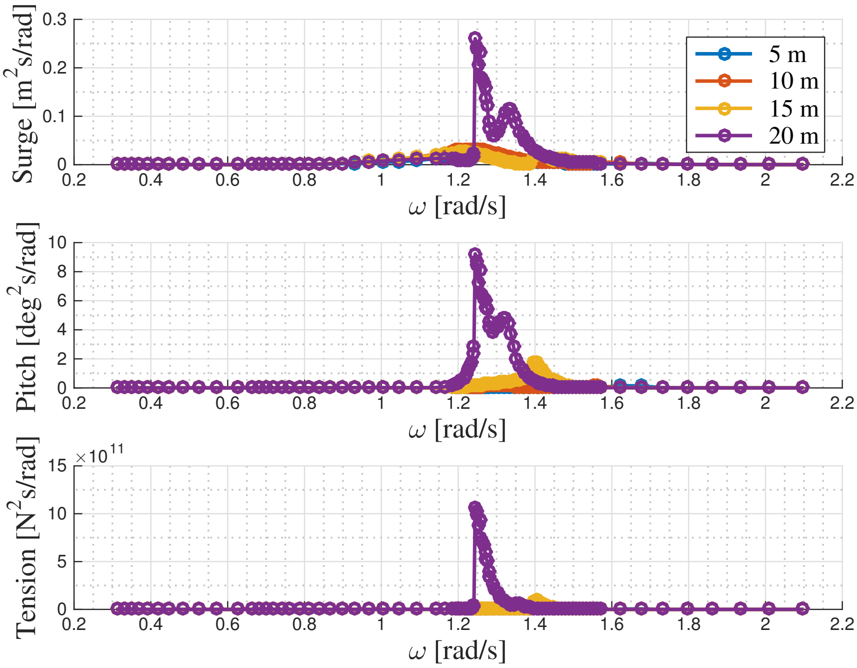

Figure 5.14: Response spectrum for monopile in irregular waves with H$_s$= 2 m and T$_p$ = 5 s.

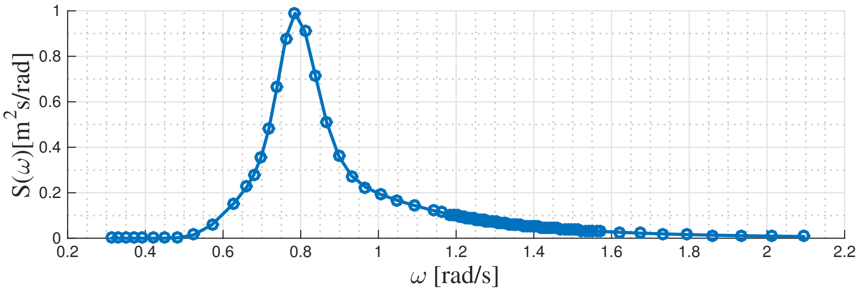

Figure 5.15: JONSWAP spectrum for H$_s$= 2 m and T$_p$ = 8 s used in regular wave analysis.

Figure 5.19 and 5.20 present the response spectra for the monopile, in short and long waves, obtained directly from time-domain analysis in irregular waves conducted in SIMO .

With regards to both short and long waves, the same effects as for the regular waves are observed to induce responses in the system. In short waves, the monopile response is governed by the pitch resonance motion at a large draft. For the same draft, 20 m, the lift wire tension has a peak frequency in the spectrum at twice the frequency of the pitch peak. This indicates that for every cycle of rotational response, a variation of two cycles is induced in the lift wire tension. The same observations was done by Li et al. (2014) which suggests that this is the physical behaviour of the system.

In the results obtained from the irregular analysis, unlike the regular analysis, the results do not indicate that the vessel response in long waves completely dominates the rotational resonance motion of the monopile. Two peaks are thus observed in the re-

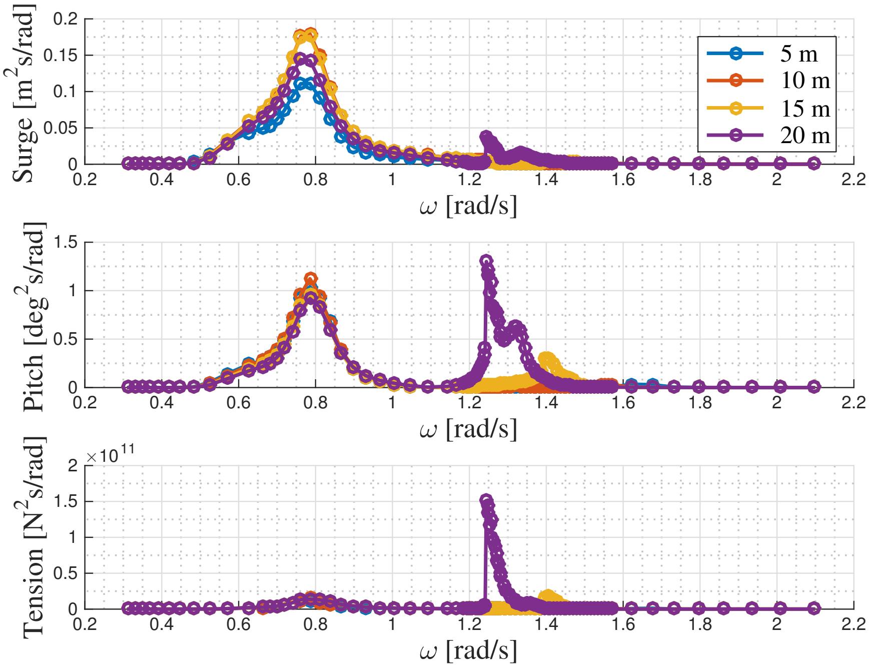

Figure 5.16: Response spectrum for monopile in irregular waves with H_s= 2 m and T_p = 8 s.

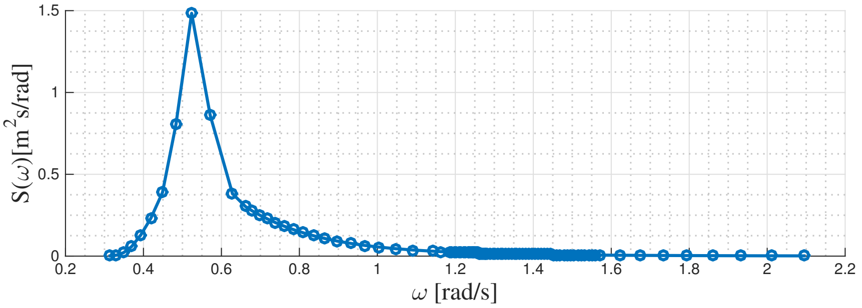

Figure 5.17: JONSWAP spectrum for H_s= 2 m and T_p = 12 s used in regular wave analysis.

sponse spectra for monopile surge and pitch in long waves. A third peak frequency is also found, but since waves with a period of approximately T = 60 s is not considered in this study, this peak is neglected during the following comparisons of the approaches.

In Figure 5.21 to 5.24 the response spectral densities obtained from the regular wave analysis and the irregular wave analysis are compared. The first two figures compare the spectra for similar monopile drafts in short waves, at T_p = 5 s, while the next two presents the results obtained in long waves, at a sea state with T_p = 12 s.

As illustrated in the figures, the response spectra obtained from the regular wave analysis deviates from the results found from the irregular analysis. This can be explained by applying the response energy as a basis for comparison. In the irregular analysis, the energy is given by the area below the response spectrum. While for the regular analysis, the energy for each regular response signal at various frequencies are given by Eq. (3.17) in Sec. 3.3.1 or i.e. half the squared wave amplitude.

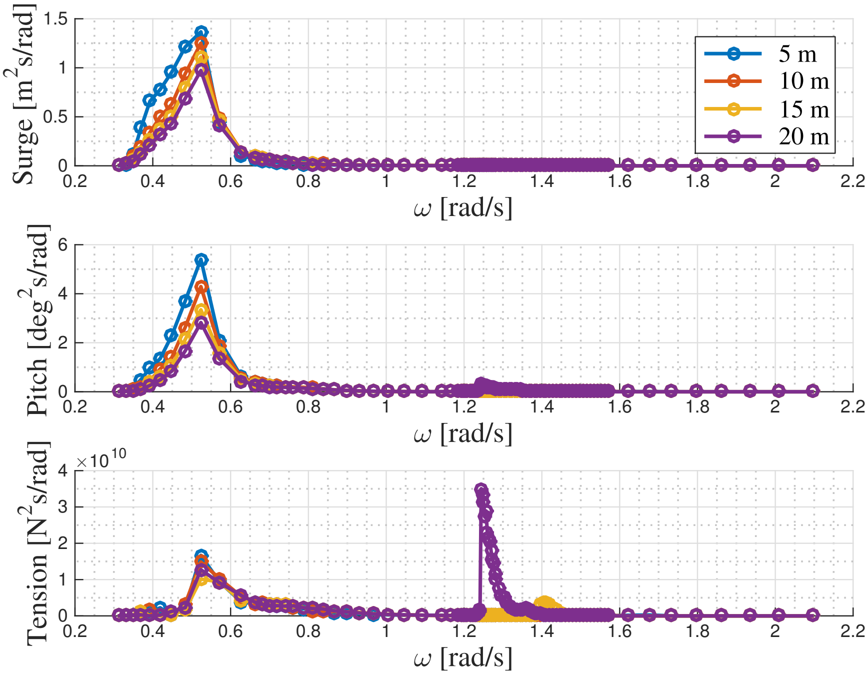

Figure 5.18: Response spectrum for monopile in irregular waves with H_s= 2 m and T_p = 12 s.

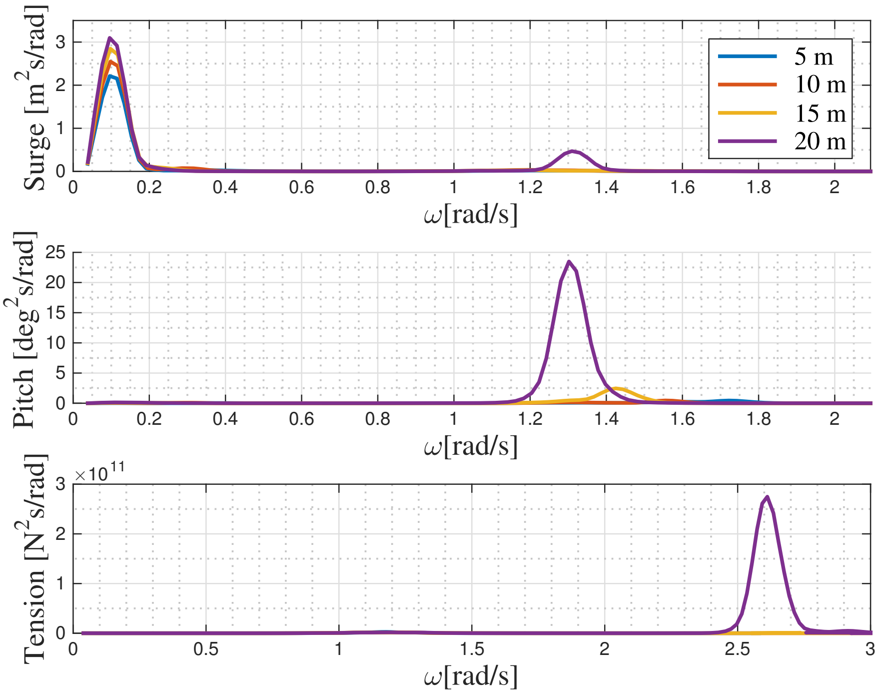

Figure 5.19: Response spectrum obtained directly from SIMO for monopile in irregular waves with H_s= 2 m and T_p = 5 s.

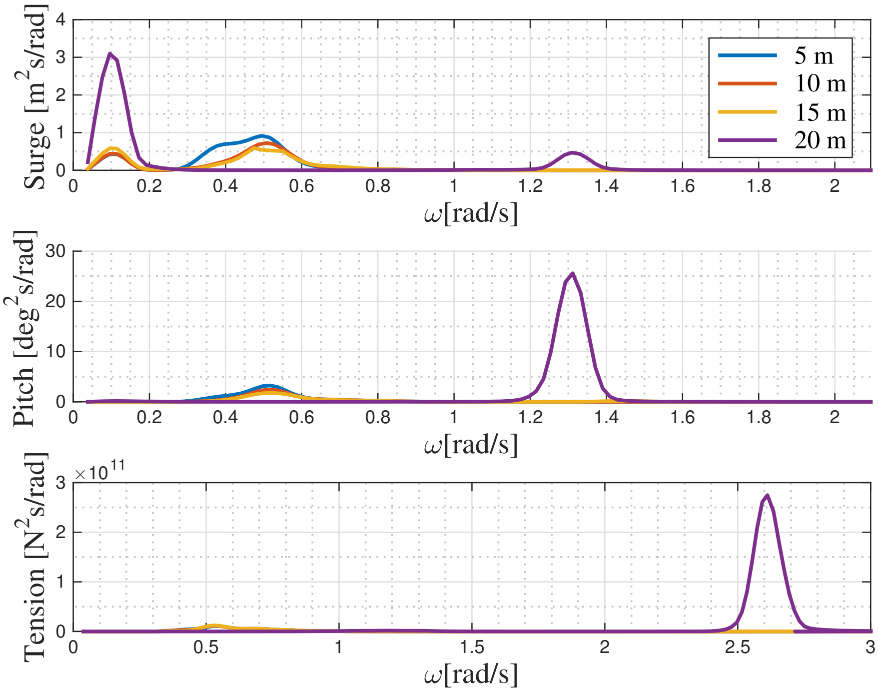

Figure 5.20: Response spectrum obtained directly from SIMO for monopile in irregular waves with H$_s$= 2 m and T$_p$ = 12 s.

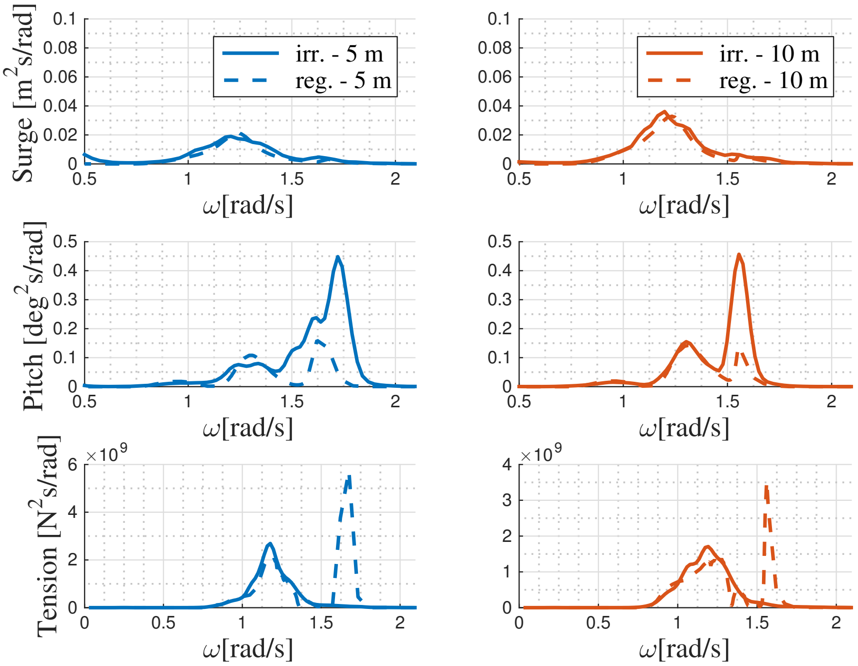

Figure 5.21: Response from regular- and irregular wave analysis with H$_s$= 2 m and T$_p$ = 5 s .

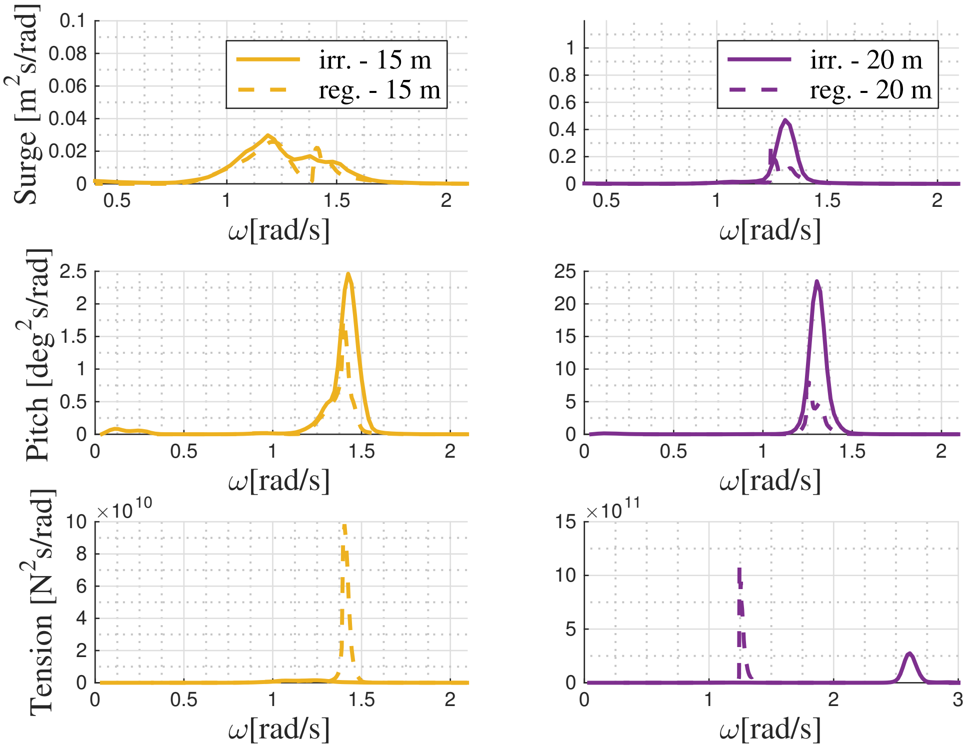

Figure 5.22: Response from regular- and irregular wave analysis with H_s= 2 m and T_p = 5 s.

Since the response might vary greatly for each regular signal, as illustrated in the RAOs obtained from the harmonic wave processes, taking the maximum value across the various frequencies investigated will generally overestimate the response. Because when the irregular waves have multiple frequencies distributed around the peak frequency, each regular wave only has a single frequency determining the response. This is the weakness of an analysis based on regular waves.

For the spectra in the figures it is most relevant to compare the response for a regular wave with a given period, to the response at the same period obtained from an irregular analysis performed for a sea state with a corresponding spectral peak period. In Figure 5.21 and 5.22 the response at the frequency corresponding to a wave period of T = 5 s is thus compared. As expected, the response from the regular wave analysis at this exact frequency, ω = 1.26 rad/s, either corresponds to or estimates a larger response than the irregular analysis. The same effect is even more apparent in Figure 5.23 and 5.24, where the response at 0.52 rad/s is investigated.

An exception to the overestimation is, however, found if the irregular wave spectral density has a peak which coincides with a resonance frequency. For such cases the frequency resolution, used to find the responses from the regular analysis in the frequency-domain, might not be sufficient to capture the exact natural frequency and the corresponding responses which are captured by the irregular wave analysis. In Figure 5.21 and 5.22 the peaks in the response spectral density from the irregular analysis clearly corresponds to the depth-dependent natural frequency in pitch.

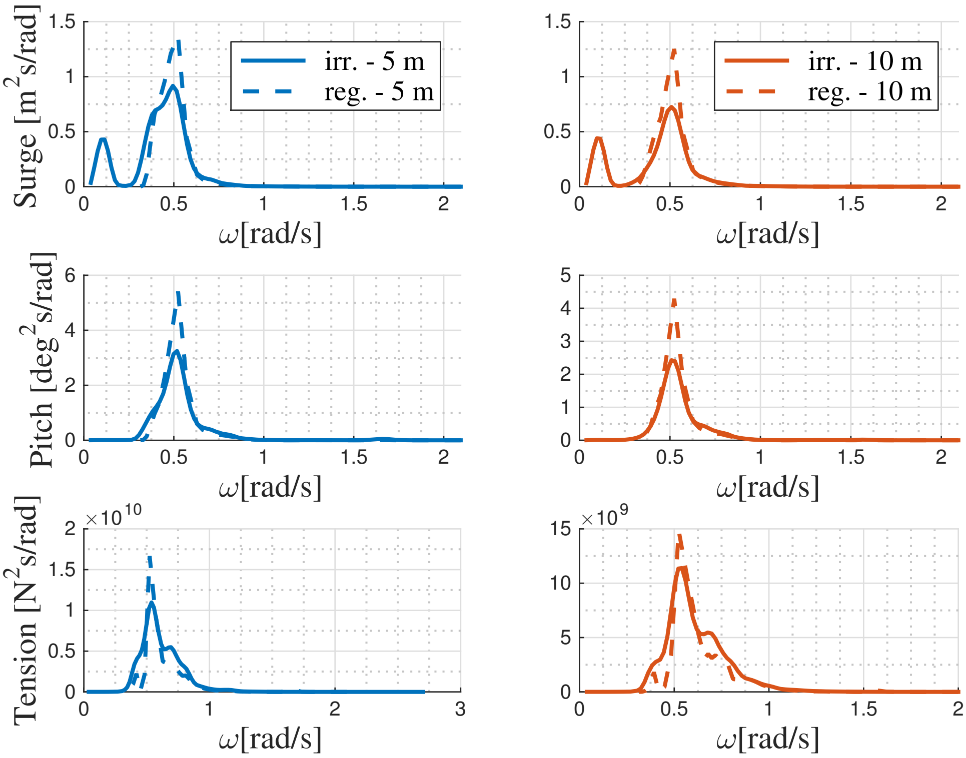

Figure 5.23: Response from regular- and irregular wave analysis with H$_s$= 2 m and T$_p$ = 12 s
.

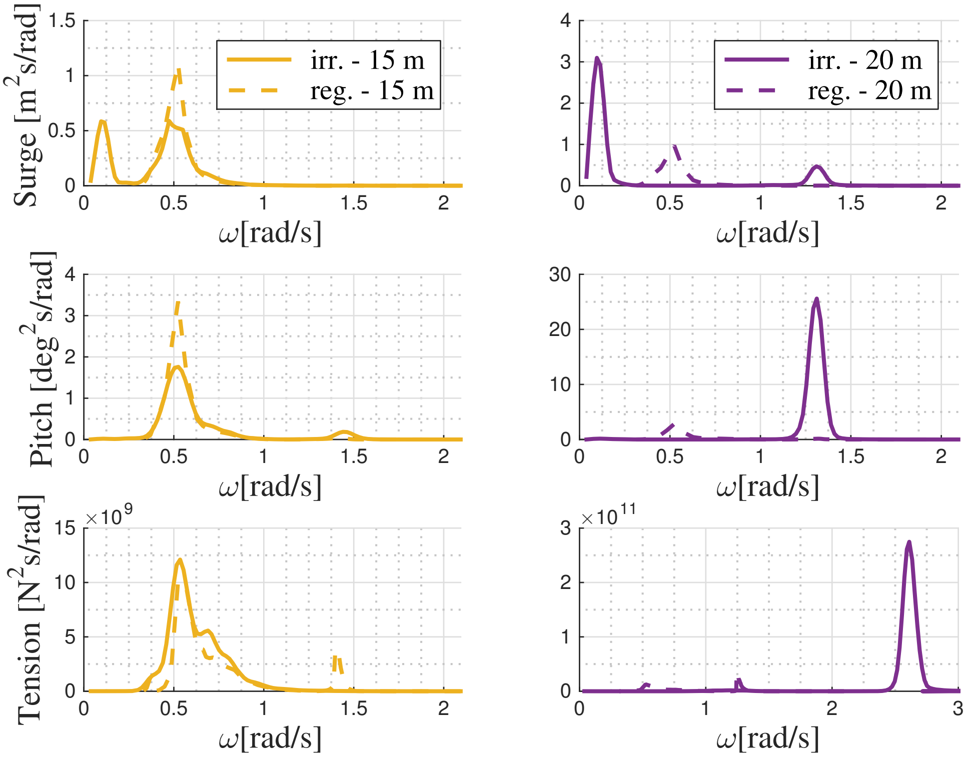

Figure 5.24: Response from regular- and irregular wave analysis with H$_s$= 2 m and T$_p$ = 12 s
.

5.3.3 Standard deviation and short-term extreme

Figure 5.25 shows the short-term extreme responses and the standard deviations found in surge from the regular and the irregular wave analysis. This figure indicates that all the values obtained from the irregular analysis are larger than the ones obtained from the irregular. A result like this, deviates significantly from the expectations established based on the discussion in Sec. 5.3.2. A reason for the large responses might be the extra peak observed at a wave period of approximately 60 s in the response spectra given in Figure 5.19 and 5.20. These results should therefore be further verified.

The results in Figure 5.26 do correspond with the expectations. In this case, the irregular wave results at T_p = 5 s is the largest, due to the fact that the natural frequency of the motion is close to T_p as expected. While at T_p = 12 s the response is smaller for every case, except for at a 20 m draft. This response should be further verified, as previous results indicate that there might be an error in the simulation for this case.

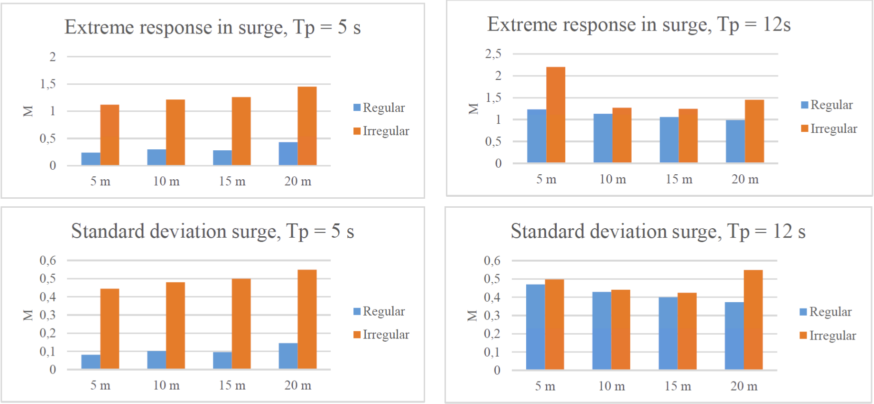

Figure 5.25: Extreme response and standard deviation in surge at H_s = 2 m and T_p = 5 s and T_p = 12 s from regular and irregular wave analysis.

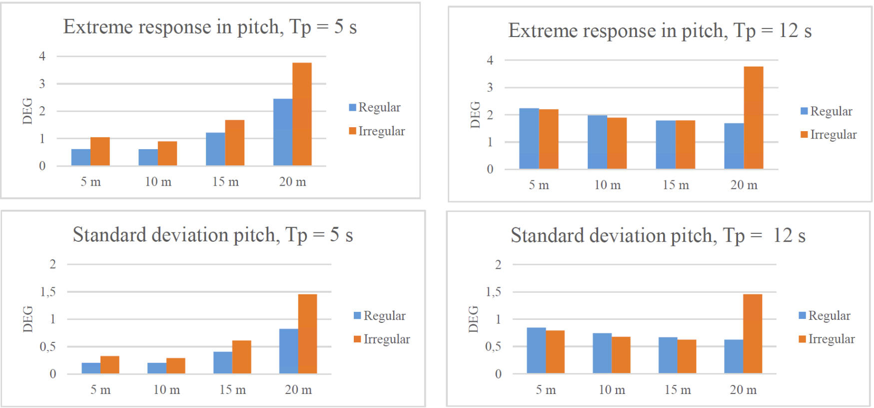

Figure 5.26: Extreme response and standard deviation in pitch at H_s = 2 m and T_p = 5 s and T_p = 12 s from regular and irregular wave analysis.

Chapter 6

Numerical simulation of lowering

To approximate the hydrodynamic forces for the lowering process, Morison's formula can be utilized. In Morison's formula approximation, however, the diffraction and the radiation of the structure are neglected. These effects thus have to be described by system properties obtained from potential theory. The issue is that these hydrodynamic properties cannot be applied in a non-stationary case, as previously discussed, since they are obtained by solving the wave-body interaction problem in the frequency domain.

In this chapter, the effect of neglecting the radiation damping of the XL monopile is therefore studied in Sec. 6.1.2. This is investigated through time-domain analyses of the monopile when these effects are both included and excluded. Additionally, the responses obtained from a stationary simulation in the most onerous position is compared to the results obtained from a non-stationary analysis in Sec. 6.1.3. A time-variant model, where the responses are estimated from strip-theory, are utilized to examine the significance of conducting simulations of the complete lowering. However, to apply this approach a study of the time-variant system properties are required to obtain proper coefficients.

6.1 Time-domain analysis of time-variant model

6.1.1 Time-variant model

To use strip theory to account for the added mass and the quadratic drag, constant coefficients have to be obtained for the various strips. The added mass coefficients are also used to compute the excitation force in Eq. (6.1) and it is thus crucial for the accuracy of the result to find proper depth dependent coefficients.

To account for the horizontal motion, η_1, of a circular cylinder, Morison's formula in Eq. (3.28) can be modified to the following (Faltinsen (1993)):

$$dF = \rho C_M \frac{\pi D^2}{4} dz a_1 - \rho C_A \frac{\pi D^2}{4} dz \ddot{\eta}_1 + \frac{\rho}{2} C_D D dz (u - \dot{\eta}_1)|u - \dot{\eta}_1| \tag{6.1}$$

where ρ is the water mass density, D is the diameter of the cylinder, u and a_1 are the horizontal undisturbed fluid velocity and acceleration at the midpoint of the strip, respectively, $\dot{\eta}_1$ and $\ddot{\eta}_1$ are the velocity and acceleration at the midpoint of the strip due to body motion, C_M the mass coefficient, C_A the added mass coefficient and C_D the quadratic drag coefficient. Eq. (6.1) gives the horizontal force, dF, on a strip of length dz. The first term is the one which describes the wave excitation forces discussed in Sec. 3.2, the second is the inertial term and the last is the drag term.

As for the time-invariant model, the quadratic transverse drag coefficient, constant over each strip, is defined in the numerical model in SIMO according to Eq. 5.2.

The added mass coefficients are, on the other hand, obtained from a study, illustrated in Figure 6.1, of non-dimensional 2D added mass values. These values are found from the 3D added masses at fixed drafts, retrieved by the panel method in HydroD, during the project work of the author. This figure only gives an indication on proper values for the coefficients. A further sensitivity study is conducted with regards to Figure 6.2.

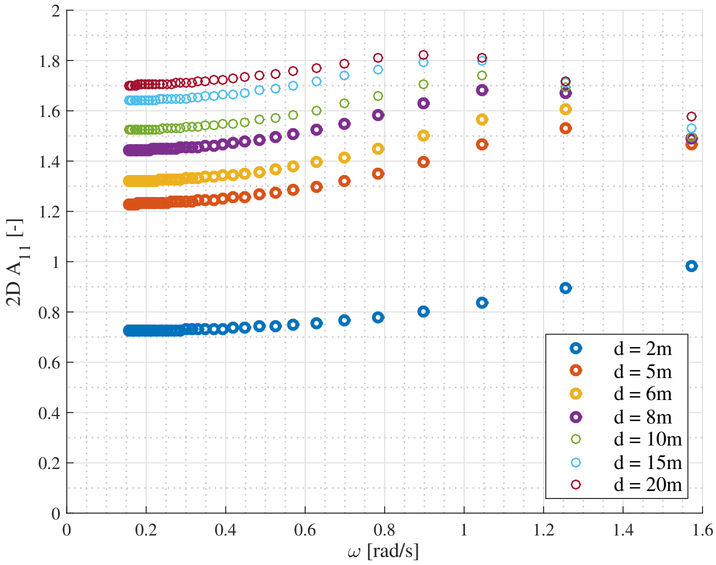

Figure 6.1: Frequency dependent, non-dimensional 2D added mass, for various submerged lengths of the XL monopile.

The fact that the monopile is bottomless and gets water-filled when submerged, is the reason why 2D added mass coefficients change with the draft. When there is water with free surface inside the cylinder, the hydrodynamic coefficients get affected (Li et al. (2013)). Mavrakos (1988) studied the fluid motion inside a bottomless cylidrical body floating in water and found that the wall thickness also influence the hydrodynamic properties.

At really small drafts it is observed that the 2D added mass coefficient is close to 1, which corresponds to the coefficient for the pile extending from the seabed through the free surface, or in other words an empty cylinder. While for drafts larger than 5 m, the coefficient increases.

That the value approaches a constant about twice as large as the coefficient for the closed cylinder seems reasonable. This is concluded based on the fact that the bottomless monopile will get an extra contribution to the added mass from the water inside the cylinder. These findings are supported by Li et al. (2013), whom states that the water filled in the pile will behave as 'frozen water'. Thus in the numerical model the following dimensionless 2D coefficients are utilized to define the added mass of the monopile by strip theory:

$$C_A = \begin{cases} 1.00, & \Delta z < 2 \text{ m} \\ 1.60, & 2 \text{ m} \leq \Delta z < 5 \text{ m} \\ 2.00, & 5 \text{ m} \leq \Delta z \end{cases} \tag{6.2}$$

where each strip is considered as 1 m and Δz is the distance from the bottom of the monopile to the considered strip. Based on Eq. (6.2), transverse added mass coefficients are defined in the numerical model according to the expression in Eq. (6.3) such that the added mass of each strip adds up to the 3D added mass in surge of the complete submerged structure. The added mass computed based on the transverse added mass coefficients are only taken into account when the strips are submerged.

$$\rho_W C_A \frac{\pi D^2}{4} [kg/m] \tag{6.3}$$

To investigate the quality of these 2D added mass coefficients, the 3D added mass at different monopile submergences is recalculated based on these coefficients (ME), according to Eq. (6.4) to (6.6):

$$A_{11}^{3D} = \int_{-d}^{0} A_{11}^{2D}(z)dz \tag{6.4}$$

$$A_{15}^{3D} = \int_{-d}^{0} z \times A_{11}^{2D}(z)dz \tag{6.5}$$

$$A_{55}^{3D} = \int_{-d}^{0} z^2 \times A_{11}^{2D}(z)dz \tag{6.6}$$

where d is the submerged length, A_{11}^{2D} the 2D added mass in surge and dz a differential section.

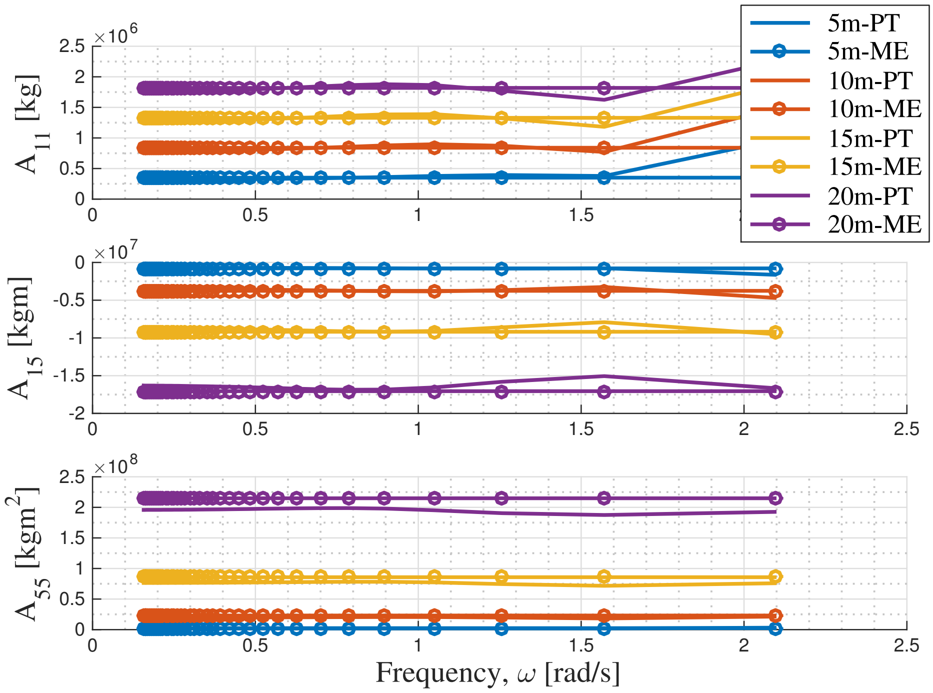

Figure 6.2: Added mass for the monopile at different drafts computed by Potential theory (PT) and Morison's equation (ME).

In Figure 6.2 these values are compared to the 3D added mass obtained directly in HydroD from Potential theory (PT). Based on this figure, the choice of 2D added mass coefficients seems reasonable. For wave conditions with low frequencies, the regime for which Morison's formula approximation has proven sufficient, the added masses computed based on the two different theories correspond quite well. For application in Morion's formula, the added mass coefficients found in Eq. (6.2) are therefore used.

This is further justified in Figure 6.3, where the excitation forces obtained from Potential theory by the Wadam solver in HydroD are compared to the excitation forces computed by Morison's formula based on the obtained added mass coefficients in Eq. (6.2). In the ME approach the excitation force is found according to Eq. (6.7) - (6.8):

$$F_1 = \int_{-d}^{0} dF_1(z)dz = \int_{-d}^{0} C_M \rho A \omega^2 \zeta_a e^{kz} cos(\omega t) dz \tag{6.7}$$

$$F_5 = \int_{-d}^{0} z \times dF_1(z)dz = \int_{-d}^{0} C_M \rho A \omega^2 \zeta_a z e^{kz} cos(\omega t) dz \tag{6.8}$$

where the amplitude of the forces are $F_1 = C_M \rho A g \zeta_a (1 - e^{-kd})$ and $F_5 = C_M \rho A \frac{g}{k} \zeta_a (1 - e^{-kd})(kz + 1)$, and the mass coefficient $C_M = C_A + 1$ is taken as $C_M = C_A$ since the diffraction part of the excitation force is assumed to have negligible effect.

Figure 6.3 illustrates how the excitation forces obtained by strip theory and Morison's equation corresponds well to the forces retrieved by the panel method, where diffraction and radiation are taken care of, for frequencies below approximately 1 rad/s. For higher frequencies, the figure indicates that an approximation based on Morison's formula is not sufficient to catch all the important effects.

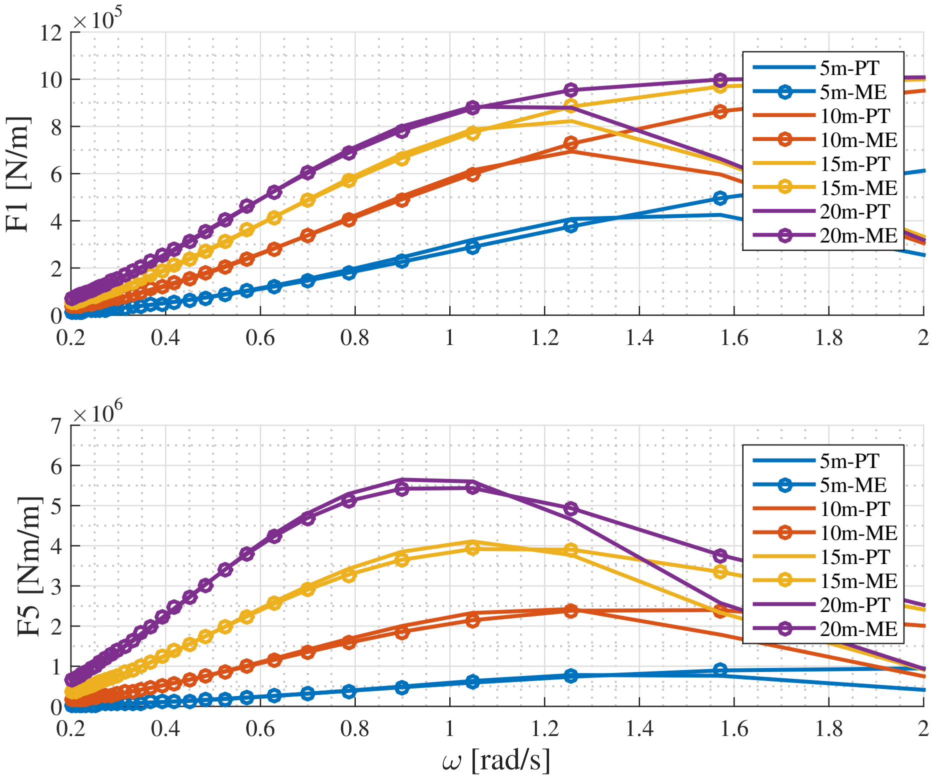

Figure 6.3: Excitation forces obtained from potential flow theory 'PT' compared to the forces obtained from 'ME'.

6.1.2 Study of monopile radiation damping effect

In this section, the approach utilized to investigate the effect of monopile radiation damping is described. To investigate the significance of including potential damping in the numerical simulation of an XL monopile, time-domain simulations are performed at steady-state conditions for the two models previously discussed.

The time-invariant model, described in Sec. 5.2.1, takes due to its time-variant system properties the radiation of the monopile into account. This is not the case for the time-variant model established in Sec. 6.1.1, which neglects diffraction and radiation effects to be able to engage in non-stationary analyses. As the aim during the numerical modelling was to portray the same coupled system, the models should behave approximately identical if the effect of this single characteristic is negligible. The difference in the response spectral density obtained from each model at similar conditions will thus indicate how the potential damping affects the results.

Even if the hydrodynamic coefficients were carefully determined in Sec. 6.1.1, the system behaviour for the two models does not correspond. From an eigenvalue analysis of the time-variant model, it is found that the natural periods differ from the ones presented in Table 5.8 in Sec. 5.2.2. As briefly discussed in Sec. 6.2.1, this affects the responses and disrupt the basis for comparison.

Since the difference in the eigenfrequencies indicates that the Morison model is modelled too flexible compared to the time-invariant model, some modifications are performed to obtain a starting point that will help emphasize the effect examined in this section. A sensitivity study is therefore conducted for the wire stiffness in the time-variant model and the lift wire properties are changed to the ones presented in Table 6.1.

Table 6.1: Modified parameters for the simple wire coupling in the time-variant model.

Lift wire		
EA/l_0 [kN/m]	k_0 [kN/m]	Damping [kNs/m]
7.0E+05	5.00E+05	1.4E+03

On the basis that only the pitch, the surge and the coupled pitch-surge motion are studied in this thesis, the wire stiffness is increased to a level where the natural periods for Mode 3, 4 and 5 corresponds better with the periods in the time-invariant model. How the increasing stiffness affects the remaining modes is disregarded at this point. The effect of this is further discussed in Sec. 6.2.1.

This change drastically alters the model's eigenperiods and eigenmodes, as illustrated in Table 6.2. The eigenperiods for the time-invariant model are given in Table 6.3 for comparison.

Table 6.2: Eigenperiods and eigenvectors for Morison model at 20 m monopile draft.

Body	Mode	1	2	3	4	5	6	7	8
Vessel	Heave [m]	-0.01	0.00	0.00	0.25	0.03	0.00	0.00	0.00
Vessel	Roll [deg]	-0.19	-0.09	0.00	0.04	-0.04	**0.28**	0.02	0.00
Vessel	Pitch [deg]	-0.01	0.00	-0.02	-0.14	0.14	0.01	0.02	0.02
MP	Surge [m]	-0.01	0.02	0.21	-0.14	0.13	0.02	0.15	**1.00**
MP	Sway [m]	0.00	-0.22	0.01	-0.02	0.02	-0.24	**0.77**	-0.14
MP	Heave [m]	**1.00**	-0.09	0.00	0.22	0.07	0.29	0.04	0.00
MP	Roll [deg]	-0.03	**1.00**	-0.07	0.29	-0.40	**1.00**	**1.00**	-0.16
MP	Pitch [deg]	-0.05	0.09	**1.00**	**-1.00**	**1.00**	0.15	0.06	**-0.82**
Natural period [s]		0.50	3.47	4.64	9.96	10.37	3.62	37.2	44.32

Table 6.3: Eigenperiods previously obtained for time-invariant model at 20 m monopile draft.

Natural period [s]	1.02	4.34	4.65	8.89	10.03	14.01	24.12	31.72

The draft of the monopile is defined as 20 m for both models and analyses are run for two different irregular sea states, T_p = 5 s and T_p = 12 s, respectively. From the 15 time series resulting from each case, the response spectra are obtained from the SIMO post processor in the same way as previously discussed and illustrated in Sec. 5.2.4. The only exception is the larger smoothness parameter, which in this case is equal to 15. Spectra from the same sea states are then compared to illustrate how the potential damping affects the responses. This comparison is presented and discussed in Sec. 6.2.1.

6.1.3 Response analysis of non-stationary lowering

In this section the significance of performing complete non-stationary simulations of the lowering operation is investigated. As one of the most utilized simplification of the nonstationary lowering process is to locate the most critical position of the lowered object and conduct steady-state analyses for various irregular sea states at that spot, it is interesting to study the effect of this simplification.

Two approaches, both based on the Morison model and proposed by Sandvik (2012), is used to obtain the extreme responses in the coupled system. In the first approach, a slow lowering is conducted in harmonic waves for each of the regular waves presented in Table 6.4, to identify the most onerous position for the monopile. This lowering is performed at a winch speed of 0.01 m/s. To make sure that the most critical position is identified, the amplitude of the harmonic waves have to be large enough to induce realistic slamming forces. Based on Sandvik (2012), an amplitude of 2.5 m is thus chosen.

Table 6.4: Wave periods used in simulation of slow lowering to identify critical position.

Wave amplitude, ζ_0 [m]	Wave period, T [s]
2.5	4, 5, 6, .. 20

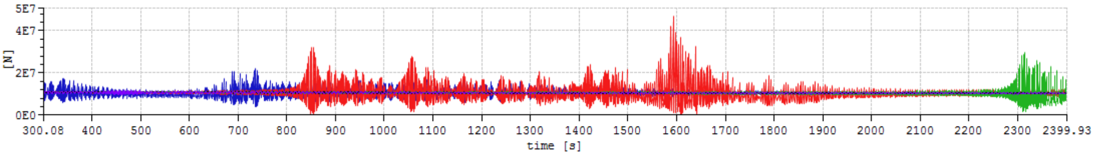

Figure 6.4: Response during slow lowering, in various color coded, harmonic waves.

Figure 6.4 illustrates a representative selection of the time series of responses obtained from this study. This figure indicates that the most critical position for the monopile can be found after 1600 s. As the winch starts to run at 300 s, the monopile has been lowered 13 m by this time. When the most intolerable position is determined, stationary simulations are conducted in irregular waves with the monopile in this position. The analysis is performed for the sea states presented in Table 6.5.

Table 6.5: Sea states used in study of lift wire tension maximum range.

H_s [m]	T_p [s]
2	5, 6, 7, .. 12

From these analyses, the maximum range of the lift wire tension from each sea state is obtained and plotted as shown in Figure 6.5. This study indicates that the most critical lift wire tension occurs for H_s = 2 m and T_p = 5 s. In Sec. 5.3.1 it was found that the lift wire tension is governed by the rotational resonance motions of the monopile when the system is exposed to head sea, which corresponds well with these observations.

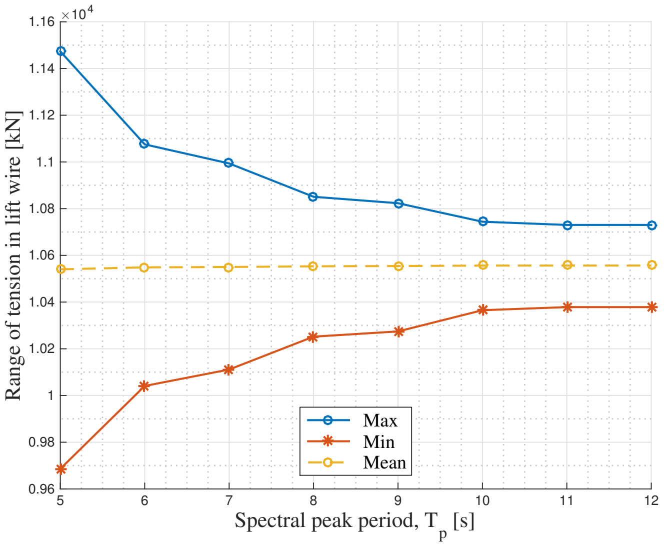

Figure 6.5: Maximum tension range at various sea states with monopile in onerous position.

When both the most intolerable position and the most critical sea state is identified, stationary simulations are conducted for 15 realisations of irregular waves. From the resulting response series for the lift wire tension, the distribution of the global maxima and minima is studied. Since the response process can be modelled as a Gaussian stochastic process, as discussed in Sec. 3.3.3, the global peaks are assumed to be Rayleigh distributed.

By utilizing the post processor in SIMO, the short-term extreme responses can now be estimated from the statistical distribution. These extreme responses are in the current approach assumed to be representative for the motion during the deployment of the monopile. If the probability of non-exceedence is set equal to 1 over the number of zero-up-crossing response cycles occurring in the sea state, the characteristic largest response is estimated. This approach is shown in Eq. (6.9). Here the zero-up-crossing period for the response process, T_{Xm02}, is simplified to $0.83T_p$ according to Eq. (3.5.5.4) in DNV-RP-C205 (2010).

$$1 - F_{X_G}(\tilde{x}_{400s}) = \frac{1}{n_{400s}} = \frac{1}{\frac{400s}{0.78 \times T_p}} \tag{6.9}$$

In the second approach, the extreme responses are obtained directly from the response series of the non-stationary simulations. This method involves performing repeated simulations of the complete deployment process and to study the extreme responses obtained from each response time series. The extreme response for the sea state is then determined from the average extreme, obtained from the 15 realisations of irregular waves.

In Sec. 6.2.2 the short-term extreme tension in the lift wire obtained from the two approaches are presented and compared.

6.2 Results and discussion

6.2.1 Effect of radiation damping

Figure 6.6 exemplifies the response spectral density obtained from the two approaches before the lift wire tension were modified to make the models behave more alike. This modification was justified on the basis of getting across the affect of including radiation damping, at a point where the initial conditions for the models differed due to non-consistent modelling of the installation system.

If various wave headings are to be considered, however, the eigenfrequencies of the remaining modes in Table 6.2 are not optimal. Since there exists a minor difference in the mean offsets of the monopile and the vessel under static conditions, the varying modelling of the gravity and the buoyancy should, for instance, be investigated to find the source of the difference.

The following results are obtained when the model with the modified lift wire stiffness is utilized. A significant reduction in the response spectral density is observed at the rotational resonance frequency in Figure 6.7 when the radiation damping of the XL monopile is included. This figure presents the response spectra for monopile surge and pitch obtained in irregular waves with H_s = 2 m and T_p = 5 s.

The large peak in the surge response spectra for low frequencies occur at the natural frequency of the pendulum motion and indicates that large responses occur when this motion is excited by incident waves. This response is critical for the installation op-

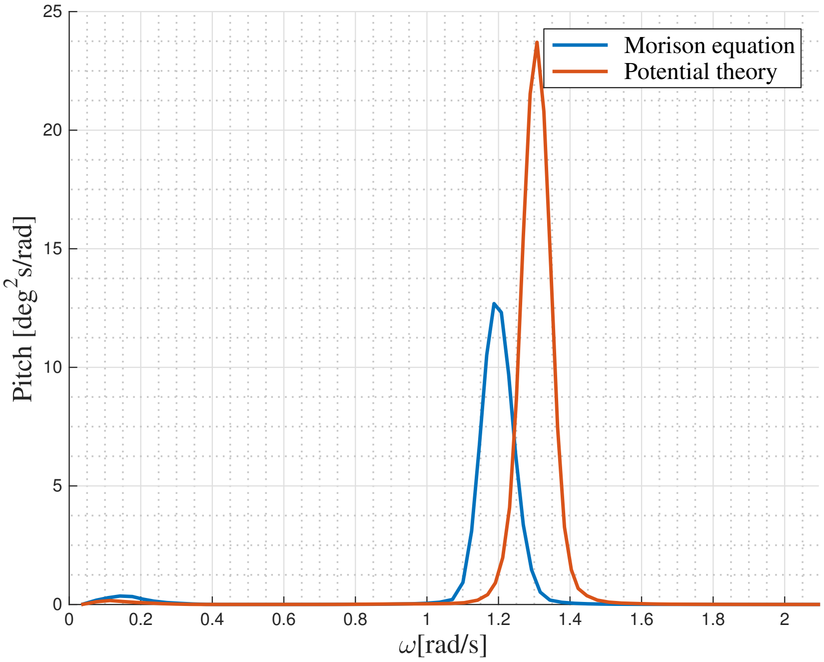

Figure 6.6: Response spectrum from steady-state simulations of time-invariant model and non-modified Morison model, at T$_p$ = 5 s, with monopile 20 m submerged.

eration and should be avoided. Since the natural frequency of the motion is low, most irregular sea states occurring do not have enough wave power close to this frequency to excite the motion. This response is also found in longer waves, as illustrated in Figure 6.8.

In the literature review of a similar case, it was found that spectra without this excited pendulum response can be obtained. This indicates that the modelling of the system in this thesis might benefit from some improvements and should be optimized further to achieve accurate estimates of the responses.

Due to the presumed error in the irregular analysis of the 20 m submerged monopile in long waves, discussed in Sec. 5.3.2. Figure 6.8 presents results obtained from steady-state analyses at 15 m draft. The same reduction in the response is also observed in this figure, at the rotational resonance frequency due to the radiation and diffraction of the monopile.

In this case, however, a second peak is also observed. This peak occur at the spectral peak period due to the monopile motion induced by the vessels increased response in the longer waves. At this peak, no reduction is observed. This is reasonable, due to the fact that this monopile motion is induced by the vessel response through the crane tip, which is not affected by the radiation damping.

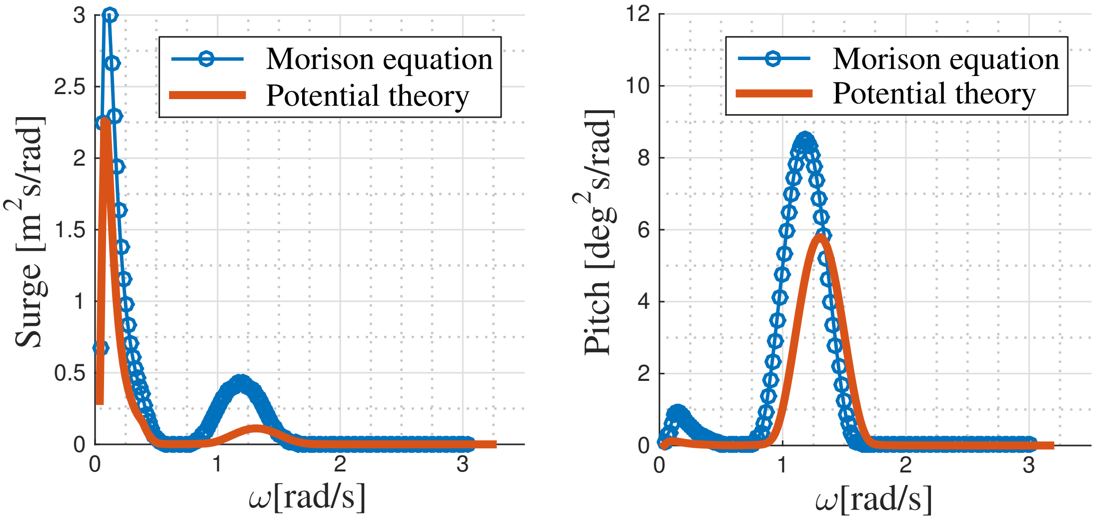

Figure 6.7: Response spectral density at H_s = 2 m, T_p = 5 and head sea.

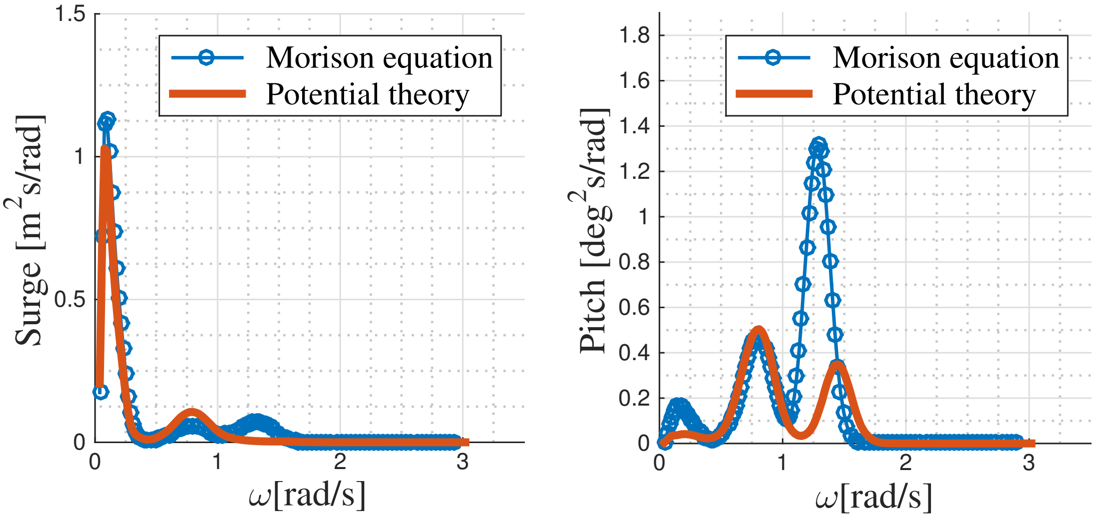

Figure 6.8: Response spectral density at H_s = 2 m, T_p = 8 s and head sea.

6.2.2 Comparison of responses from steady-state and non-stationary simulations

In Figure 6.9 the result of the fitting of the Rayleig distribution to the global maxima for each of the response series is presented. These distributions were utilized in the SIMO post processor to statistically determine the short-term extreme response. The average value from this analysis is compared to the average extreme lift wire tension, obtained from the non-stationary simulations in Table 6.6.

Based on Table 6.6 it is recommended to perform non-stationary simulations to obtain the extreme responses. These observations are supported bySandvik (2012), whom found that an unrealistic build-up of oscillations occur at the steady-state conditions,

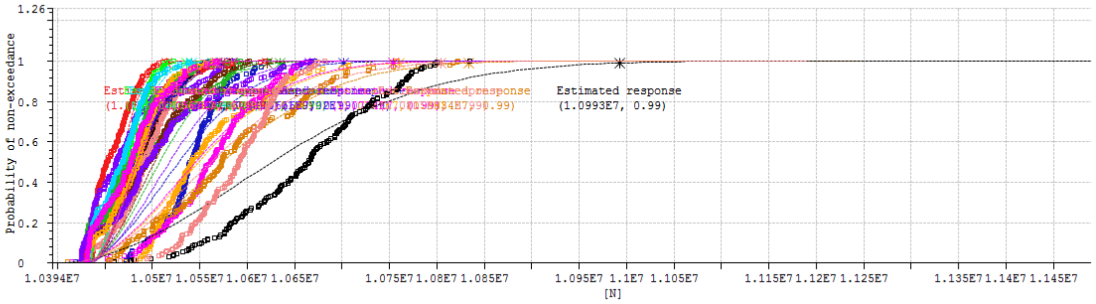

Figure 6.9: Rayleigh distribution fitted to the global maxima obtained from the stationary simulations at the most onerous position .

Table 6.6: Short-term extreme lift wire tension from steady-state and non-stationary analysis.

Steady-state wire tension [N]	Non-stationary wire tension [N]
1.06E+07	4.61E+06

which causes to high responses. The results obtained should, however, be further investigated to establish a well-founded basis for comparison.

Chapter 7

Conclusions and recommendations for further work

This thesis studied the responses in the coupled installation system for an XL monopile substructure. Dynamic analyses of the lowering phase of the installation operation were conducted to examine the difference between regular and irregular wave analysis, the effect of radiation damping from the monopile and the significance of performing complete non-stationary simulations of the lowering operation.

In this final chapter, the main conclusions of this thesis work and recommendations for further work are presented.

7.1 Conclusions

First, the numerical model of the coupled system composed of the XL monopile and the heavy lifting vessel were developed and time-variant hydrodynamic system properties were obtained from frequency-domain analyses in HydroD. Steady-state simulations were then performed to study the natural frequencies of the lifting system, before the difference between performing a regular and an irregular wave analysis was investigated.

Due to the fact that the system properties not are applicable directly in a non-stationary simulation where the monopile's position changes significantly, the simplification of conducting steady-state simulations was also utilized to study the affect of the radiation damping from the XL monopile. As an unrealistic build-up of oscillations have been found to be a weakness of this approach, the difference in the results obtained from a steady-state and a non-stationary simulation is also investigated by the use of a time-variant model based on strip theory.

The essential findings from this thesis work can be summarized as follows:

- **Eigenfrequencies strongly dependent on level of monopile submergence:** It is found that the eigenfrequencies of the rotational monopile motions are strongly depth-dependent. For a wave spectra with a T_p = 5 s, rotational resonance motions can thus be induced when the monopile is 20 m submerged, even though they are not induced at smaller drafts. It is also observed that the tension in the lift wire is governed by the rotational resonance motions of the monopile.

- **Regular wave analysis overestimates responses:** From the comparison of the results obtained from the regular- and irregular wave analysis it is found that the regular wave analysis predicts higher responses than the irregular analysis for every monopile draft, except for at resonance frequencies. Since time-domain analysis are expected to more accurately capture the nonlinear wave loads on the monopile and give larger responses than the ones predicted in the frequency-domain, it is concluded that the regular wave analysis overestimates the responses and that it is recommended to use an irregular wave analysis to predict the extreme responses in the installation system.

- **Radiation damping effect:** A significant reduction in the response spectral density is observed at the resonance rotational response of the monopile, when the potential damping is included in T_p = 5 s.

  In the response spectra for the monopile in irregular waves with T_p = 8 s two peaks are observed. The first peak is due to the motion induced by the vessel on the monopile through the crane, while the second is due to the resonance motion caused by the incident waves with a period close to the eigenperiod of the monopile. In this case, a drop in the response is observed for the resonance peak, but not for the spectral peak period peak. This is reasonable, since the radiation and diffraction of the monopile affects the wave induced motions of the pile, but do not affect the vessel response which causes the other motions. These findings indicate that the radiation damping affects the responses of the XL monopile, especially in short waves, and should be considered to obtain an accurate model.

- **Crucial to perform non-stationary simulations of the complete lowering process:** A significant difference is observed when the short-term extreme response in the lift wire, predicted from the stationary simulations, are compared to the average response obtained from the non-stationary simulations. This is due to the unrealistic build-up of oscillations that occur at steady-state conditions. It is therefore recommended to conduct several non-stationary simulations in time-domain at each sea state to estimate accurate responses.

7.2 Further work

The following list presents recommendations for how to further improve the accuracy of the numerical model of the lowering operation for installation of an XL monopile.

- **Include radiation damping in non-stationary analysis:** To assess the issue of the time-varying system properties, the approaches utilized in this thesis work were to either conduct steady-state simulations with the XL monopile in the most onerous position or to perform non-stationary simulations for a Morison model where the potential damping was excluded.

  Since the responses may be overestimated both by conducting steady-state simulations and by excluding the radiation damping of an XL monopile, the potential damping should have been included in the non-stationary analysis. To further improve the accuracy of the numerical model of the operation, a method proposed by Li et al. (2015) to compute the excitation forces from Morison's formula , account for the added mass- and quadratic drag coefficients using strip theory and include the potential damping through the retardation function could have been utilized.

- **Account for shielding effects:** In this study only undisturbed, head sea waves are considered for simplicity. To further improve the numerical model of the installation operation for the XL monopile, shielding effects should be considered. Li et al. (2014) found that the shielding effect, if the lowering operation is performed in the vicinity of a properly positioned HLV, are significant especially in short waves and should definitely be taken into account to obtain an optimal result.

- **Consider wave spreading:** To simplify this study, the waves were approximated as long-crested waves for all conditions. During real life operations, the vessel will be exposed to waves behaving more like short-crested waves. For certain wave headings, directional waves might affect the system RAOs greatly due to the spreading of the wave energy. To further improve this study, the waves should thus be modelled as short-crested waves. This also implies that different wave propagating directions should be considered, not only head sea.

- **Establish operational limits:** An important tool to utilize the weather window provided at the site in a best possible way, is to assess the operability at the relevant site based on the estimated system responses obtained from the numerical simulation. With regards to the number of lowering operations often required to install an offshore wind farm, it is crucial for the installation efficiency of the whole farm to increase the allowable sea state for each lifting operation.

  Future work should thus deal with the establishment of operational limits. To establish the limits, the tension in the lift wire should be considered to avoid wire breakage and snap loads. The translational and rotational motion of the monopile should also be studied, to ensure that the hydraulic cylinders in the gripper are preserved and that the inclination angle of the pile is acceptable prior to the driving operation, respectively.

- **Nonlinear loads:** The assumption that linear wave theory is applicable should be questioned, especially in severe conditions. According to the table showing the range of validy for the Airy theory in DNV-RP-C205 (2010), this assumption can not be completely justified for the sea states considered in this study. Further work should therefore include the nonlinear effect due to the instantaneous free surface and body position. This is supported by Li et al. (2015), whom found a significant increase in the resonse when nonlinear effects were accounted for and concluded that this effect are crucial.

- **Non-stationary simulations:** In further work, time-domain simulations of the complete deployment operations should be conducted as it was found that steady-state analyses overestimates the responses. Since only the lowering process is studied in this case, future work should include other severe operations like the hammering and upending operations to obtain a proper basis for establishing the allowable sea states.

Bibliography

4C Offshore Ltd (2016). Monopile support structure. Website: `http://www.4coffshore.com/windfarms/monopiles-support-structures-aid4.html`, accessed: 2016-08-01.

Anam, I., Roësset, J. M., et al. (2004). Slender-body approximations of hydrodynamic forces for spar platforms. *International Journal of Offshore and Polar Engineering*, 14(02).

Baar, J., Pijfers, J., van Santen, J., et al. (1992). Hydromechanically coupled motions of a crane vessel and a transport barge. In *Offshore Technology Conference*. Offshore Technology Conference.

Berg, T. E., Selvik, Ø., and Berge, B. O. (2015). *Defining operational criteria for offshore vessels*, pages 193–199. Taylor and Francis Group.

BVG Associates (2012). Offshore wind cost reduction pathways - technology work stream. Website: `http://www.thecrownestate.co.uk/media/5643/ei-bvg-owcrp-technology-workstream.pdf`, accessed: 2016-03-17.

BWEA (2004). Prospects for offshore wind energy. Website: `http://www.offshorewindenergy.org/reports/report_026.pdf`, accessed: 2016-03-17.

Clauss, G., Riekert, T., et al. (1990). Operational limitations of offshore crane vessels. In *Offshore Technology Conference*. Offshore Technology Conference.

Cozijn, J., van der Wal, R., Dunlop, C., et al. (2008). Model testing and complex numerical simulations for offshore installation. In *The Eighteenth International Offshore and Polar Engineering Conference*. International Society of Offshore and Polar Engineers.

Det Norske Veritas (2010a). Offshore standard dnv-os-e301 position mooring.

Det Norske Veritas (2010b). *SESAM User Manual Wadam - Wave Analysis by Diffraction and Morison Theory*, rev. 8 edition.

DNV-RP-C205 (2010). Dnv, dnv and loads, environmental. *Environmental conditions and environmental loads. Norway: Det Norske Veritas.*

EWEA (2015). The european offshore wind industry–key trends and statistics 2015. Website: `http://www.ewea.org/fileadmin/files/library/publications/statistics/EWEA-European-Offshore-Statistics-2015.pdf`, accessed: 2016-03-17.

Faltinsen, O. (1993). *Sea loads on ships and offshore structures*, volume 1. Cambridge university press.

Gao, Z., Luan, C., Moan, T., Skaare, B., Solberg, T., and Lygren, J. (2011). Comparative study of wind-and waveinduced dynamic responses of three floating wind turbines supported by spar, semi-submersible and tension-leg floaters. In *Proceedings of the 2011 International Conference on Offshore Wind Energy and Ocean Energy, October*.

Greco, M. (2012). Tmr 4215: sea loads lecture notes. *Trondheim, Norway: Dept. of Marine Technology, Norwegian University of Science and Technology*, pages 77–80.

Hasselmann, K., Barnett, T., Bouws, E., Carlson, H., Cartwright, D., Enke, K., Ewing, J., Gienapp, H., Hasselmann, D., Kruseman, P., et al. (1973). Measurements of wind-wave growth and swell decay during the joint north sea wave project (jonswap). Technical report, Deutches Hydrographisches Institut.

Haver, S. (2016). Stochastic description of ocean waves and response analysis and prediction of extremes. (Lecture Notes).

Herman, S. (2002). *Offshore wind farms: Analysis of transport and installation costs*. Energy Research Centre of the Netherlands.

IEA (2012). *Energy Technology Perspectives 2012: Pathways to a Clean Energy System*. OECD Publishing.

IEA (2013). Technology roadmap: Wind energy. Website: `http://www.iea.org/publications/freepublications/publication/Wind_2013_Roadmap.pdf`, accessed: 2016-03-17.

IHC (2016). Ihc iqip delivers new 1400t upending tool to seaway heavy lifting. Website: `https://www.royalihc.com/en/news/ihc-iqip-delivers-new-1400t-upending-tool-to-seaway-heavy-lifting`. assessed: 2016-08-01.

ISKES (2016). Offshore services gallery. Website: `http://iskestugs.nl/gallery`, assessed: 2016-06-31.

Jonkman, J. and Matha, D. (2011). Dynamics of offshore floating wind turbines—analysis of three concepts. *Wind Energy*, 14(4):557–569.

Kaiser, M. J. and Snyder, B. (2010). Offshore wind energy installation and decommissioning cost estimation in the us outer continental shelf. *Energy Research Group LLC, Louisiana*.

Karimirad, M. (2014). *Offshore Energy Structures For Wind Power, Wave Energy and Hybrid Marine Platforms*. Springer International Publishing.

Karimirad, M. and Moan, T. (2011). Extreme dynamic structural response analysis of catenary moored spar wind turbine in harsh environmental conditions. *Journal of offshore mechanics and Arctic engineering*, 133(4):041103.

K.E. Hansen A/S. Mono-pile upending trolley. Website: `http://www.knudehansen.com/references/offshore-offshore-wind-vessels/mono-pile-upending-trolley/`, accessed: 2016-08-01.

Kiełkiewicz, A., Marino, A., Vlachos, C., Maldonado, F. J. L., and Lessis, I. (2015). The practicality and challenges of using xl monopiles for offshore wind turbine substructures. Website: `http://www.esru.strath.ac.uk/EandE/Web_sites/14-15/XL_Monopiles/cost.html#introduction`, accessed: 2016-03-17.

Li, L. (2016). *Dynamic Analysis of the Installation of Monopiles for Offshore Wind Turbines*. PhD thesis, Norwegian University of Science and Technology.

Li, L., Acero, W. G., Gao, Z., and Moan, T. (2016a). Assessment of allowable sea states during installation of offshore wind turbine monopiles with shallow penetration in the seabed. *Journal of Offshore Mechanics and Arctic Engineering*, 138(4):041902.

Li, L., Gao, Z., and Moan, T. (2013). Numerical simulations for installation of offshore wind turbine monopiles using floating vessels. In *ASME 2013 32nd International Conference on Ocean, Offshore and Arctic Engineering*, pages V008T09A076–V008T09A076. American Society of Mechanical Engineers.

Li, L., Gao, Z., and Moan, T. (2015). Response analysis of a nonstationary lowering operation for an offshore wind turbine monopile substructure. *Journal of Offshore Mechanics and Arctic Engineering*, 137(5):051902.

Li, L., Gao, Z., Moan, T., et al. (2016b). Operability analysis of monopile lowering operation using different numerical approaches. *International Journal of Offshore and Polar Engineering*, 26(02):88–99.

Li, L., Gao, Z., Moan, T., and Ormberg, H. (2014). Analysis of lifting operation of a monopile for an offshore wind turbine considering vessel shielding effects. *Marine Structures*, 39:287–314.

MacCamy, R. and Fuchs, R. A. (1954). Wave forces on piles: a diffraction theory. Technical report, DTIC Document.

MARINTEK (2007). *SIMO User's Manual Version 3.6*. Trondheim, Norway.

MARINTEK (2009). *SIMO Theory Manual Version 3.6, rev:2*. Trondheim, Norway.

Matter, G. B., da Silva, R. R. M., and Tan, P.-L. (2005). Touchdown analysis of jack-up units for the definition of the installation and retrieval operational limits. In *ASME 2005 24th International Conference on Offshore Mechanics and Arctic Engineering*, pages 1115–1121. American Society of Mechanical Engineers.

Mavrakos, S. (1988). Hydrodynamic coefficients for a thick-walled bottomless cylindrical body floating in water of finite depth. *Ocean engineering*, 15(3):213–229.

MIT OCW (2005). Design principles for ocean vehicles (mit lecture). Website: `https://www.flickr.com/photos/mitopencourseware/4149929315`, accessed: 2016-06-06.

Moan, T. (2015). Recent development of analysis and design of offshore wind turbines for deep water. *Renewable Energies Offshore*, page 19.

Moné, C., Smith, A., Maples, B., and Hand, M. (2015). 2013 cost of wind energy.

Morison, J., Johnson, J., Schaaf, S., et al. (1950). The force exerted by surface waves on piles. *Journal of Petroleum Technology*, 2(05):149–154.

Mukerji, P. et al. (1988). Hydrodynamic responses of derrick vessels in waves during heavy lift operation. In *Offshore Technology Conference*. Offshore Technology Conference.

Muliawan, M. J., Karimirad, M., Moan, T., and Gao, Z. (2012). Stc (spar-torus combination): a combined spar-type floating wind turbine and large point absorber floating wave energy converter—promising and challenging. In *ASME 2012 31st International Conference on Ocean, Offshore and Arctic Engineering*, pages 667–676. American Society of Mechanical Engineers.

Myhr, A., Maus, K. J., Nygaard, T. A., et al. (2011). Experimental and computational comparisons of the oc3-hywind and tension-leg-buoy (tlb) floating wind turbine conceptual designs. In *The Twenty-first International Offshore and Polar Engineering Conference*. International Society of Offshore and Polar Engineers.

Newland, D. E. (2012). *An introduction to random vibrations, spectral & wavelet analysis*. Courier Corporation.

Nielsen, F. G. (2007). Lecture notes in marine operations. *Department of Marine Structures, Norwegian University of Science and Technology, Trondheim, Norway*.

OffshoreWind.biz (2011). The netherlands: Norwind installer and ulstein join forces on new offshore wind foundation installation vessel. Website: `http://www.offshorewind.biz/2011/11/28/`, assessed: 2016-08-01.

Park, K.-P., Cha, J.-H., and Lee, K.-Y. (2011). Dynamic factor analysis considering elastic boom effects in heavy lifting operations. *Ocean Engineering*, 38(10):1100–1113.

Perry, M., Sandvik, P., et al. (2005). Identification of hydrodynamic coefficients for foundation piles. In *The Fifteenth International Offshore and Polar Engineering Conference*. International Society of Offshore and Polar Engineers.

Pettersen, B. (2007). Marin teknikk 3: hydrodynamikk. *Dept. of Marin Techn. NTNU, Trondheim, Norway*.

Ringsberg, J. W., Daun, V., and Olsson, F. (2015). Analysis of impact loads on a self-elevating unit during jacking operation. In *ASME 2015 34th International Conference on Ocean, Offshore and Arctic Engineering*, pages V003T02A096–V003T02A096. American Society of Mechanical Engineers.

Sandvik, P. (2012). Estimation of extreme response from operations involving transients. In *2nd Marine Operations Specialty Symposium, Singapore, Aug*, pages 6–8.

Sarkar, A. and Gudmestad, O. T. (2011). Installation of monopiles for offshore wind turbines—by using end-caps and a subsea holding structure. In *ASME 2011 30th International Conference on Ocean, Offshore and Arctic Engineering*, pages 309–315. American Society of Mechanical Engineers.

Sarkar, A. and Gudmestad, O. T. (2013). Study on a new method for installing a monopile and a fully integrated offshore wind turbine structure. *Marine Structures*, 33:160–187.

Sarkar, A., Gudmestad, O. T., et al. (2012). Study on a new methodology proposed to install a monopile. In *The Twenty-second International Offshore and Polar Engineering Conference*. International Society of Offshore and Polar Engineers.

The Crown Estate (2012). Offshore wind cost reduction: Pathways study. *United Kingdom, May*.

Thomsen, K. (2014). *Offshore wind: a comprehensive guide to successful offshore wind farm installation*. Academic Press.

van den Boom, H., Dekker, J., Dallinga, R., et al. (1988). Computer analysis of heavy lift operations. In *Offshore Technology Conference*. Offshore Technology Conference.

Vattenfall Wind Power AB (2009). Vattenfall ab conceptual design study kriegers flak windforce 09. Website: `http://www.slideshare.net/ThomasStalin/conceptual-design-study-kriegers-flak-090618-redused`, accessed: 2016-08-01.

Vellekoop, A. (2015). Conceptual design of a time-efficient method for the installation of mono-piles exceeding crane capacity. Master's thesis, TU Delft, Delft University of Technology.

Wiser, R. . Z. Y. . M. H. . O. H. . D. I. e. . P. H. J. V. N. . M. O. . G. S. . A. Z. (2011). Wind energy. in ipcc special report on renewable energy sources and climate change mitigation [o. edenhofer et. al (eds)]. Report, Cambridge University Press, United Kingdom and New York.

Appendix A: Load-radius chart for main crane

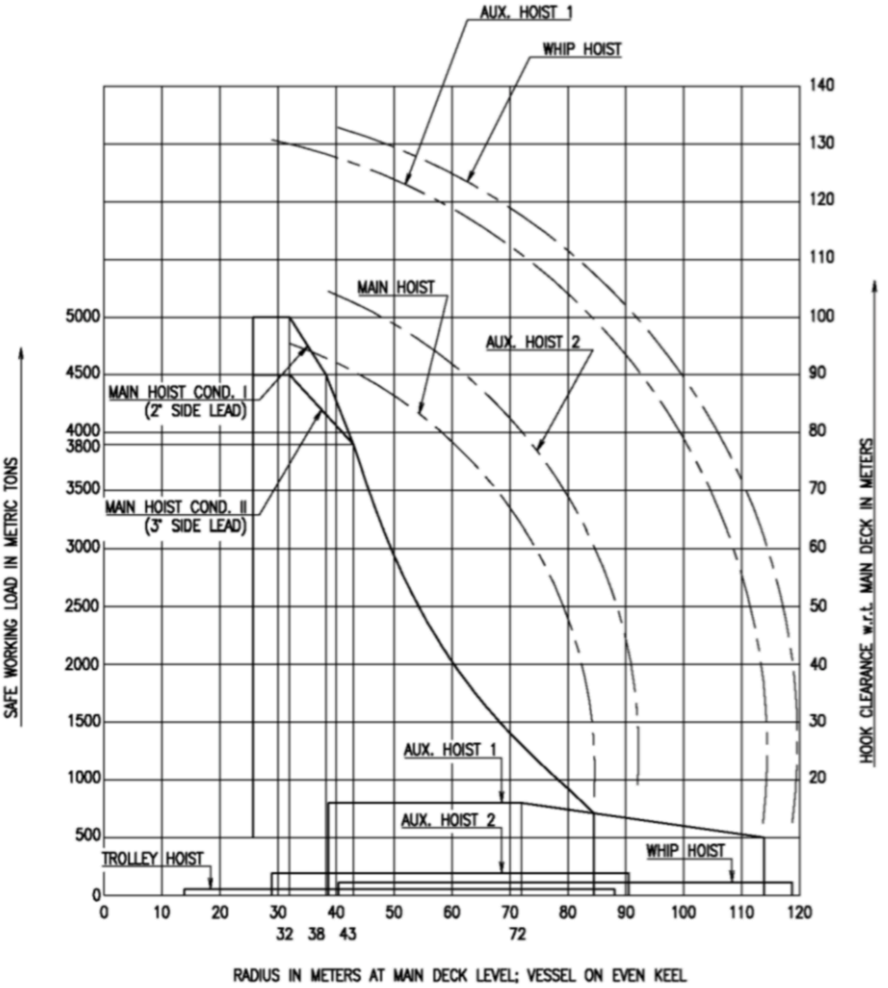

Appendix B: MATLAB - Response spectrum

This appendix contains the main script and the functions written in MATLAB by the author to generate a response spectrum from the RAOs obtained from the regular wave analysis in SIMO and a JONSWAP wave spectrum. The first code presented is the script with the main file, while the functions used in this script are given in the next sections.

```
% This script creates a response spectrum for various levels of monopile submergence
% from collected RAOs and a set of wave spectrums according to the expression:
% Sxx(w)=[RAO]^2xS(w). It also estimates the short-term extreme response
% ----------------------------------------------------------------------------------
% Functions:              Description
% ----------------------------------------------------------------------------------
% read                    Collects values for RAOs and frequencies in vectors
% JONSWAP                 Creates the wave spectrum, Sw, for the given Hs, Tp and freq
%                         vectors defined
% response_spectrum       Creates the response spectrum from the RAO and the wave
%                         spectrum
% spec_moments            Computes the spectral moments
% zero_cross_period       Finds the zero-up-crossing period
% extreme_resp            Estimate the short-term extreme responses and the
%                         STD
% ----------------------------------------------------------------------------------

[freq, d5_1, d10_1, d15_1, d20_1, d5_5, d10_5, d15_5, d20_5, d5_lift, d10_lift,
    d15_lift, d20_lift] = read();

Hs=[2]; %Vector containing the significant wave heights
Tp=[5,12]; %Vector containing the spectral peak periods

for j=1:length(Hs) %Loops through all Hs-values
    for k=1:length(Tp) %Loops through all Tp-values
        [Sw] = JONSWAP(Hs(j),Tp(k),freq); %Computes the wave spectrum
        [d5_resp_lift,d10_resp_lift,d15_resp_lift,d20_resp_lift]=resp_spectrum(Sw,
            freq, d5_1, d10_1, d15_1, d20_1, d5_5, d10_5, d15_5, d20_5, d5_lift,
            d10_lift, d15_lift, d20_lift); % Creates the response spectrum
    end %ends loop
end %end loop

[m0, m2] = spec_moments(freq,d5_resp_lift,d10_resp_lift,d15_resp_lift,d20_resp_lift);
     %takes in the parameters which are investigated

[Tz] = zero_cross_period(m0,m2);

[x_ext,STD] = extreme_resp(m0,Tz);
```

B.1 read.m

```
%%[freq,d5_1,d10_1,d15_1,d20_1,d5_5,d10_5,d15_5,d20_5,d5_lift,d10_lift,d15_lift,
    d20_lift] = read()
%
```

```
% This function reads from txt.-files with values, obtained in SIMO, for the RAOs
% and collects the values in vectors.
% ----------------------------------------------------------------------------------
% Parameters:  I/O     Description
% ----------------------------------------------------------------------------------
% freq             O      Vector containing wave frequencies
% d5_1           O      Vector with values for surge and 5 m MP submergence
% d10_1         O      Vector with values for surge and 10 m MP submergence
% d15_1         O      Vector with values for surge and 15 m MP submergence
% d20_1         O      Vector with values for surge and 20 m MP submergence
% d5_5           O      Vector with values for pitch and 5 m MP submergence
% d10_5         O      Vector with values for pitch and 10 m MP submergence
% d15_5         O      Vector with values for pitch and 15 m MP submergence
% d20_5         O      Vector with values for pitch and 20 m MP submergence
% d5_lift         O      Vector with values for lift and 5 m MP submergence
% d10_lift       O      Vector with values for lift and 10 m MP submergence
% d15_lift       O      Vector with values for lift and 15 m MP submergence
% d20_lift       O      Vector with values for lift and 20 m MP submergence
% ----------------------------------------------------------------------------------

function [freq,d5_1,d10_1,d15_1,d20_1,d5_5,d10_5,d15_5,d20_5,d5_lift,d10_lift,
    d15_lift,d20_lift] = read()

fid=fopen('mp_surge.txt'); %Open the txt.-file for surge
a=textscan(fid,'%f %f %f %f %f'); %Read all columns
fclose(fid);            %Close file
period=a{1};            %Save column 1 to vector period
freq=(2*pi)./period;    %Calc. frequency from period
d5_1=a{2};              %Save column 2 to vector d5_1
d10_1=a{3};             %Save column 3 to vector d10_1
d15_1=a{4};             %Save column 3 to vector d10_1
d20_1=a{5};             %Save column 5 to vector d20_1

fid=fopen('mp_pitch.txt'); %Open the txt.-file for pitch
a=textscan(fid,'%f %f %f %f %f'); %Read all columns
fclose(fid);    %Close file
d5_5=a{2};      %Save column 2 to vector d5_5
d10_5=a{3};     %Save column 3 to vector d10_5
d15_5=a{4};     %Save column 3 to vector d10_5
d20_5=a{5};     %Save column 5 to vector d20_5

fid=fopen('liftwire_mp_ZG.txt'); %Open the txt.-file for pitch
a=textscan(fid,'%f %f %f %f %f'); %Read all columns
fclose(fid);    %Close file
d5_lift=a{2};      %Save column 2 to vector d5_5
d10_lift=a{3};     %Save column 3 to vector d10_5
d15_lift=a{4};     %Save column 3 to vector d10_5
d20_lift=a{5};     %Save column 5 to vector d20_5
end %end function
```

B.2 JONSWAP.m

```
%% [Sw] = JONSWAP(Hs,Tp,w)
%
% This function computes the JONSWAP wave spectrum for a vector with wave
% frequencies and a given Hs and Tp value. The formula for the spectrum is taken
% from MARINTEK(2009).
% ----------------------------------------------------------------------------------
% Parameters:   I/O     Description
% ----------------------------------------------------------------------------------
% Hs             I      Significant wave height
% Tp             I      Spectral peak period
% w              I      Vector with wave frequencies
% ----------------------------------------------------------------------------------
```

```
function [Sw] = JONSWAP(Hs,Tp,w)

b=1.25; %Form parameter beta
y=3.3;  %Peakedness parameter gamma
a=5.061*(Hs^2/Tp^4)*(1-0.287*log(y)); %Spectral parameter alpha
s_a=0.07;       %Default value for spectral parameter sigma_a
s_b=0.09;       %Default value for spectral parameter sigma_a
wp=(2*pi)/Tp;   %Spectral peak frequency
g=9.81;         %Acceleration of gravity
Sw=zeros(1,length(w)); %Generates zero-vector for spectrum values

%% Loop to compute frequency dependent spectrum values
for i=1:length(w)
    if w(i)>wp %If/else statement to determine sigma parameter
        s=s_b;
    else
        s=s_a;
    end
    Sw(i)=((a*g^2)/(w(i)^5))*exp(-b*(wp/w(i))^4)*y^(exp(-((w(i)/wp-1)^2/(2*s^2))));
end

end %Ends function
```

B.3 response_spectrum.m

```
%% resp_spectrum(Sw,freq,RAO_d5_1, RAO_d10_1, RAO_d15_1, RAO_d20_1, RAO_d5_5,
    RAO_d10_5, RAO_d15_5, RAO_d20_5)
%
% This function computes the values for the response spectrum from eq.
% Sxx(w)=[RAO^]^2xS(w) and plots the response spectrum in surge and pitch.
% ----------------------------------------------------------------------------------
% Parameters:   I/O     Description
% ----------------------------------------------------------------------------------
% Sw             I      JONSWAP wave sepctrum
% freq           I      Vector containing all wave frequencies
% RAO_dj_k       I      Vector containing RAO values for MP submergence dj where
%                       j = 5,10,15,20 and DOF k where k = 1 and 5
% ----------------------------------------------------------------------------------

function resp_spectrum(Sw,freq,RAO_d5_1, RAO_d10_1, RAO_d15_1, RAO_d20_1, RAO_d5_5,
    RAO_d10_5, RAO_d15_5, RAO_d20_5)

%% Computes the [RAO]^2 values
d5_surge=RAO_d5_1.^2;
d10_surge=RAO_d10_1.^2;
d15_surge=RAO_d15_1.^2;
d20_surge=RAO_d20_1.^2;
d5_pitch=RAO_d5_5.^2;
d10_pitch=RAO_d10_5.^2;
d15_pitch=RAO_d15_5.^2;
d20_pitch=RAO_d20_5.^2;

%% Computes the values for the response spectrum, Sxx(w)
d5_resp_pitch=d5_pitch.*Sw';
d10_resp_pitch=d10_pitch.*Sw';
d15_resp_pitch=d15_pitch.*Sw';
d20_resp_pitch=d20_pitch.*Sw';
d5_resp_surge=d5_surge.*Sw';
d10_resp_surge=d10_surge.*Sw';
d15_resp_surge=d15_surge.*Sw';
d20_resp_surge=d20_surge.*Sw';

%% Plots a figure with 1 plot for surge and 1 plot for pitch
```

```
figure()
subplot(2,1,2)
hold on
p1=plot(freq,d5_resp_pitch,'-o',freq,d10_resp_pitch,'-o',freq,d15_resp_pitch,'-o',
    freq,d20_resp_pitch,'-o');
legend('\fontsize{14} \fontname{Times New Roman} 5 m','\fontsize{14} \fontname{Times
    New Roman} 10 m','\fontsize{14} \fontname{Times New Roman} 15 m','\fontsize{14} \
    fontname{Times New Roman} 20 m','location','northeast');
p1(1).LineWidth = 2;
p1(2).LineWidth = 2;
p1(3).LineWidth = 2;
p1(4).LineWidth = 2;
ylabel('Pitch [deg^2s/rad]','FontName','Times New Roman','FontSize',16);
xlabel('\omega [rad/s]','FontName','Times New Roman','FontSize',16);
grid on
grid minor
hold off

subplot(2,1,1)
hold on
p2=plot(freq, d5_resp_surge,'-o',freq,d10_resp_surge,'-o',freq,d15_resp_surge,'-o',
    freq,d20_resp_surge,'-o');
legend('\fontsize{14} \fontname{Times New Roman} 5 m','\fontsize{14} \fontname{Times
    New Roman} 10 m','\fontsize{14} \fontname{Times New Roman} 15 m','\fontsize{14} \
    fontname{Times New Roman} 20 m','location','northeast');
p2(1).LineWidth = 2;
p2(2).LineWidth = 2;
p2(3).LineWidth = 2;
p2(4).LineWidth = 2;
ylabel('Surge [m^2s/rad]','FontName','Times New Roman','FontSize',16);
xlabel('\omega [rad/s]','FontName','Times New Roman','FontSize',16);
grid on
grid minor
hold off

end %ends the function
```